European Heart Journal - Cardiovascular Imaging (2023) **24**, e119–e197
https://doi.org/10.1093/ehjci/jead090

EACVI DOCUMENT

Three-dimensional transoesophageal echocardiography: how to use and when to use—a clinical consensus statement from the European Association of Cardiovascular Imaging of the European Society of Cardiology

Francesco F. Faletra*, Eustachio Agricola , Frank A. Flachskampf, Rebecca Hahn, Mauro Pepi, Nina Ajmone Marsan, Nina Wunderlich, Leyla Elif Sade, Erwan Donal , Jose-Luis Zamorano, Bernard Cosyns, Mani Vannan, Thor Edvardsen , Alain Berrebi, Bogdan A. Popescu, Patrizio Lancellotti , and Roberto Lang

Reviewers: This document was reviewed by members of the 2020–2022 EACVI Scientific Documents Committee: Magnus Bäck, Philippe B. Bertrand, Marc Dweck, Niall Keenan, and Ivan Stankovic

Division of Cardiology, ISMETT: Istituto Mediterraneo per i Trapianti e Terapie ad Alta Specializzazione, Palermo, Lugano 6900, Switzerland

Received 7 April 2023; accepted 11 April 2023; online publish-ahead-of-print 1 June 2023

Three-dimensional transoesophageal echocardiography (3D TOE) has been rapidly developed in the last 15 years. Currently, 3D TOE is particularly useful as an additional imaging modality for the cardiac echocardiographers in the echo-lab, for cardiac interventionalists as a tool to guide complex catheter-based procedures cardiac, for surgeons to plan surgical strategies, and for cardiac anaesthesiologists and/or cardiologists, to assess intra-operative results. The authors of this document believe that acquiring 3D data set should become a 'standard part' of the TOE examination. This document provides (i) a basic understanding of the physic of 3D TOE technology which enables the echocardiographer to obtain new skills necessary to acquire, manipulate, and interpret 3D data sets, (ii) a description of valvular pathologies, and (iii) a description of non-valvular pathologies in which 3D TOE has shown to be a diagnostic tool particularly valuable. This document has a new format: instead of figures randomly positioned through the text, it has been organized in tables which include figures. We believe that this arrangement makes easier the lecture by clinical cardiologists and practising echocardiographers.

Keywords transoesophageal three-dimensional echocardiography • basic physical principle of 3D TOE • 3D TOE in valvular pathologies • 3D TOE in non-valvular pathologies

Introduction and scope

Two-dimensional multiplane transoesophageal echocardiography (2D TOE) is a well-established ultrasound technology which is extensively used in clinical practice, during percutaneous catheter-based procedures and in the operating room. Compared with transthoracic echocardiography (TTE), 2D TOE has the following advantages:

(a) Distortion of ultrasound beams crossing the thin muscular tissue and the squamous epithelium of the oesophageal wall is negligible.

---

* Corresponding author. E-mail: francesco.faletra@gmail.com

(b) The close proximity of the oesophagus to the posterior aspects of the heart allows the use of high-frequency transducers (5–7 MHz).

In other words, the better acoustic conditions and the high frequencies allow the acquisition of images with a higher spatial resolution than those provided by TTE.[1]

Limitations of TOE remain the discomfort of probe introduction in conscious patients, the limited transducer mobility, and the 'blind spot' of the ascending aorta (AO) and aortic arch due to interposition of the trachea and bronchi.

Nearly 15 years ago, advancements in computer and crystal technology resulted in a revolutionary transducer architecture, where a new generation of minute piezoelectric crystals was arranged in rows and columns. This innovative 'matrix' array transducer could acquire a pyramidal volumetric data set rather than a single cross-section displaying three-dimensional (3D) echocardiographic images in real time. In a few years, echocardiography, traditionally considered a 'tomographic' technique, entered into the three-dimensional realm.[2]

Not surprisingly, the inclusion of the 3D matrix array technology into 2D TOE probe has been particularly prolific and successful, creating 3D cardiac images with high-quality anatomical details. These characteristics have made three-dimensional transoesophageal echocardiography (3D TOE) an extraordinary diagnostic tool in clinical practice.[3–5]

Currently, 3D TOE is particularly useful as an additional imaging modality in the echo-lab,[6,7] for cardiac interventionalists as a tool to guide complex catheter-based procedures,[8] for cardiac surgeons to plan surgical strategies, and for cardiac anaesthesiologists and/or cardiologists, to assess intra-operative results.[9]

The authors of this clinical consensus document are well aware that 2D will continue to be the main modality of the TOE examination. However, at the same time, they do believe that acquiring 3D data set should become a 'standard part' of the TOE examination.

An effective use 3D TOE, requires (i) 'full understanding' of the technical principles of 3D acquisition and limitations and (ii) a 'systematic approach' to 3D image acquisition, analysis, and display of various cardiac structures.

This clinical consensus statement of the European Association of Cardiovascular Imaging (EACVI) of the European Society of Cardiology (ESC) aims to provide a practical methodologic approach on how to use and when to use 3D TOE in clinical practice. The present document is divided into the following two sections: section I offers a review of the basic physical principle of 3D TOE, imaging acquisition, imaging display, and limitations. Section II presents specific imaging protocol on 'when' and 'how' to use 3D TOE in different pathologies in which 3D TOE has shown to be a diagnostic imaging tool particularly valuable. The section II is divided into two parts: section II part 1 which describes the role of 3D TOE in valvular pathologies and section II part 2 which describes the role of 3D TOE in non-valvular pathologies.

Section I

Basic physical principles of 3D TOE

The fully sample matrix array transducer

Advances in computer technologies and miniaturization of electronic circuitries have made it possible to insert ~2500 new-generation piezoelectric crystals arranged in a matrix array assembly into the tip of normal-sized TOE probe. The technical term 'fully sampled' means that all acoustical elements can be simultaneously 'activated' for image acquisition.[10]

3D TOE transducers typically have ultrasound frequencies between 5 and 7 MHz and are capable of acquiring standard 2D images, including the rotation of 2D imaging planes across a 180° arc, pulsed, continuous, and colour Doppler capabilities. There is a much larger amount of data processing involved with a 3D data set compared with a 2D image (about 100 MB for an 'average' 3D loop at 30 volumes per second vs about 10 MB for a typical 2D loop at 52 frames per second). No clinically relevant problems with overheating or biological effects of sound energy have been reported with 3D TOE; however, long-time usage of active TOE probes with probe temperature >40°C should be avoided.

Table 1

Engineering achievements
New generation of piezoelectric crystals
Compared with traditional PZT/polymer composites, the new generation of piezoelectric crystals
• Have a more uniform atomic structure, exhibiting fewer impurities.
• Exhibit a larger band (i.e. when vibrating, they generate a wider spectrum of frequencies) which eventually results in increased ultrasound penetration and resolution.
• Convert electrical into mechanical energy (i.e. electro-mechanical coupling) with greater efficiency than the traditional PZT/polymer composites.
Matrix array transducer
• The matrix array transducer consists ~2500 crystals organized in 50 rows and 50 columns.
Miniaturization of electronic circuitries and active cooling
• Miniaturization has made it possible to accommodate in the tip of the transducer of the same size as a 2D TOE probe a huge number of electronic circuitries.
• Active cooling minimizes heat generation.
Beamforming circuitries
• These specific circuitries allow sending the data from the 2500 crystals into the typical 128 channels. Patches of 20–25 crystals converge their output in a single connecting wire (128 wires connect 2500 crystals to the main frame), thus minimizing the size of connecting cable.
Parallel beam forming
• Parallel beam forming allows to overcome the physical bottleneck of fixed ultrasound wave speed. The system transmits 1 wide beam and receives multiple narrow beams in parallel (up to 64 for 1 beam transmitted).
• The number of volumes/s is increased by a factor equal to the number of receiving beams.
• Excessive increase of the number of receiving beams leads to a deterioration of signal-to-noise ratio and to a decreased spatial resolution, since the peripheral beams become further away from the centre of the transmitted beam.
Real-time or live image
• 3D 'real-time' or 3D 'live image' means that the 3D image displays the movement at the same time in which the movement occurs. However, before reconstructing the 3D image, the scan lines generated by the matrix array transducer can be steered electronically in the lateral and elevational directions.
• The motion of TOE 3D image is displayed on the screen with a few millisecond delay. This delay is not perceived by the human eyes. In other words, the current technology is able to generate 3D images so rapidly that they are perceived as they occurred in real time.

Table 2

Terms
Temporal resolution (volume rate)
The term refers to the number of 3D volumetric data sets that can be displayed in 1 s. The volume rate is measured in Hz (i.e. 10 volumes/s = 10 Hz).
Spatial resolution (line density)
The spatial resolution depends on the number of scan lines (line density) and sector lines (sector density) within the pyramidal data set. The higher the line and sector density, the narrower the space between lines and sectors, and the better the spatial resolution.
Trade-off between spatial and temporal resolution and size of pyramidal data set
There is an inverse relation between the volume rate, volume size, and number of scan/sector density (which corresponds to spatial resolution). Any increase of one of them causes a decrease of the other two. The better the spatial resolution, the lower the temporal resolution, and vice versa. The bigger the size of the pyramidal data set, the lower the temporal resolution, and vice versa. Some platforms allow modification of volume rates by changing the line/sector density.
Anisotropy of the 3D voxel
The 3D TOE voxel is 'anisotropic' (see image). This term means that the 3D image has a different spatial resolution in each dimension. The axial resolution is ∼1 mm (Line A), the lateral or azimuthal (*x*-axis) resolution is ∼ 2 mm (Line B), and the elevational resolution (*z*-axis) is ∼ 3 mm (Line C). Because of this anisotropy, the quality of a 3D TOE image obtained by the same 3D data set may deteriorate if the 3D image is rotated in space. For example, whenever the ultrasound beam cannot be aligned perpendicularly to the structure of interest, the corresponding 3D image is reconstructed predominantly based on lateral or elevational resolution which are inferior to the axial resolution. Awareness of the 3D voxel anisotropy may help in choosing the best image orientation for any specific structure. 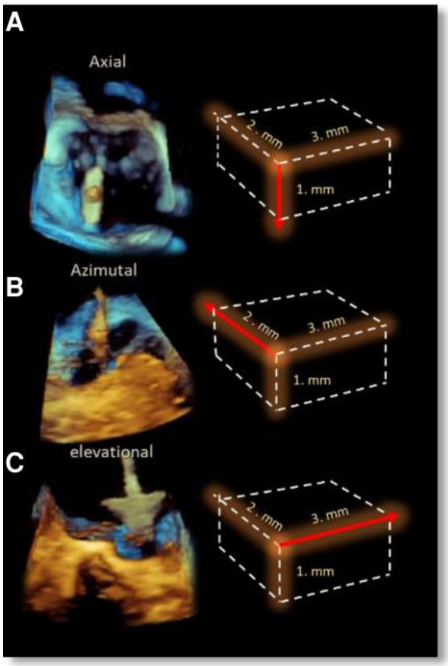

Table 1 summarizes the engineering achievements of 3D TOE images. *Table 2* summarizes the most common terms utilized in this clinical consensus document and their meaning.

Key points

The matrix array transducer (∼2500 crystals organized in 50 rows and 50 columns) allows obtaining 3D volumetric data set virtually in 'real time'.

Trade-off between spatial and temporal resolution and size of pyramidal data set should be taken into account for obtaining diagnostic 3D images with the best spatial and temporal resolution.

3D images should be reconstructed and displayed prevalently based on axial orientation.

Acquisition modalities

As general rule, before 3D acquisition, the 2D TOE image must be optimized: poor 2D TOE results in even poorer 3D TOE.

There are several modalities for acquiring a 3D data set:

(i) Simultaneous 2D multiplane (also known as biplane or triplane) imaging
(ii) Real-time 3D (also known as narrow/live 3D, single-beat)
(iii) Zoom modality single-beat and multi-beat
(iv) Multiple-beat ECG-gated acquisitions
(v) 3D TOE colour Doppler

Table 3 shows a brief description and 3D TOE examples of acquisition modalities.

Table 3

Acquisition modality	Image description	Image
Simultaneous 2D multiplane imaging Although this modality does not generate 3D images, it is one of the most commonly used image acquisitions. Two simultaneous cross-section views of the same heart beat can be shown by activating two lines of the matrix transducer. Using the primary 2D image as a reference plane, a moveable linear indicator (tilt plane) defines the location of the secondary plane. By default, orientation of the two cross-sectional planes is orthogonal (90°) to each other. The rotation angle of the second image is modifiable by the echocardiographer, and the location of the secondary plane can be anywhere along the sector of the primary image. Doppler colour flow can be superimposed.	**Image A** The image shows a typical biplane image. The tilting plane is oriented on the base of the AML. The secondary plane shows the perpendicular section (90°) corresponding to the tilting plane. **Image B** The image shows the tilting plane crossing the aortic leaflets in systole. The secondary plane shows the aortic leaflets in cross-section. **Image C** The image shows a biplane image of a regurgitant jet due to aortic leaflet perforation. The secondary plane shows the vena contracta (VC) (red arrow).	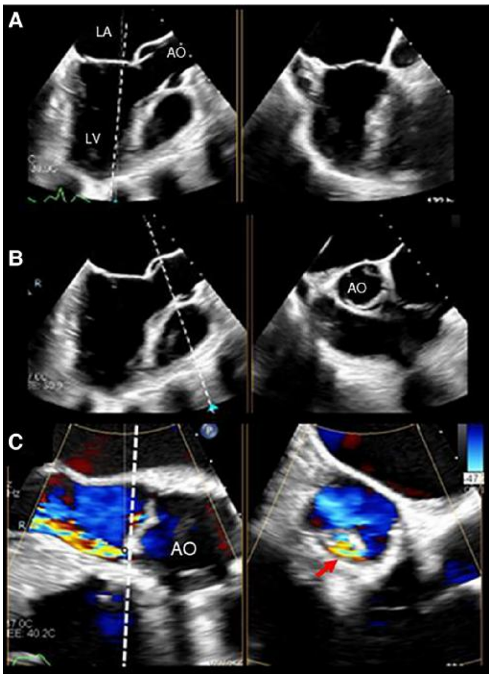
Real-time single beat modality A dedicated button shifts the initial 2D TOE into a 3D TOE image. TOE volume data acquisition typically appears as a solid narrow angle pyramidal data set (usually 30°×60°). Independent adjustments of the azimuthal and elevational planes (up to 90°×90°) can increase the size of the pyramidal data set. Being devoid of stitching artefacts, this modality is often used during percutaneous procedures.	**Image A** The image shows a pyramidal data set enlarged in the lateral/azimuthal plane (curved arrows) **Image B** The image shows the same pyramidal data set enlarged in the elevational plane (curved arrows). There is a progressive decrease in temporal resolution as the 3D pyramidal data set gets larger.	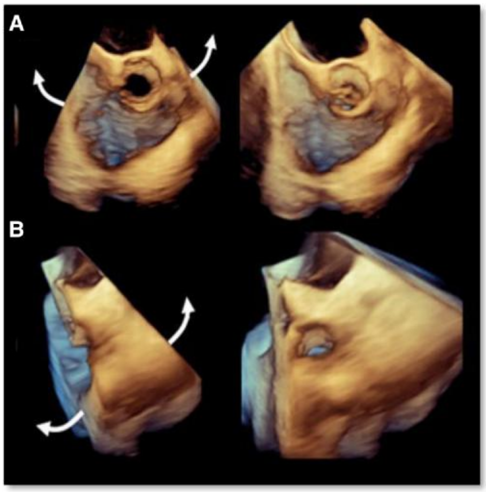
Real-time single-beat 'zoom modality' This modality displays a truncated and magnified pyramidal data set of the region of interest (ROI). Once activated, a 2D preview image shows the original view (reference plane) and its orthogonal plane. Two trapezoid-shaped boxes serve to define the position and the size of the ROI. This modality does not suffer from stitching artefacts.	**Image A** 2D TOE preview image. The truncated pyramid delineates the ROI which includes the MV; LV, left ventricle. **Image B** The image shows the resultant 3D TOE image obtained from image A shown in surgical view and displayed in photorealistic volume rendering; MV, mitral valve. **Image C** The truncated pyramid defines the ROI which includes the LAA.	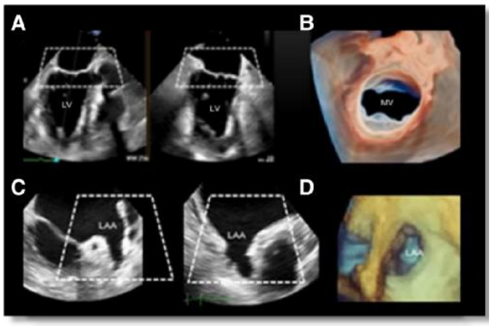

Continued

Table 3 Continued

Acquisition modality	Image description	Image
	Image D The image shows the resultant 3D TOE image obtained from image C. The LAA is shown from above and displayed in classic volume rendering with the LAA orifice seen in 'en face'.	
ECG-gated multi-beat acquisition modality This image acquisition is constructed by merging up to six narrow sectors (or sub-volumes). The correct acquisition requires regular heart rhythm and breath holding. The volume rate and line density are those of a single sector. Therefore, the final image has the same high spatial and temporal resolution of their sub-volume. However, since the entire final image is unavailable until the last sector is acquired, this modality is not 'real time'. Moreover, this acquisition modality suffers of stitching artefacts due to incorrect juxtaposition at the interface between two adjacent sectors.	**Image A** The image shows six sectors forming a composite image of the MV. The spatial and temporal resolutions are excellent. In this example, the temporal resolution is 56 volume/s. **Image B** The image shows two examples of stitching artefacts which occur in case of irregular rhythm (arrows).	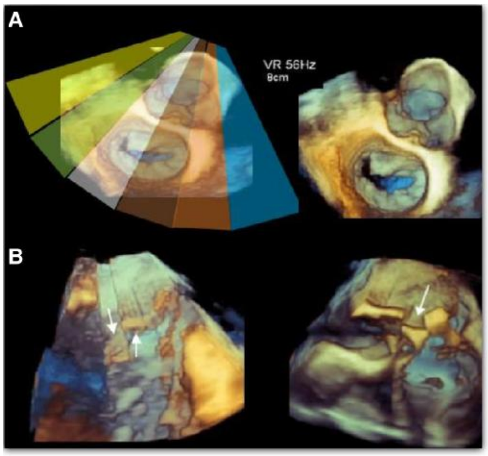
ECG-gated multi-beat 3D TOE acquisition in zoom modality This combined modality allows obtaining 3D images with the highest temporal rate (> 100 volume/s) and the optimal spatial resolution.	**Images A and B** Multi-beat zoom acquisition of two MVs. The volume rate is 82 and 101 in images A and B, respectively.	
3D colour Doppler multi-beat and single-beat acquisition Colour Doppler can be used either with a single-beat or in ECG-gated multi-beat acquisitions. The addition of colour Doppler reduces the frame rate of both modalities.	**Image A** The image shows one example of a multi-beat acquisition. The volume rate is 26 Hz. **Image B** The image shows an example of a single-beat acquisition. The volume rate is significantly decreased (18 Hz).	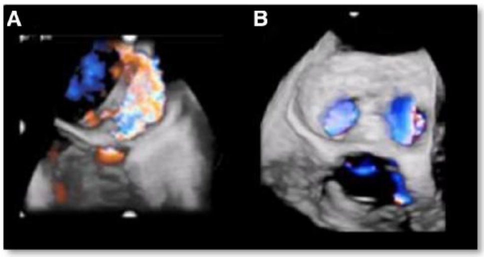

Key points

Simultaneous 2D multiplane imaging is one of the most commonly used image acquisitions, allowing obtaining two simultaneous cross-section views of the same heartbeat.

For acquiring images of the valves, the best acquisition modality is the multi-beat ECG-gated acquisition which allows the highest temporal and spatial resolution. However, this acquisition modality is not in ‘real time’ and suffers of stitching artefacts.

Zoom modality single-beat is the preferred imaging modality in patients with irregular rhythm and for guiding transcatheter procedures.

The addition of colour Doppler reduces the frame rate.

Image optimization (compression, smoothing, gain, and cropping)

Current guideline recommendations on how to set compression, smoothing, and gain for optimization of 3D images are scarce. ‘Low compression’ produces a high-contrast image which better shows fine details. ‘Smoothing’ makes a rough surface more uniform. The ‘gain’ amplifies returning echoes before being displayed. Too high gain setting produces marked static noises that resemble dense spontaneous echo contrast. Too low a gain setting creates dropout artefacts in the tissues. An optimal gain setting likely depends on depth, size, thickness, location, and orientation of the structure of interest with respect to the ultrasound beam direction. A certain level of gain setting may be optimal for a given structure, but too high or too low for an adjacent structure in the same image. As a general rule, the optimal gain

Table 4

Type of cropping	Image
Fix tomographic cropping planes The fix tomographic cropping planes allow cropping of the pyramidal data set in the three directions of the space (X, Z, and Y). **Image A** shows a volumetric data set in which there barely are recognizable structures. By advancing the cropping plane in the Z or elevational direction (arrows), the right atrium (RA) and coronary sinus (CS) are seen (Image B). **Images C and D** show the cropping plane advancing in the Y or axial direction and in the X or azimuthal direction, respectively.	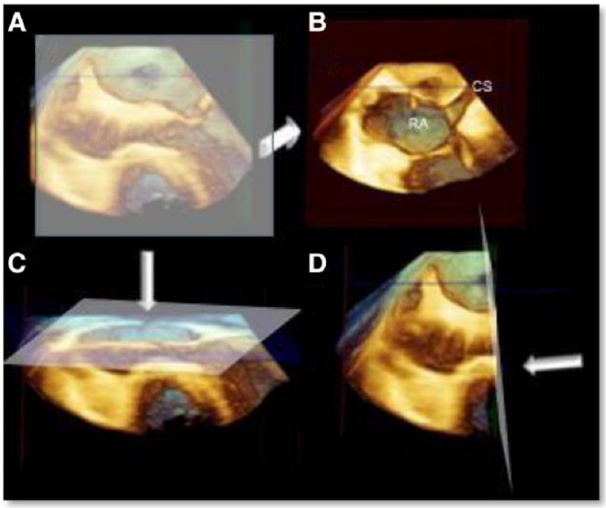
Images A–D show a ‘free cropping plane’. The pyramidal data set can be cropped in any arbitrary direction by a freely adjustable cropping plane. Figure B shows a ‘face crop’ in the direction of the observer.	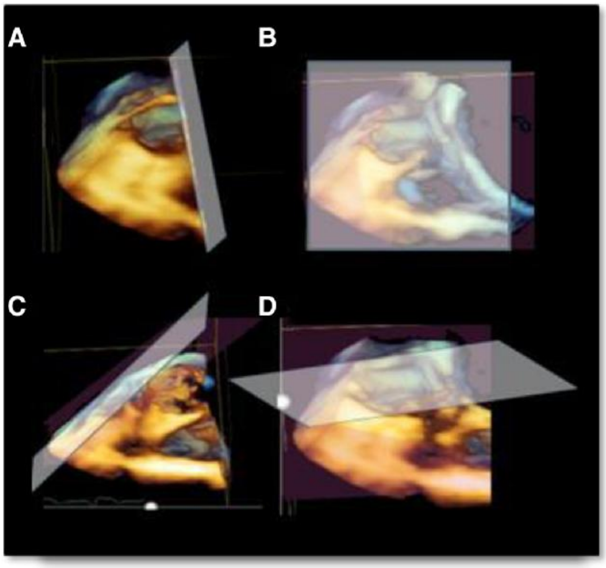

Continued

Table 4 Continued

Type of cropping	Image
Focused cropping **Image A** shows as 2D cross-sectional images are used as a guide, to visualize the structure of interest within the volumetric data set.	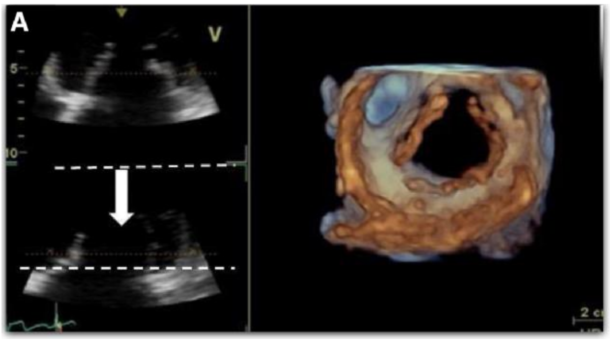

should be set in such a way as to eliminate the static noises while preserving anatomic structures.

The concept of 'cropping' is of critical importance to 3D echocardiography. This tool allows removing redundant tissues to expose the structure of interest. Different vendors offer several methods to achieve adequate tissue cropping (Crop Adjust Box, Crop Adjust Plane, Crop Tool, Box Edit, Clip Crop, etc.). Essentially, there are three main modalities: (i) fix tomographic cropping planes along the *X-Y-Z* directions; (ii) free cropping plane along any direction, and (iii) focused cropping using 2D cross-sectional images as a guide. Some platforms provide an 'automatic' display of the structure within the 3D data set without the need for manual cropping.

Table 4 shows the three main types of tissue cropping and the corresponding 3D TOE images.

Image display

Regardless of the acquisition modality, a key challenge is how to display 3D structures on a 2D screen/user interface. This is done by computer-generated texturing and shadowing to create the perception of a 3D solid which can be rotated and tilted in any direction. Of note, any individual tomographic 2D slice can be extracted from an acquired 3D data set.

Key 3D image displays include:

(i) Volume rendering
(ii) Surface rendering
(iii) Photorealistic vision
(iv) Glass (transparency)
(v) Multiplanar reconstruction
(vi) 2D tomographic slices

Table 5 shows the different modalities of image displays.

Table 5

Modality of image display	Description	Image
Volume rendering modality This modality uses various shades of blue/bronze combination to improve the perception of the third dimension (depth). In general, the system uses lighter shades (i.e. yellow–bronze) for structures that are closer to the observer and darker shades (i.e. brown/blue) for deeper structures.	**Image A** 3D TOE images in volume rendering modality showing the AO, LAA, the left upper pulmonary vein (LUPV), and the MV. The blue/bronze colour shades improve the perception of depth. **Image B** 3D TOE images in volume rendering modality showing the AO and the right ventricular outflow tract (RVOT).	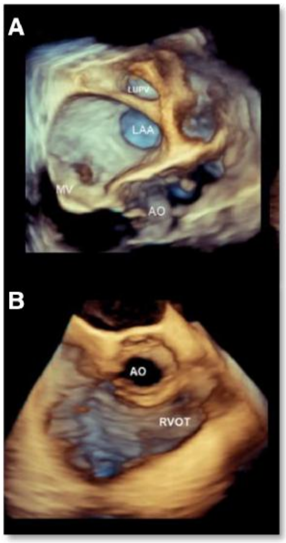
Surface rendering modality This modality depicts the surfaces of structures which have been identified by manual or (semi)automated border tracing. These automated algorithms utilize pattern recognition and other forms of artificial intelligence to identify fiducial anatomic landmarks. This modelling approach is currently extremely useful for measuring several parameters (diameters and areas and volumes) of different cardiac structures.	**Image A** The image shows the surface rendering of a MV obtained by different vendors. The image shows the surface rendering image which can be shown alone or inserted onto a 3D solid pyramidal data set. Several measurements can be done. **Image B** The image shows the surface rendering of the RV, LV, and LA.	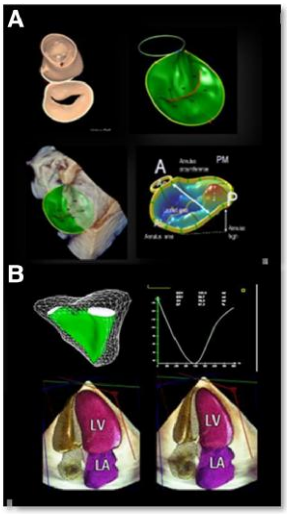
Photorealistic vision (true-view) This tool uses a freely movable virtual source of light, to enhance shadowing (and therefore the perception of depth). Positioned beyond the image, the light source generates an effect of transillumination enhancing delineation of orifices, borders, and cavities.[11]	**Image A** The image shows the orifice of the LAA illuminated by four different positions of the virtual source of the light (yellow arrows), creating different effects in the shadowing. **Image B** The effect of transillumination delineates orifices and border. Moreover, thick tissue, such as rough zone (RZ) compared with clear zone (CZ) and calcium (CA), is seen as dark regions since the light does not cross through.	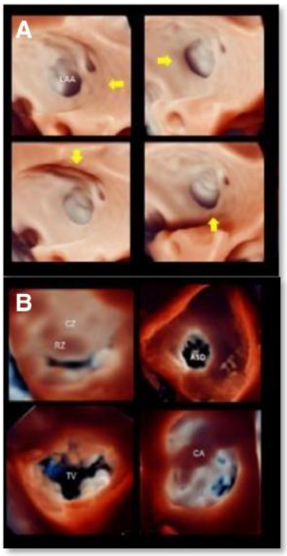

Continued

Table 5 **Continued**

Modality of image display	Description	Image
Glass (transparency) This tool allows the operator to adjust the degree of transparency of both cardiac and extra-cardiac structures.[12]	**Image A** shows MV scallops (P1, P2, and P3), post-clipping MV, mitral stenosis (MS), and flail of central scallop of PML (P2), respectively. In some circumstances, transparency improves the perception of three-dimensionality. C = clip.	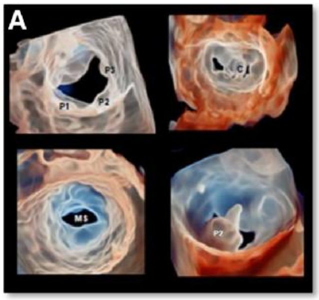
Multiplanar reconstruction This modality allows live rotation of perpendicular planes on either 2D or 3D image to display any desired 2D imaging plane. Real-time measurements can then be performed on selected 2D imaging planes, thus avoiding inaccuracies of direct measurements on 3D displays, due to parallax*. *'Parallax is the effect whereby the position or direction of an object appears to differ when viewed from different positions and it is a phenomenon specific to 3D rendered images.'	**Image A** shows how to measure the size of LAA. A three-step approach is advised. 'Step one': two orthogonal 2D planes are oriented perpendicular to the structure to be measured. 'Step two': The third orthogonal 2D plane is positioned at the level of the structure to be measured. 'Step three': The structure in the third 2D plane is measured.	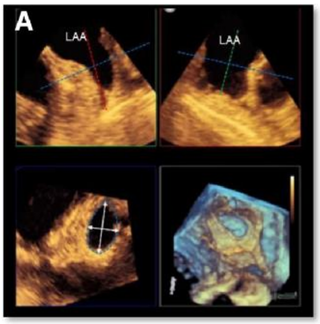
2D tomographic slices This tool shows multiple parallel cross-sections extracted automatically from a single pyramidal data set. This tool is particularly useful for wall motion analysis at different levels.	**Image A** shows 2D TOE tomographic slices focused on the LV.	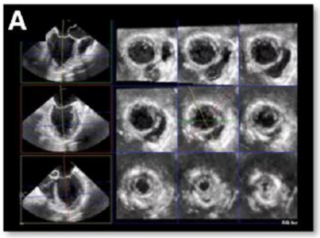

Key points

'Volume rendering modality' uses various shades of blue/bronze combination to improve the perception of the third dimension. It is the most used modality.

'Surface rendering modality' depicts the surfaces of structures identified by manual or (semi)automated border tracing. This modelling approach is useful for quantitative assessment.

'Photorealistic vision (true-view)' uses a freely movable virtual source of light, to enhance shadowing (and therefore the perception of depth), and, located beyond the structures, generates an effect of transillumination which may enhance delineation of orifices and borders.

'Transparency (glass)' allows the operator to adjust the degree of transparency of both cardiac and extra-cardiac structures.

'Multiplanar reconstruction' uses 2D images derived by 3D data set, allowing displaying any desired 2D imaging plane.

'2D tomographic slices' show multiple parallel cross-sections extracted automatically from a single pyramidal data set.

3D TOE pitfalls

3D TOE is subject to the same ultrasound artefacts as 2D TOE but also some that are unique to this imaging modality. A comprehensive description of 3D artefacts has been published elsewhere.[13] Herein, we describe the most common pitfalls that occur in 3D TOE 'but not' in 2D TOE. These pitfalls are due to inability of 3D TOE to define whether a given mass has a 'soft' or hyperechogenic (very bright) texture. 3D TOE uses different shades of blue/bronze or different positions of the virtual source of light for improving the perception of depth rather than for texturing (soft or hyperechogenic) a given mass. Thus, endocarditis, vegetations, thrombi, and calcifications show the same blue/bronze shade of colour of those surrounding structures which lie at the same depth (see *Table 6*).

Table 6

Pathology	Image
Vegetations **Image A** 2D TOE showing a bacterial vegetation (red circle). The texture of the vegetation is 'soft' and clearly distinguishable from surrounding structures. **Image B** 3D TOE showing the same case with volume rendering modality. The texture of vegetation (red circle) is similar to the surrounding tissues.	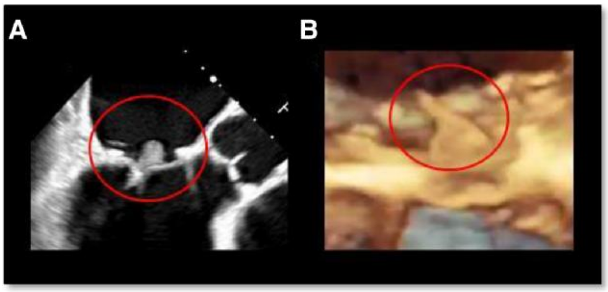
Calcifications **Image A** 2D TOE image showing an extensive calcification of the MA (red circle). Calcifications appear hyperechogenic. **Images B** 3D TOE image of the same case. Calcifications have the same texture of adjacent structures.	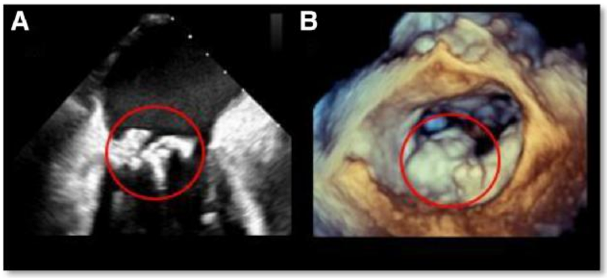
Thrombi **Image A** 2D TOE image showing a thrombus (asterisk) positioned deep in the LAA. The thrombus has a 'softer' texture than surrounding tissues. **Image B** 3D TOE image of the same case. The thrombus (asterisk) has almost the same texture of surrounding tissues. LAA, left atrial appendage.	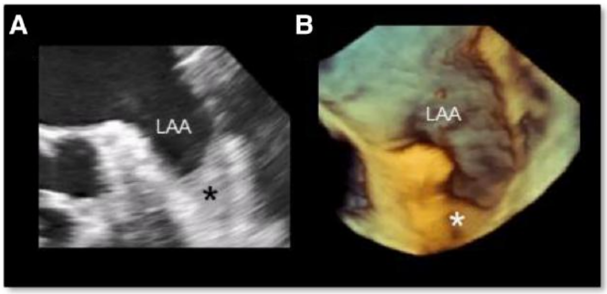

Key points

3D TOE uses different shades of blue/bronze for improving the perception of depth rather than for texturing (soft or hyperechogenic) of cardiac structures and masses.

Thus, endocarditis, vegetations, thrombi, and calcifications show the same blue/bronze shade of colour of those surrounding structures which lie at the same depth.

Section II part 1

Mitral valve

Introduction

There are multiple circumstances that make 3D TOE the 'ideal' technique for mitral valve (MV) imaging. First, the nearly perpendicular angle of incidence between the pyramidal beam and mitral leaflets. Hence, the 3D image of the valve is reconstructed mostly using axial resolution with the highest spatial resolution (see section of physics).

Secondly, the short distance between the valve and the TOE transducer coupled with the absence of ribs and lungs. Both circumstances allow the use of high-frequency transducers without artefacts and 3D image distortion.

Thirdly, the ability of 3D TOE volumetric data set to be rotated in any direction depicting the valve from a countless number of perspectives, the most popular being the view from overhead (the so-called surgical view with the AO is on top of the image at 12 o' clock).

A correct interpretation of the wide spectrum of MV diseases requires the knowledge of the 3D TOE features of normal MV anatomy.

Normal MV anatomy

The main components of the MV apparatus are the mitral annulus (MA), the anterior (AML) and posterior (PML) mitral leaflets, the chordae tendineae, and the papillary muscles (PMs). These components work together with a delicate balance of spatial and temporal coordination, preventing systolic leakage and allowing an unrestricted diastolic inflow.

3D TOE offers impressive, high-quality images of the normal MV anatomy.

Table 7 shows examples of the normal 3D TOE aspects of normal MV anatomy.

Table 7

MV anatomy	Image description	Image
MA[14] The MA can be divided into an anterior and a posterior segment. **The** '**posterior segment**' has a 'C shape', extending posteriorly from the left to the right trigone, and can be described as a convergence of atrial and ventricular walls, external adipose tissue, and the hinge line of the PML. These components are glued together by a discontinuous string of fibrous tissue. **The** '**anterior annulus**' is simply the hinge line of the AML, which is in continuity with the atrial wall on its atrial aspect and with the mitral aortic curtain on its ventricular aspect. The MA has a saddle-shaped configuration. During systole, the MA contracts, moves towards the apex, and increases its saddle shape.	**Image A** 3D TOE image of MV (surgical view) in diastole. The white dotted line denotes the posterior annulus. **Image B** Same valve in systole. The red dotted line denotes the posterior annulus. The white and red dotted lines show the sphincter-like contraction of the posterior MA from diastole to systole. **Image C** The red line depicts the hinge line of the anterior MA, in continuity with the atrial wall. **Image D** The AML seen from a ventricular perspective. The dotted line depicts the hinge line of the AML. The image also shows the mitral–aortic curtain 'en face' view (yellow area).	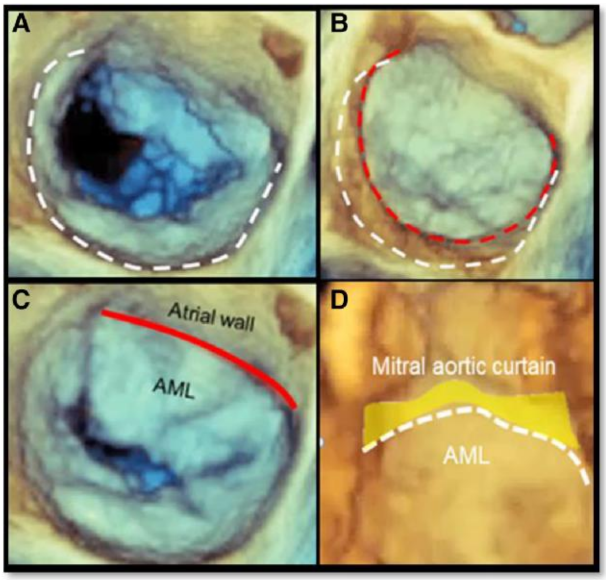
Mitral leaflets[15] Two main commissures separate the MV in two leaflets. The AML is a single veil, and the PML is divided by indentations into three (or more) sub-segments called scallops and labelled P1, P2, and P3. Though devoid of indentations, the corresponding areas of the AML are named A1, A2, and A3. The ventricular surface of both leaflets presents two distinct zones: the rough and the clear zone. The rough zone covers the distal surface of both leaflets and receives the insertions of chordae tendineae assuming a corrugated surface. The clear zone covers the remaining ventricular surface and has a smooth surface. Interestingly, from an atrial aspect, the rough zone corresponds to the coaptation area.	**Image A** 3D TOE surgical view. The image shows the AML and the PML divided by two indentations (arrows) into three scallops. **Image B** The image shows that the AML is a single veil (though divided into three segments), while the PML has three scallops (P1, P2, and P3). The arrows mark the indentations. **Image C** 3D TOE in cross-section (oblique view) showing the rough and clear zones. **Image D** 3D TOE photorealistic vision from the ventricular perspective. The source of light is positioned beyond the valve creating an effect of 'transillumination'. The rough zone (being thicker than the clear zone) appears darker.	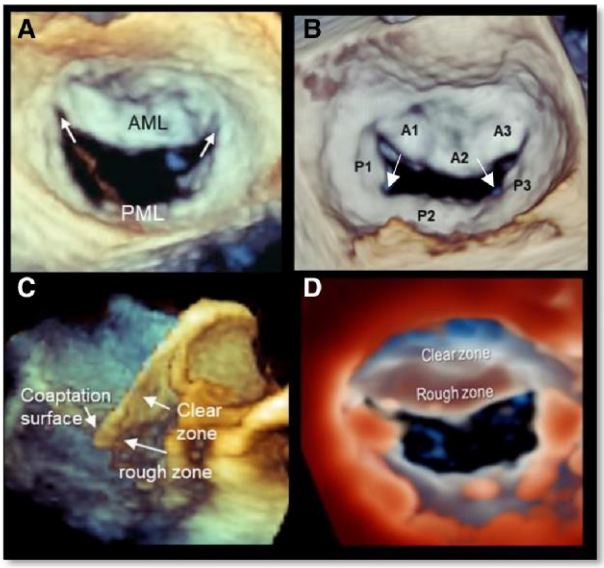

Continued

Table 7 Continued

MV anatomy	Image description	Image
Chordae tendineae and PMs[16,17]		
Anatomists describe three types of chordae: primary (or marginal), secondary (or strut), and tertiary. **The** ‘**primary chordae**’ are inserted on the free margins of the leaflets and prevent leaflet prolapse; **the** ‘**secondary chordae**’ are inserted laterally and medially on the border between the rough and clear zones. These chordae (often present only on the AML) are thicker and more resistant than the marginal chordae because they are stretched either in diastole or systole. The assembly leaflet–strut chordae–PMs appear to preserve the LV geometry and function. **The** ‘**tertiary chordae**’ extend from the ventricular wall on the base of PML, likely preventing leaflet prolapse. Contrary to conventional belief, ‘PM**s**’ do not arise as a single pillar from a compact myocardium, but rather from a network of trabeculations. with several branches.	Because of insufficient spatial resolution, usually, 3D TOE cannot distinguish between different types of chordae or visualize the spaces between PMs. For this purpose, 2D TOE (or 2D TOE image derived by the 3D data set) is the most valuable echocardiographic technique especially when acquired in the trans-gastric views. **Images A and B** The images show the different types of chordae tendineae SC = strut chordae; MC = marginal chordae; TC = tertiary chordae. **Images C and D** show that PMs do not arise as a single pillar but rather with several branches.	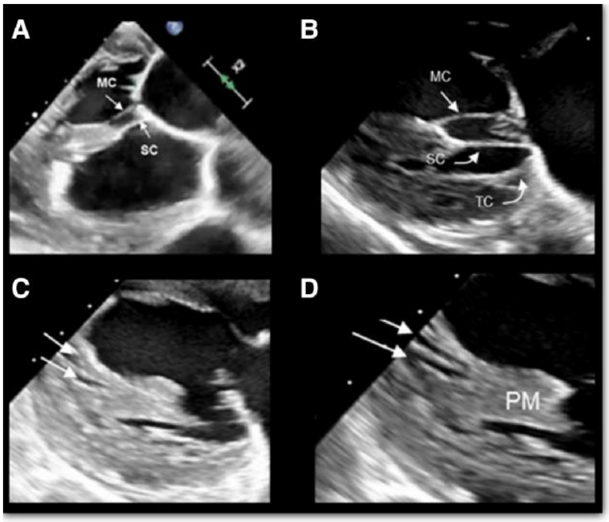

Key points

Knowledge of the 3D TOE features of normal MV anatomy is a prerequisite for a correct interpretation of the wide spectrum of MV diseases.

The MA can be divided into an anterior and a posterior segment. The posterior segment is made up by a discontinuous string of fibrous tissue, interspersed with adipose tissue. The anterior segment is the insertion on the anterior leaflet in continuity with the mitral–aortic curtain.

Two main commissures separate the MV in two leaflets. The AML is a single veil, while the PML is divided by indentations into three (or more) sub-segments called scallops and labelled P1, P2, and P3. On their ventricular aspect, each leaflet is divided into a rough and clear zone. On their atrial aspect, the rough zone corresponds to the coaptation surface.

The 2D TOE image derived by the 3D data set is a valuable modality for visualizing chordae tendineae especially when acquired in the trans-gastric views.

PMs do not arise as a single pillar from a compact myocardium, but rather from a network of trabeculations. with several branches.

3D TOE acquisition and display modalities

The ‘dynamic’ nature of MVR requires an imaging technique capable of high spatial resolution (to identify the fine morphological details of the valve) and a high temporal resolution (to allow an accurate frame-by-frame analysis). The best modality for acquisition remains a ‘zoom’ ECG-gating multi-beat acquisition (see paragraphs of basic physic). This is particularly true when colour Doppler is used. Currently, the single-beat zoom modality acquisition may also reach an acceptable temporal resolution (up to 25 volume/s), while the temporal resolution zoom single-beat colour Doppler still remains usually below 20 Hz.

There are several modalities for displaying 3D TOE images of MVR. These modalities are summarized in *Table 8*.

Table 8

Displaying modalities	Image description	Image
Perspectives Currently, the 'surgical view' remains the most intuitive view and, hence, the most used. However, once the volumetric data set has been acquired, the 3D image can be observed from countless perspectives. 'We strongly' advise the use of the so-called angled or tangential views.[18] These views may better clarify the entity of protrusion above the annular plane (which may be misjudged using surgical views only) or discover small lesions localized in commissural areas.	**Image A** 3D TOE surgical view. Barlow's disease with multiple ruptures of chordae tendineae (arrows). **Image B** Same data set in a tangential view (left to right). This perspective improves the perception of leaflet protrusion above the annulus (asterisk).[18] **Image C** Angled view with the AO 'en face'. This view shows the anatomical regurgitant orifice (arrow). **Image D** Angled view showing the anterolateral commissure (arrow). CS, coronary sinus.	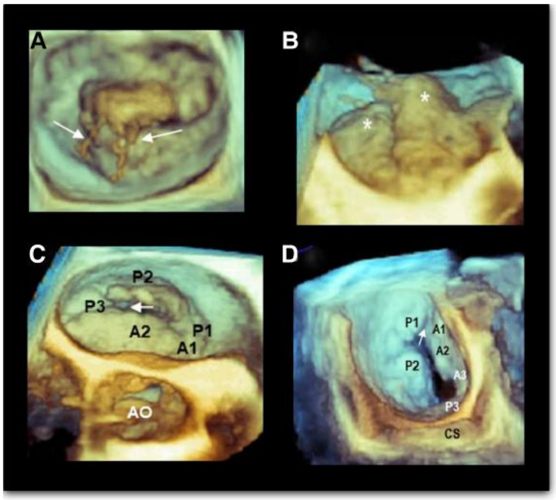
Photorealistic vision This new algorithm uses a free mobile source of light and is able to 'illuminate' the valve from different perspectives creating shadows to improve the perception of depth. Although at first sight, images may appear impressive, it must be stated that there are no data nor a systematic investigation which shows the advantages of these new display algorithms vs. the 'classic' volume rendering modality.	**Image A** P2 prolapse with ruptured chordae. The source of light 'illuminates' the prolapse from above allowing a clear definition of its size and shape. **Image B** Barlow's disease. The lateral illumination improves the perception of multi-scallop protrusions (asterisks). **Image C** Functional mitral valve regurgitation (MVR). The source of light is located behind the valve in diastole. The full opening of the valve is clearly defined. **Image D** Same case in systole. The anatomical regurgitant orifice is clearly visible (asterisk).	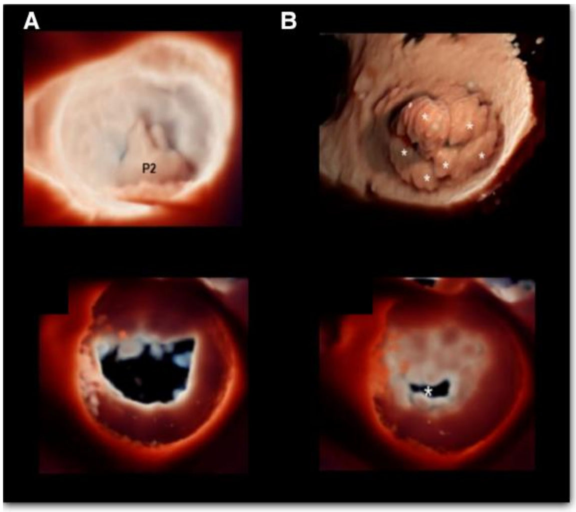
Glass (transparency) vision This tool allows the operator to adjust the degree of transparency of both cardiac and extra-cardiac structures.	**Image A** 3D TOE surgical view showing a P2 prolapse glass (transparency) display. The image clearly shows the protruding prolapse and the ruptured chordae (arrow). **Image B** 3D TOE surgical view showing Barlow's disease. The image clearly shows the multi-scalloped protrusion of leaflets (asterisks).	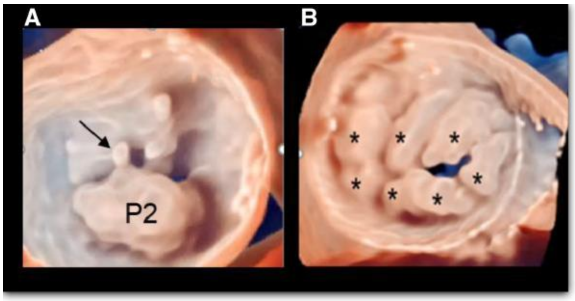

Continued

Table 8 Continued

Displaying modalities	Image description	Image
Surface rendering modalities Generally, the 3D patho-anatomic features of the valve are described qualitatively relaying on the visualization of an experienced observer. Dedicated quantitative software can digitally reconstruct a precise three-dimensional parametric map of the entire valve. This modality overcomes the limitations of a qualitative interpretation/description. The use of this multi-parametric map may improve the accuracy, reliability, and interobserver variability amongst novice readers.	**Image A** The image shows different surface rendering modalities. This software allows either manual or semiautomated tracking of the hinge line and leaflets visualized on 2D slices (derived by 3D data sets), providing relevant quantitative parameters such as the circumference and the height of the saddle-shaped annulus, as well as the height, length, areas, and volumes of prolapsing tissue. The same measurement can be done in functional MR.	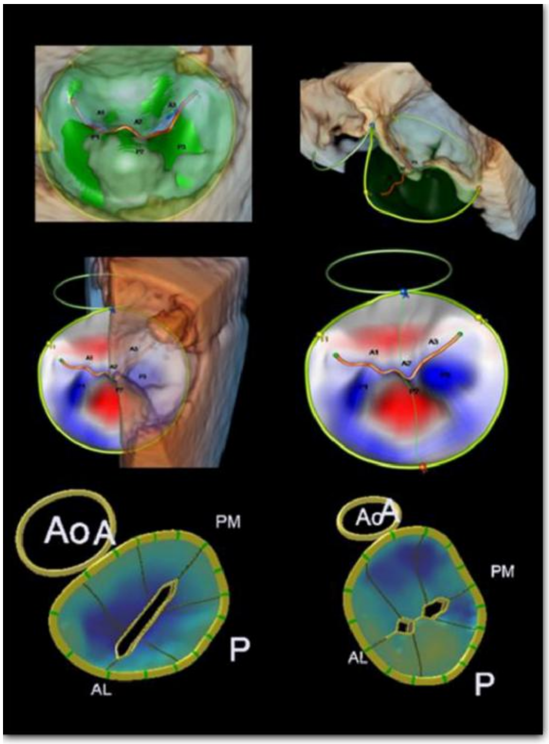

Key points

The best modality for acquisition of MV is a 'zoom' ECG-gating multi-beat modality which allows the highest spatial and temporal resolution.

The 'angled or tangential views' should be used to better clarify the entity of protrusion above the annular plane (which may be misjudged using surgical views only) or discover small lesions localized in commissural areas.

New algorithms using a free mobile source of light or changing the degree of transparency may improve the perception of depth. However, there are neither data nor a systematic investigation which shows the advantages of these new display algorithms vs. the 'classic' volume rendering modality.

The use of surface rendering modality (which displays a multi-parametric map) may improve the accuracy, reliability, and interobserver variability especially amongst novice readers.

MV regurgitation

Introduction

MV regurgitation (MVR) is currently the most common disorder in developed countries affecting 2–3% of the general population. Moreover, due to aging and growth of the population, the prevalence of MVR is likely to further increase in the coming decades.[19]

Classification

Clinical practice is still based on three main categories, i.e. MV regurgitation, MV stenosis, and combined stenosis and regurgitation. However, with the advent of MV repair, this classification has shown its own limitations. On the other hand, a detailed description purely based on the anatomical aspects of MV would have been extremely complex and of limited clinical value. Carpentier's functional classification, on the contrary, makes a clear differentiation between 'aetiology' (cause of the disease), 'lesion' (determined by the disease), and 'dysfunction' (resulting from the lesion). Four functional types of lesions have been described on the basis of leaflet's motion: normal motion (type I), increased motion (typed II), restricted diastolic motion (type III A), and restricted systolic motion (type III B).[20]

Table 9 summarized these four different types of MR.

Table 9

Type of dysfunction	Image
Type I **Normal leaflet motion** Leaflet's excursion is normal. '**The aetiology**' is arrhythmogenic (annular dilation induced by AF) or infective. '**The lesion**' consists of annular dilatation or leaflet perforation. '**The dysfunction**' is mitral regurgitation with normal leaflet motion. Of note, cleft and degenerative malcoaptation, i.e. in MAC, is also thought to be part of Carpentier type 1 classification. 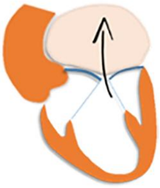 **Image A** 2D TOE showing an example of an annular dilation (dotted double arrow). The arrow points at the gap of coaptation. **Image B** 3D TOE surgical view showing a case of endocarditis with two vegetations (black arrows) and anterior leaflet perforation (white arrow). LA, left atrium; LV, left ventricle; RA, right atrium; RV, right ventricle. 	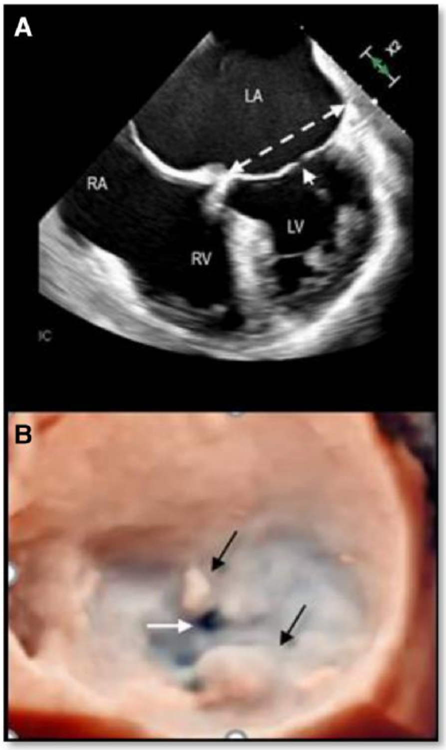
Type II **Increased motion** Leaflet excursion is excessive. '**The aetiology**' may be fibroelastic deficiency, myxomatous degeneration, endocarditis, trauma, PM rupture due to acute/subacute myocardial infarction, or other rare causes. '**The lesion**' consists of a prolapse of one or both leaflets, rupture of chordae, or PMs (associated with flail leaflets). '**The dysfunction**' is mitral regurgitation with excessive leaflet motion. 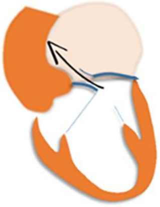 **Image A** 3D TOE surgical view showing a prolapse of P2 with ruptured chordae (arrow). **Image B** The corresponding surgical aspect. The arrow points at the ruptured chordae. **Image C** 3D TOE surgical view of Barlow's disease. **Image D** The corresponding surgical view.	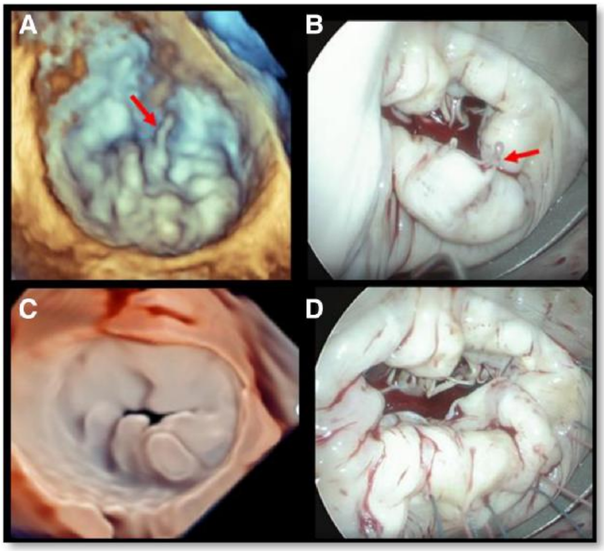

Continued

Table 9 Continued

Type of dysfunction	Image
Type III a **Restricted opening** Leaflet excursion is reduced in both systole and diastole. '**The aetiology**' is rheumatic or congenital. '**The lesion**' is fibrosis/calcification of both leaflets. '**The dysfunction**' is reduced leaflet motion with various degrees of stenosis and insufficiency. 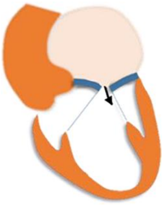 **Image A** Diastolic frame of 3D TOE image in cross-section. **Image B** Same case from the ventricular perspective. Both images show leaflet restricted opening.	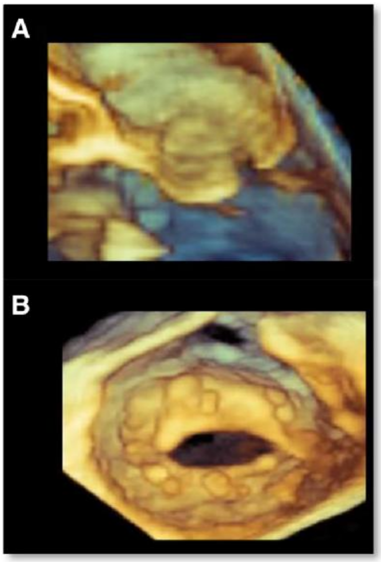
Type III B restricted leaflet closure Leaflet excursion is primarily reduced in systole. '**The aetiology**' is ischaemic, infective (myocarditis), or idiopathic. '**The lesion**' is wall motion abnormalities and/or dilatation resulting in tethering of the leaflets. '**The dysfunction**' is a variety of regurgitation degrees. 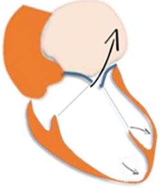 **Image A** 2D TOE long-axis view showing multiple wall motion abnormalities (white arrow). The red arrow points at the gap of leaflet coaptation. **Image B** Same case of image A. The colour Doppler shows severe mitral regurgitation. **Images C and D** 3D TOE surgical view in diastole (image C) and in systole (image D) showing the severe gap of coaptation affecting the entire line of coaptation (asterisks).	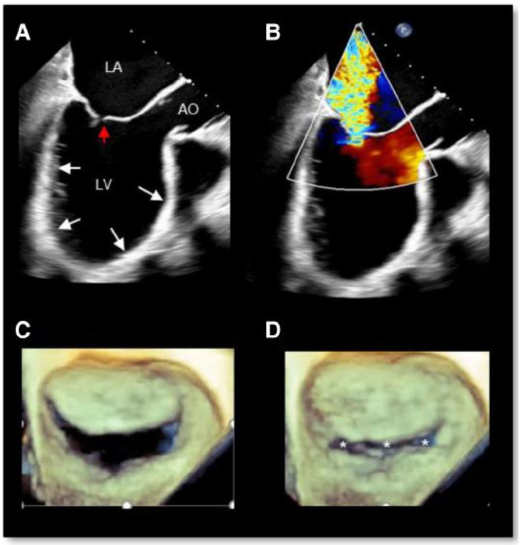

MV regurgitation

MVR can be classified as 'primary' or 'organic', defined as a primary abnormality of the MV apparatus, and 'secondary' or 'functional', defined as a disease of the atrium (atriogenic MVR) or ventricle (ventricular MVR) causing MVR which is not caused by intrinsic MV disease but rather secondary to changes in the atrium or ventricle.

Primary (organic and degenerative) MR

The primary MR includes a wide spectrum of pathological conditions affecting primarily MV leaflets and chordae tendineae. This lesion corresponds at type II Carpentier functional classification. Four morphological phenotypes based on the progression of redundancy of the valve tissue have been described:[21] (i) fibroelastic deficiency, (ii) fibroelastic deficiency plus, (iii) forme fruste, and (iv) Barlow's disease. While 2D TTE/TOE is essential as the first-line imaging technique, 3D TOE provides exquisite images of these four phenotypes (*Table 10*).

In recent years, mitral annular disjunction (MAD), defined as an atrial displacement of the PML hinge point, has gained interest in cardiology community for its association with arrhythmogenic MVP.[22] However, the demonstration of pseudo-MAD, and the high prevalence of MAD in normally structured MV,[23,24] has risen the debate whether MAD is an abnormal or normal feature. 3D TOE enables visualizing the MAD from a ventricular perspective and analysing the circumferential extension of MAD in multiple reconstructed radial planes around the long axis of the left ventricle (LV).[25] However, the role of 3D TOE on this normal/abnormal MV finding needs further studies.

Table 10

Type	Image description	Image
Fibroelastic deficiency (FED) FED is characterized by a deficient production of collagen, elastin, and proteoglycans. Leaflets preserve their own three-layer arrangement, but at surgical inspection, they appear thin and translucent.	**3D TOE surgical view** The image shows the P2 flail due to FED. The arrow points at a ruptured chord. Either the prolapsing/ flail segment (P2) or the remaining valve tissue is not redundant.	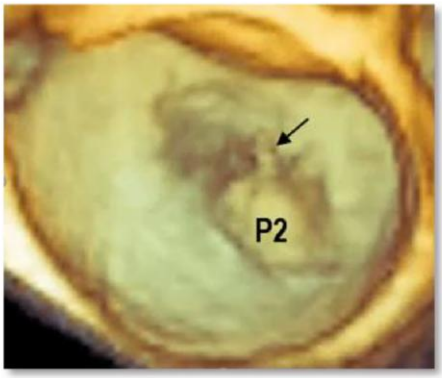
FED plus The prolapsing/flail segment is redundant and affected by myxomatous degeneration. It has been suggested that FED plus may be considered a sort of 'worsening stage' of the FED, rising the hypothesis that the myxomatous changes could also be secondary to jet lesions.	**3D TOE surgical view** The image shows a large P2 flail with redundant tissue. The arrows point at ruptured chordae tendineae.	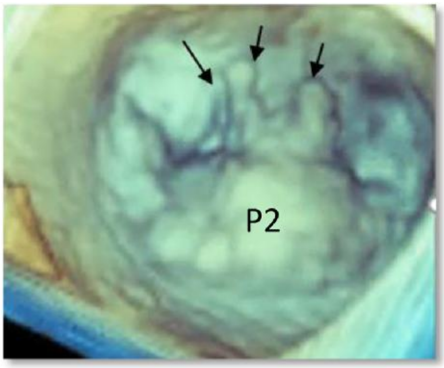
Forme fruste This phenotype has some but not all pathologic features of Barlow's disease. Indeed, the macroscopic Barlow's aspect of the valve (thick and redundant leaflets) with myxomatous degeneration affects the entire posterior leaflet (P1, P2, and P3) but not the anterior leaflet. It has been considered as an incomplete Barlow phenotype confirming that degenerative MV regurgitation includes a spectrum of progressive lesions.	**3D TOE surgical view** The entire posterior leaflet (P1, P2, and P3) is prolapsing with redundant tissue.	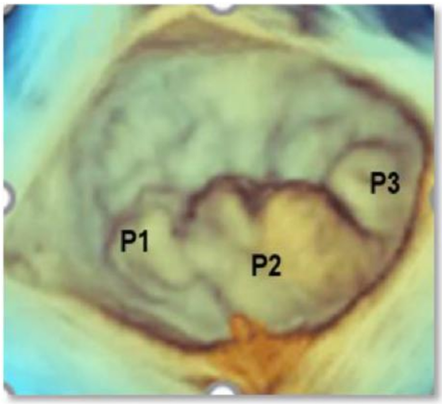
Barlow's disease This phenotype is the result of an abnormal accumulation of myxoid substance (mainly proteoglycans) into the spongiosa layer and a disruption of collagen tissue of the fibrosa layer. The three-layered arrangement of leaflets is lost. The macroscopic appearance is that of thick, bulky, redundant leaflets, elongated and thickened chordae tendineae, and annular dilatation. The excess in leaflet tissue leads to lack of coaptation and consequent MR (with or without ruptured chordae).	**3D TOE surgical view** The image shows a multi-scallop prolapse due to Barlow's disease. Either the anterior (A1, A2, and A3) or posterior (P1, P2, and P3) is thick and redundant.	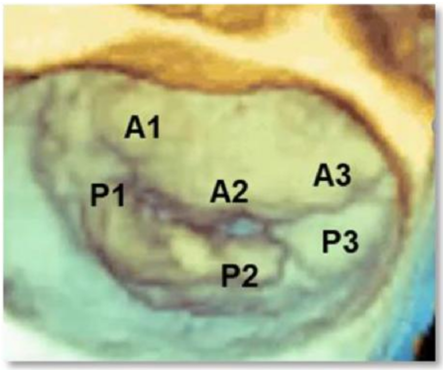

Key points

Carpentier's functional classification is the most practical approach making a clear differentiation between 'aetiology' (cause of the disease), 'lesion' (determined by the disease), and 'dysfunction' (resulting from the lesion).

Four morphological phenotypes based on the progression of redundancy of the valve tissue have been described: (i) fibroelastic deficiency, (ii) fibroelastic deficiency plus, (iii) forme fruste, and (iv) Barlow's disease.

3D TOE is the best method for imaging the four phenotypes.

Chronic secondary (functional) MR

Chronic secondary (functional) MR is usually due to an imbalance between two competing forces: trans-mitral closure forces which are generated by intraventricular pressure and tethering forces exerted by the displaced PMs. Two subgroups of patients can be distinguished on the basis of the tethering patterns, different degrees of local and global LV remodelling, and characteristics of the regurgitant jet: the asymmetric tethering patten and the 'symmetric' tethering pattern.[26] These lesions correspond to Carpentier IIIB functional classification. Isolated left atrial (LA) dilatation due to long-standing atrial fibrillation (AF) and the consequential annular dilation may cause functional MR. This phenotype has been named 'atrial' functional MR[27] and corresponds to Carpentier type I functional classification.

In both cases, the leaflets move apart each other resulting in incomplete coaptation and regurgitation.

2D TOE 'is essential' for defining the pathophysiological mechanism, while 3D TOE may add supplementary qualitative/quantitative data.[28]

Table 11 describes the mechanisms of these two pathological substrates and the corresponding 2D and 3D TOE images.

Table 11

Pathology	Image description	Image
Asymmetric tethering pattern The mechanism of regurgitation consists of a localized wall motion abnormality of the LV, leading to traction on the medial half of both leaflets. This unbalanced tethering force moves the line of coaptation posteriorly creating an image of 'pseudo' prolapse of the AML. Consequently, the direction of the jet is usually directed towards the posterior LA wall.	**Image A** 2D TOE long-axis view, showing asymmetric tethering due to wall motion abnormalities of the posterior basal wall (arrows). **Image B** Same case. The regurgitant jet is directed towards the posterior atrial wall. **Image C** Same case. 3D TOE colour Doppler surgical view. The colour Doppler shows the medial jet origin (arrow). **Image D** Same case from an angled view. The arrow points at the regurgitant jet.	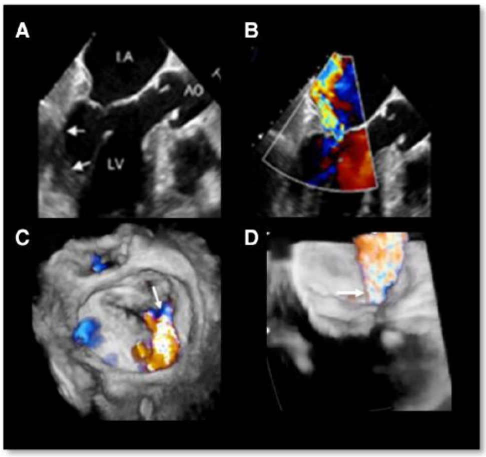

Continued

Table 11 Continued

Pathology	Image description	Image
Symmetric tethering pattern As the LV remodels and dilates, both PMs are displaced outward and downward, resulting in traction of chordae on mitral leaflets in a symmetric fashion causing a gap along the entire coaptation line. The annular dilation and reduced closing forces exacerbate severity of the regurgitation.[29]	**Image A** 2D TOE long-axis view, showing a symmetric tethering due to LV dilatation and PM displacement. The brown area indicates the tenting of leaflets, which is considered an indicator of the tethering forces and sub-valvular distortion. **Image B** 3D TOE volume rendering modality from a ventricular perspective showing a slick-like regurgitant orifice involving the entire line of coaptation. **Image C** Surface rendering modality of the same case showing tenting of the leaflets. **Image D** At the onset of systole, the weak closing forces and strong tethering forces lengthen the time needed for the leaflets to reach their apposition, leading to a significant rise of early systolic regurgitation. **Image E** In mid-systole, at the peak of intraventricular pressure, leaflets reach their maximal possible apposition and the regurgitation decreases. **Image F** At the end of systole, the interventricular pressures are again reduced and the regurgitant flow increases.[25]	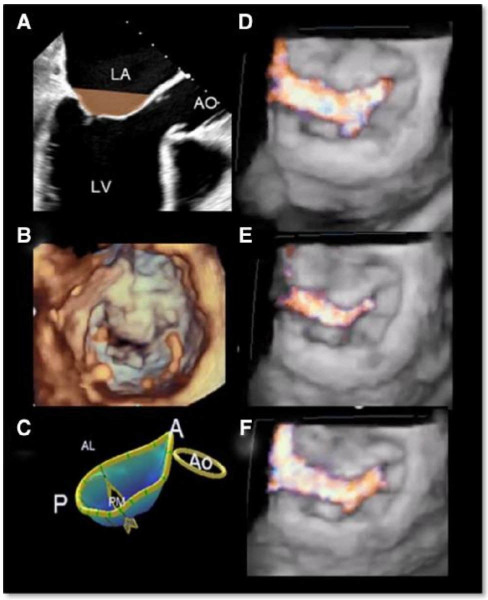
Atrial functional MR In patients with long-standing AF, the atria enlarge and undergo structural remodelling eventually resulting in an 'atrial cardiomyopathy'. Small degrees of annular dilation may be balanced by the natural redundancy of mitral leaflets, whereas large annular dilation gradually moves the MV leaflets apart resulting in inadequate coaptation and regurgitation.	**Image A** '2D' four-chamber view showing a significant LA enlargement. The structures in the red square are magnified in image B. **Image B** The image shows the so-called atriogenic functional MV regurgitation. The LA enlargement displaces the hinge line of the posterior leaflet over the crest of the LV musculature. Because the annulus–papillary distance is augmented, this posterior displacement may result in a lack in leaflet coaptation.	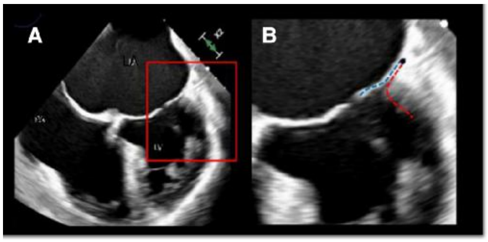

Key points

Functional MR is substantially due to an imbalance between trans-mitral closure forces which are generated by intraventricular pressure and tethering forces exerted by the displaced PMs.

Two subgroups of patients can be distinguished on the basis of the tethering patterns, the asymmetric tethering pattern and the 'symmetric' tethering pattern due to local and global LV remodelling, respectively.

Isolated LA dilatation and consequently annular dilatation (atrial cardiomyopathy) may cause functional MR. This phenotype has been named 'atrial' functional MR.

There is no question that 3D TOE is superior to 2D TTE/TOE imaging in the assessment of degenerative MV regurgitation. *Table 12* shows some examples of the advantages of 3D TOE over 2D TOE.

Table 12

Advantages of 3D TOE	Image
3D TEE has shown that every P2 prolapse appears unique and differs from others by width, length, and location (i.e. more lateral or more medial). **Images A–D** show four different P2 prolapse.	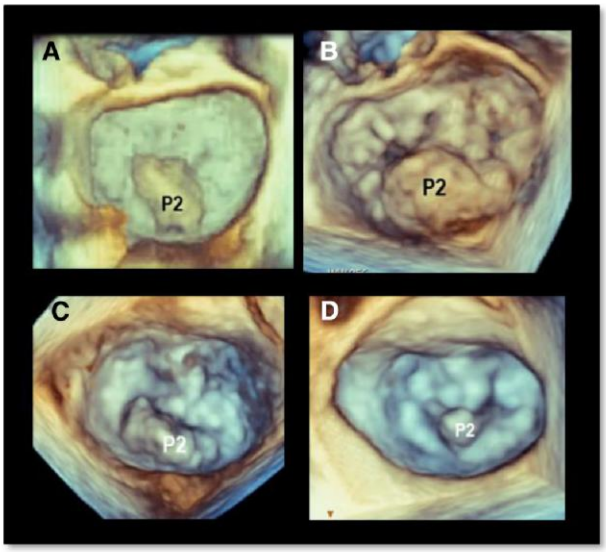
Commissural or P1 and P3 prolapses are more likely to be detected with 3D than with 2D TEE. **Images A and B** show two cases of P3 flail.	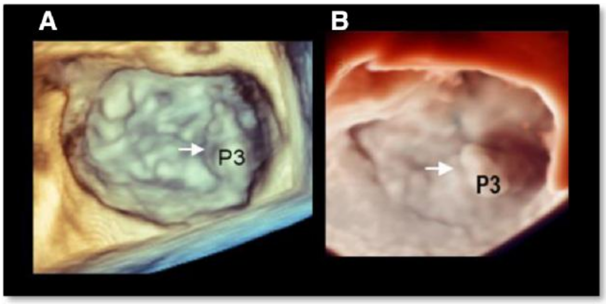

Continued

Table 12 Continued

Advantages of 3D TOE	Image
3D TOE allows easier distinction between indentations (a normal feature of PML) and cleft (pathological). A cleft has the following characteristics: (i) usually extends up to the hinge line, (ii) may divide a scallop into two parts, and (iii) causes regurgitation. **Image A** 3D TOE from a ventricular perspective showing Barlow's disease. The arrows point at the commissures. **Image B** Same case in systole. A cleft divides the AML into two parts (arrow). **Images C and D** 3D TOE surgical view showing Barlow's disease in diastole and systole, respectively. In both images, a deep cleft dividing a large P2 into two halves (arrow). **Image E** 3D TOE photorealistic modality from the atrial perspective. The image shows a large cleft of posterior leaflet (arrow). **Image F** Same case from the ventricular perspective (arrow).	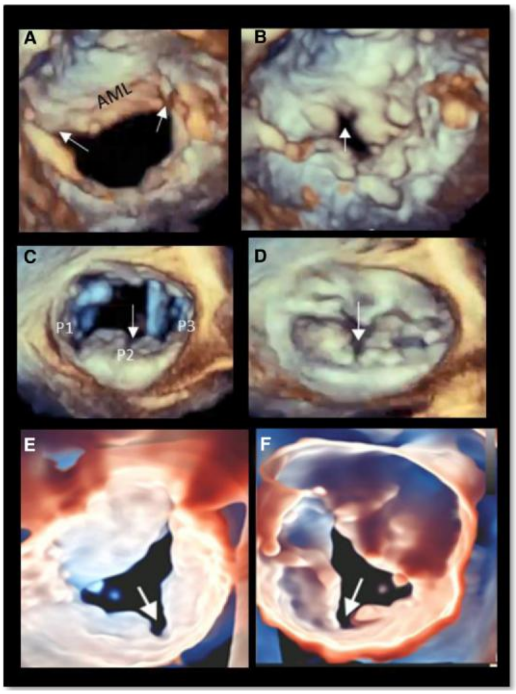
Both in surgical and in percutaneous MVR, 3D TEE allows an easy distinction between an 'ideal' (i.e. single scallop prolapse/flail, tissue exuberance, absence of annular calcification, and moderate annular dilation) and a 'challenging' patho-anatomy (i.e. FED, Barlow's disease, flail of the anterior leaflet, deep cleft, and extensive calcifications). **Image A** Ideal anatomy **Image B** Challenging anatomy (forme fruste)	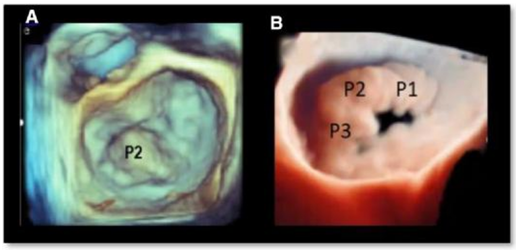
In secondary MVR, 3D TOE colour Doppler may better identify the site and size of origin of the jet. **Image A** shows a regurgitant jet originating from the entire coaptation line. **Image B** shows a regurgitant jet originating from the medial area.	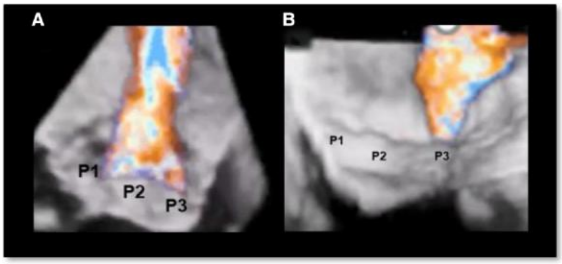
Assessment of 3D VCA This method uses 2D TOE images derived by 3D volumetric data set. Two orthogonal image planes were positioned parallel to the direction of regurgitant jet; a third cropping plane, perpendicularly oriented to the jet direction, was moved along the jet direction until the cross-sectional area at the level of the VC was visualized. The frame with the largest VCA in systole is measured by direct planimetry of the colour Doppler flow signal.	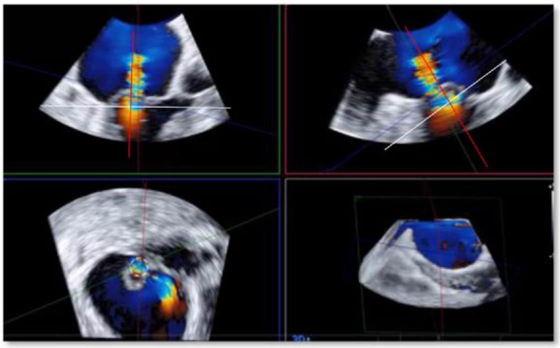

Assessment of mitral regurgitation

Current guideline recommendations are mainly based on 2D images for the quantification of the regurgitation.[30] In this setting, 3D TOE is an additional method providing the following advantages:

(a) Biplane mode is suggested as an easy approach to get more accurate measurements.
(b) The site of regurgitation can be better localized.
(c) 3D can be used for quantifying the left ventricular volumes (volumetric methods).

3D vena contracta area (3D VCA) seems to be the easiest method using post-processing images adapting aliasing velocities and the gains.[31] One of the greatest benefits of the method is that 3D VCA assessment is not dependent on any flow or geometric assumption. The accuracy of 3D VCA area and of 3D VCA-derived regurgitant volume has been validated against 2D colour Doppler methods, 2D volumetric Doppler methods, and cardiac MRI.[32,33] It has been shown to be applicable either in cases of eccentric MR jets or in cases with multiple regurgitant orifices. Importantly, cut-off points to differentiate moderate from severe MR have been determined:[34] 3D VCA at a best cut-off value of 0.41 cm^2 yielded 97% of sensitivity and 82% of specificity to differentiate moderate from severe MR. Colour flow sector should be as narrow as possible to improve volume rates. It should also be aligned orthogonal cropping planes along the axis of the jet, and then, the planimetry should be limited to the highest velocity. Both volumetric methods and 3D VCA will grow in importance with improved 3D colour resolution on newer machines/probes (see *Table 12*).

Key points

In degenerative MVR, 3D TOE has the following advantages over 2D TOE.

Every P2 prolapse appears unique and differs from others by width, length, and location.

3D TOE allows easier distinction between indentations (a normal feature of PML) and cleft (pathological).

Either in surgical or in percutaneous MV repair, 3D TEE allows an easy distinction between an 'ideal' and a 'challenging' patho-anatomy.

3D VCA and volumetric methods will grow in importance with improved 3D colour resolution on newer machines/probes.

Mitral stenosis

Mitral stenosis (MS) commonly is the result of rheumatic fever[35] or is due to a massive calcification of the annulus (MAC).[36] Although rheumatic fever remains the predominant cause of MS worldwide, in developed countries, it has been largely replaced by MAC. Rare aetiologies include congenital anomalies (parachute MS), systemic immune-mediated diseases, carcinoid syndrome, and radiation- and drug-induced MV fibrosis.

Table 13 shows a concise description of the morphology of rheumatic and degenerative MS and the corresponding 3D TOE images.

Table 13

Rheumatic MS morphology[37,38]	Image description	Image
Commissural fusion At the commissural level, the anterior and posterior leaflets are physically contiguous with less separation during diastole. The inflamed/oedematous free margin of A1–P1 and A3–P3 scallops form a point of contact which may eventually fibrose and fuse. The same mechanism may obliterate indentations of the posterior leaflet. Over time, the scarring process proceeds in two directions: from the commissures to the midline of the valve and from free margins to the base of the leaflets. Pathologically, three grades of fusion can be described. '**Grade I**' consists of a partial fusion of the leaflet near the commissures, but their free margins can be separated by hooks. '**Grade II**' is characterized by a complete fusion but with a persistent visible line separating the anterior from the posterior leaflet. 'G**rade III**' is characterized by complete fusion with no distinction between leaflets, with or without calcification.	**Image A** 3D TOE from the ventricular perspective. The commissures are fused symmetrically (arrows) as well as indentation of posterior mitral leaflets (asterisks). **Image B** 3D TOE from the ventricular perspective. Grade I of Carpentier's classification (arrows). **Image C** 3D TOE from the ventricular perspective showing grade II of Carpentier's classification. The arrows point at the persistence of the line dividing the A1 and A3 from P1 and P3, respectively. **Image D** 3D TOE from the atrial perspective. Grade III of Carpentier's classification. There is no distinction between AML and PML (double-headed arrow). The fusion forms a 'neo-commissure'. **Images E and F** Extensive calcification (CA) on medial commissure (image E) and on both commissures (image F).	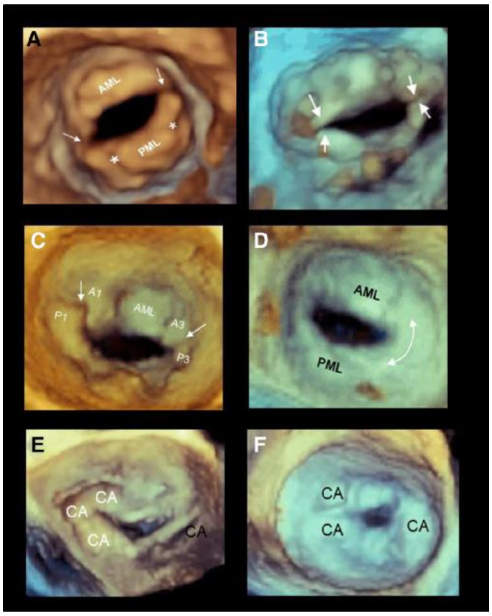
Leaflet morphology '**Anterior leaflet**': the central area of the anterior leaflet is longer and relatively further away from the free margins. As a result, the area is, for a certain period of time, spared from healing/scar/calcifications, preserving a certain degree of pliability and mobility. On the contrary, the free margin is retained by the fusion with the corresponding segment of posterior leaflet. These morphological features determine a diastolic curvature or doming, also known as 'hockey stick' (arrow). 2D/3D TOE clearly shows these changes. The doming morphology of AML means that the leaflet has a preserved pliability and can restore its diastolic excursion, with a significant increase of the valve area once the commissures are split by balloon valvulotomy. '**Posterior leaflet**': because the fusion process affects the indentations between the scallops, 3D TOE shows, either from an atrial or ventricular 'en face' perspective, the posterior leaflet as a continuous immobile scaffold-shaped ridge.	**Image A** 3D TOE apical long-axis view. In this view, the section transects the anterior leaflet through its mid line from the hinge line to the free margin and through the residual valve orifice, showing a diastolic curvature or doming (arrow). The posterior leaflet appears as an immobile scaffold-shaped ridge (dotted line). **Image B** 3D TOE from a ventricular perspective. The 'doming' of the AML is closer to the observer than the other parts of the valve and assumes a beige colour. The surrounding regions farther away are coloured with a mix of brown/bronze colour. This combination provides the perception of the doming (dotted curved line).	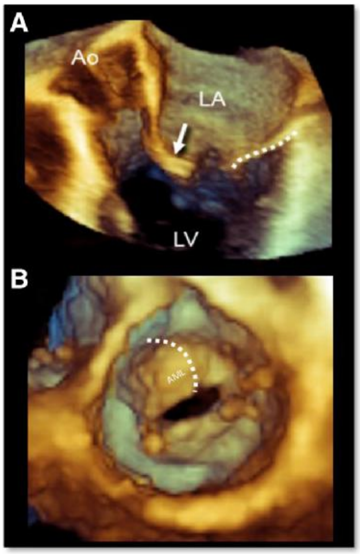

Continued

Table 13 Continued

Rheumatic MS morphology[37,38]	Image description	Image
Calcifications Calcifications are the last step of the healing process. They can be noted on the leaflets and on the annulus. Particularly relevant are calcifications in the commissures which may prevent splitting or may cause leaflet rupture during percutaneous balloon valvuloplasty. Note that in 3D echocardiography, the shades of blue/bronze dual colour are used to provide a perception of depth rather than texture. As a consequence, calcifications sited at the same depth of surrounding non-calcific structures are displayed with the same combination of blue/bronze colour. They can be distinguished from surrounding structures in that they are immobile and protruding. The protrusion, however, is due to a blooming artefact, which makes the calcifications larger than they are in reality.	**Image A** 3D TOE surgical perspective showing two calcifications (red circle) that appear protruding into the LA. **Image B** The image shows the same valve excised after surgical replacement. It is clear that calcifications (white circles) are smaller and less protruding (with the permission from Faletra et al. Real time 3D interventional cardiology page 83 Springer Varalg publisher London 2014).	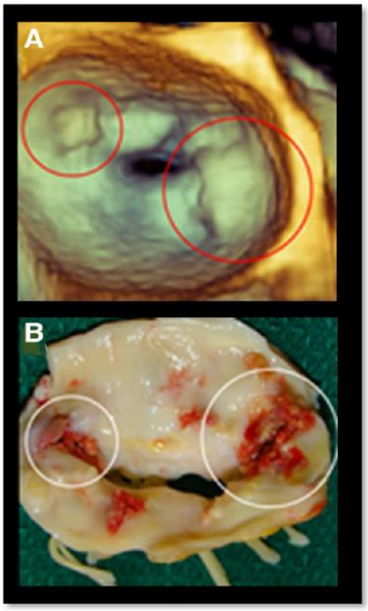
Degenerative MS (MAC) In cases of MAC, calcifications start predominantly along the posterior aspect of the annulus, with extension into the posterior leaflet and further involvement of the anterior leaflet. In degenerative MS, the commissural fusion is almost absent. However, in extremely calcified valve, this distinction may be difficult.	**Image A** 3D TOE surgical view. The image shows extensive calcifications extending into the posterior and into the lateral part of the anterior leaflet (red dotted line) in diastole. The arrows point at the commissure which are partially involved. Thus, the distinction between rheumatic and degenerative is difficult to ascertain. **Image B** Same case in systole.	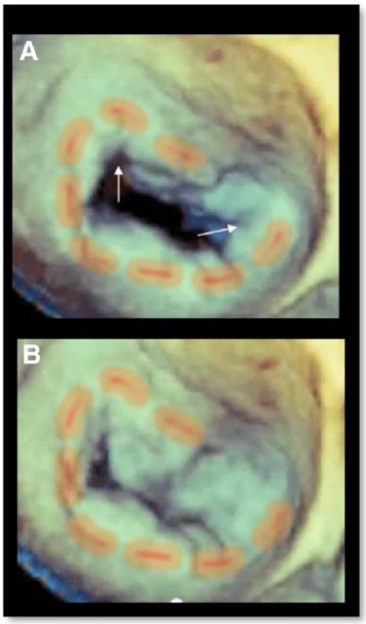

Quantification of severity

3D TOE is probably the most precise tool for assessing MV area with direct planimetry. Whenever possible, zoom modality ECG-gating multi-beat should be preferred, because of its elevated spatial and temporal resolution.[39] In case of arrhythmias, zoom modality in real time (single-beat) can be used. However, in order to maintain an acceptable volume/rate, the sector width should be the narrowest possible including only the MA and the leaflets.

The MV area can be measured using 3D TTE. As expected, the quality of transoesophageal images is significantly better compared with transthoracic images. Nevertheless, a good agreement has been found between the MV area measured with 3D TTE and MV area measured with 3D TOE. Of note, 3D TTE slightly overestimates[40] the MV area by 0.19 cm^2. There are two methods for measing the MV area: the first is using the multiplanar reconstruction, and the second is tracing the planimetry directly on 3D TOE image.[41] *Table 14* illustrates both methods.

Table 14

MS quantification	Image
Multiplanar reconstruction This method uses 2D TOE images derived by 3D volumetric data set. A classic three-step approach is advised: '**Step 1**': two orthogonal 2D planes are oriented perpendicular to the MV obtaining two orthogonal cross-sections in long-axis orientation (90° apart from each other). '**Step 2**': the third orthogonal 2D plane is obtained by positioning the line plane at the level of the tips of leaflets to ensure that the truly smallest orifice is obtained. '**Step 3**': planimetry is traced at the inner edge of the orifice (blood–tissue interface) on a cross-sectional plane during its greatest diastolic opening. Modern software permits multiple short-axis slices to be reconstructed to help identify the narrowest MV orifice.	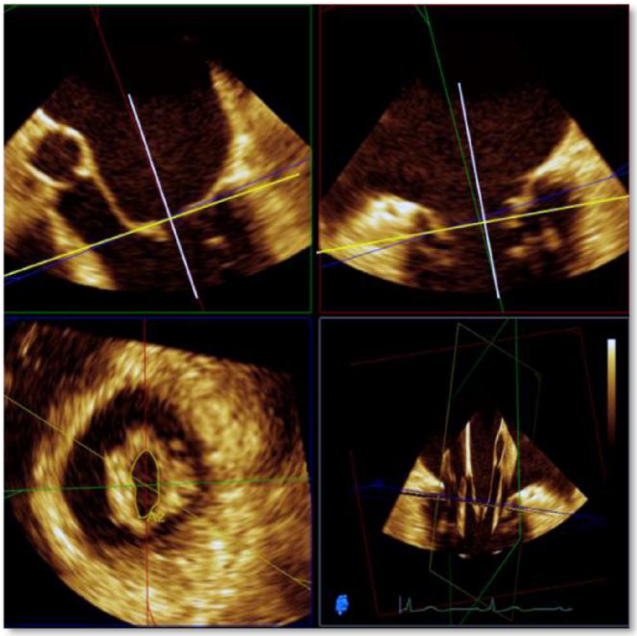
Direct planimetry Although direct planimetry on the 3D images (either from an atrial or from a ventricular perspective) appears to be a practical and appealing method, this approach may lead to inaccuracies specially in highly deformed valves due to the parallax effect. Parallax is the effect whereby the position or direction of an object appears to differ when viewed from different positions. This phenomenon is specific to 3D rendered images. However, in <1.5 cm^2 MV areas, the multiplane reconstruction and direct planimetry on 3D images have given similar results.[41]	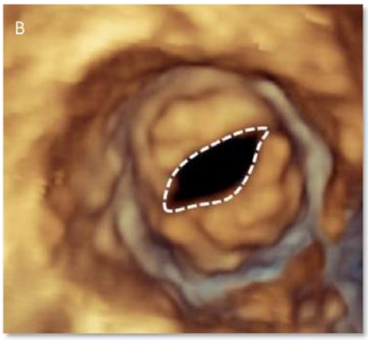

Key points

MS commonly is due to rheumatic fever or is consequent to a massive annular calcification (MAC). Rheumatic fever remains the predominant cause of MS worldwide; in developed countries, it has been largely replaced by MAC.

Rheumatic MS is characterized by (i) commissural fusion; (ii) diastolic curvature or doming, also known as 'hockey stick'; and (iii) calcifications that can be noted on the leaflets, on the annulus, and on commissures.

In MS due to MAC, calcifications start predominantly along the posterior aspect of the annulus, with extension into the posterior leaflet and further involvement of the anterior leaflet. Commissural fusion is almost absent.

3D TOE allows a quantification of MS either by multiplanar reconstruction or by direct planimetry of the 3D image. In valve area, >1.5 cm^2 of the planimetry directly on the 3D image can be affected by the parallax effect.

Section II

Aortic valve

Normal aortic valve apparatus

The aortic root is a highly sophisticated complex anatomical structure that has evolved to fulfil its role functioning properly for a lifetime in the most challenging physical environment. The aortic root includes the ventricular–arterial junction (VAJ), aortic annulus, aortic leaflets, sinuses of Valsalva (SOV), and sino-tubular junction (STJ).[42,43] These individual components function in a co-ordinated fashion to ensure a laminar flow of the ejected stroke volume by minimizing the resistance to flow. During ejection, the three-leaflet morphology of the normal AV allows passage of the stroke volume with least resistance and during diastole forms an effective seal. Preserving leaflet integrity is probably the most relevant function of the aortic root. Indeed, leaflet integrity and durability are highly dependent on the stress applied to the tissue during the closure and opening phases. The aortic root provides an extraordinary 'low-stress environment' that favours leaflet durability.

Table 15 briefly describes the principal features of the aortic root anatomy and the corresponding 3D TOE images.

Table 15

Anatomic description	Image
VAJ The VAJ refers to an area where the LVOT joins the fibroelastic wall of the AO. The VAJ is in part muscular and in part fibrous. The muscular tissue represents nearly 45% of the entire VAJ, while the fibrous component represents the remaining 55% and includes the mitral–aortic curtain and the membranous septum (MS). Interestingly, the muscular component of the LVOT extends few millimetres above the hinge lines of the right coronary leaflet and the anterior part of the left coronary leaflet. The boundary that connects the lowest insertion points of the leaflets to the LVOT is called the 'virtual' annulus since there is no distinct anatomical structure which marks this boundary. **Image A** shows a 3D TOE diastolic frame of the VAJ seen in a normal heart from a ventricular perspective. The red line marks the muscular component, the white line marks the mitral–aortic curtain, and the yellow line marks the MS. **Image B** shows a systolic frame. Please note that in systole, the VAJ assumes a more circular shape. **Image C** shows a 3D TOE still frame image cropped in long-axis view. The black double-headed arrow marks the extension of muscular tissue above the hinge line of the right coronary leaflet (RCL). **Image D** shows the corresponding anatomic image.	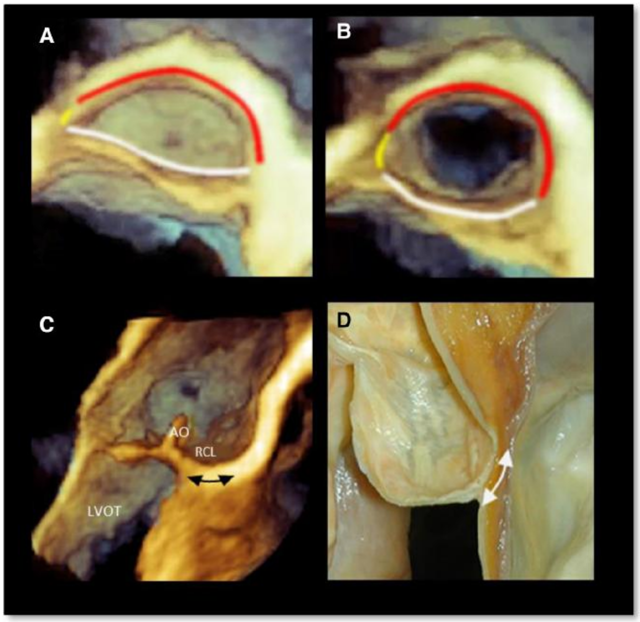
Annulus and interleaflet triangles[44,45] The aortic annulus is a geometrically complex three-dimensional crown-shaped structure. The insertion of the leaflets on the aortic wall, in fact, takes the form of three prolonged coronets with the lowest part (nadir) lying slightly below the VAJ and the highest points joining the STJ. The highest joining point of two adjacent leaflets is named commissure. **Image A** shows 3D TOE of the aortic root cropped longitudinally. The white dotted line marks the crown-shaped aortic annulus with its nadir and commissure. The red line marks the STJ. The interleaflet triangles are triangular spaces beneath each of the three commissures. Although anatomically these triangles are considered part of the aortic root, they are exposed to ventricular pressures because they remain below the aortic valve leaflet hinge line. **Image B** shows the triangle between the left (L) and right (R) coronary leaflets (green area) is usually the smallest, while the triangle between the L and the non-coronary leaflets (N) is in continuity with the mitral–aortic curtain. **Image C** The triangle between the L and the non-coronary leaflets (N) is in continuity with the mitral–aortic curtain. **Image D** The triangle between the N and the R coronary leaflets includes the MS which marks the site of the atrioventricular conduction bundle.	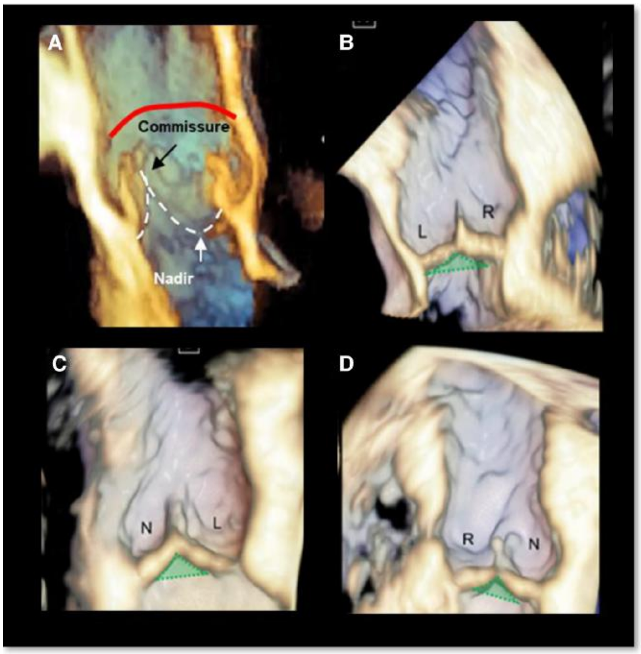

Continued

Table 15 Continued

Anatomic description	Image
The SOV The SOV are bulges of the aortic root, one for each cusp in tricuspid aortic valves. One of the functions of the sinuses is to preserve the integrity of the aortic leaflets. The most peripheral layers of blood flow, sliding along the ventricular surface of the leaflets, encounter, during systole, the 'bottleneck' of the STJ. These layers are then forced back into the space between the open leaflets and the sinuses, creating vortexes that promote a slow and smooth leaflet closure. In diastole, when the blood flow reverses, the distance between the valve leaflets is minimal ensuring a stress-free leaflet closure.[46] **Column A** Four 2D TOE colour Doppler still frames showing the peripheral layers of the blood flow are forced back in the space between sinuses and leaflets, promoting a smooth systolic closure (curved white arrow). **Column B** 3D TOE of aortic leaflets seen from a ventricular perspective. The four still frames show as in systole the area of the aortic valve progressively reduces allowing a smooth closure.	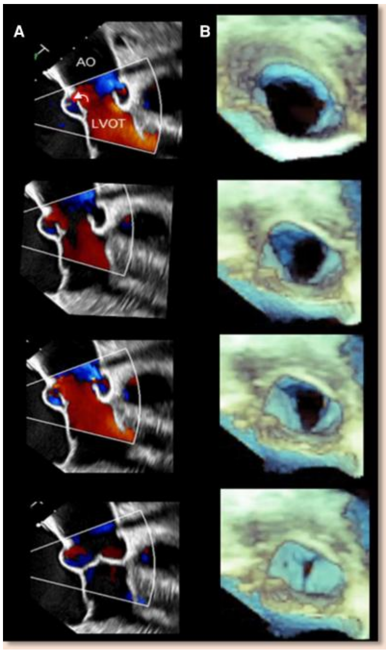
Leaflets The aortic leaflets represent the 'working component' of the aortic root. Each leaflet has several distinct anatomical regions. The hinge line has a crescent shape being part of the crown-shaped annulus. The body is the skeleton of the leaflet bearing the most force in diastole, when the valve is closed. The lunula, which corresponds to ~30% of the leaflet total area, forms the appositional surface between leaflets. In the middle of the lunula at the free margin, there is a thickened nodule called the nodule of Arantius which contribute to a perfect sealing. **Image A** 3D TOE cropped cross-section showing one leaflet 'en face'. The white and red dotted lines mark the three anatomic regions (lunula, body, and hinge). **Image B** 3D TOE cropped cross-section 'oblique' view, showing the three parts of leaflets. The spatial resolution of 2D/3D TOE is not enough to resolve the millimetric nodule of Arantius. **STJ** The STJ is the distal part of the aortic root, between the aortic sinuses and the tubular segment of the ascending AO. Contrary to the other 'virtual' rings, the STJ is a true ring made up by circumferentially aligned fibroelastic lamellae as a mild waist. The diameter of the STJ is about 10% smaller than the annular diameter, so that shape of the aortic root is a truncated cone. Dilatation of the STJ is often the instigating event in the aortic root dilatation causing AR in the elderly, and remodelling the STJ using a graft is a fundamental concept in restoring valve leaflet coaptation. **Image C** 3D TOE cropped longitudinally and displayed in a coronal orientation. The image shows the strict proximity between the commissure and the STJ. **Image D** 3D TOE cropped longitudinally showing two commissural points and the STJ.	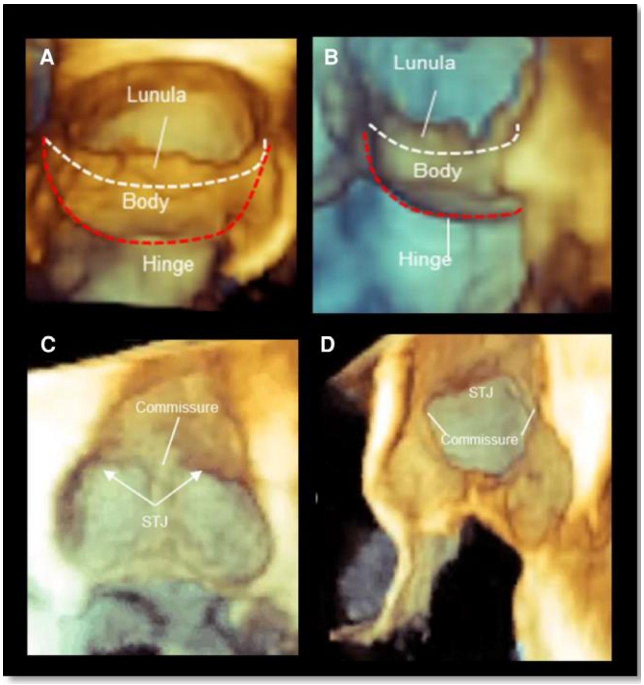

Key points

The ventricular–arterial junction (VAJ) refers to an area where the left ventricular outflow tract (LVOT) joins the fibroelastic wall of the AO. The VAJ is in part muscular and in part fibrous.

The aortic annulus is a crown-shaped structure: the lowest part (nadir) lying slightly below the VAJ and the highest points joining the STJ.

The interleaflet triangles are triangular spaces beneath each of the three commissures. Although anatomically these triangles are considered part of the aortic root, they are exposed to ventricular pressures.

The sinuses of Valsalva are bulges of the aortic root, one for each cusp in tricuspid aortic valves. The main function of the sinuses is to preserve the integrity of the aortic leaflets.

The aortic leaflets represent the 'working component' of the aortic root. Each leaflet has three distinct anatomical regions: the hinge line, lunula, and body.

The STJ is the distal part of the aortic root, between the aortic sinuses and the tubular segment of the ascending AO. Contrary to the other 'virtual' rings, the STJ is a true ring made up by circumferentially aligned fibroelastic lamellae.

The advent of aortic valve-sparing surgery and transcatheter aortic valve implantation (TAVI) techniques has emphasized the interest on the quantification of the aortic root, since both procedures require a systematic and thorough quantitative assessment as well as fine anatomical details of the components of the aortic apparatus. In particular, 3D TOE has been shown to be a valuable imaging technique for patient selection for surgical AV repair and AV-sparing surgery. Measurements listed in *Table 16* allow correct decision-making and planning of surgical procedures in patients with aortic regurgitation (AR) and aortic root disease.

The same table shows the 3D TOE acquisition modality and summarizes most common measurements of aortic root

Table 16

Description	Image
Acquisition modalities **Image A** 2D short-axis imaging of the AV between 30° and 60° or the 110°–120° view from the mid-oesophageal location of the TOE probe is used as the starting point of volume rendering 3D TOE image. The volume acquisition of the aortic root is done after this optimization of the 2D view of the aortic root. The best way for 3D acquisition is the ECG-gated multi-beat acquisition which is able to acquire images with volume rate up to 90–100 MZ. However, when there is irregular cardiac rhythm or pronounced respiratory motion, real-time acquisition yields reliable data albeit with decreased temporal resolution. If need be, a biplane view from the short-axis view of the AV can be used to optimize the long-axis view to target a specific pathology, such as a prolapse of the leaflet.	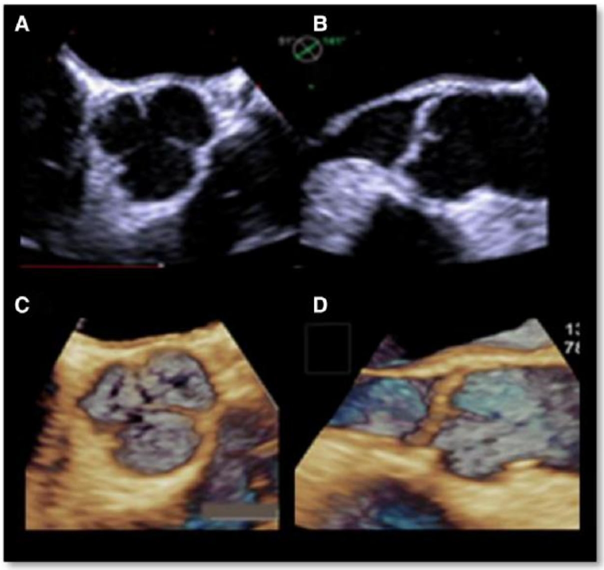

Continued

Table 16 Continued

Description	Image
The virtual annulus[47] The boundary that connects the lowest insertion points of the leaflets to the LVOT is called the 'virtual annulus', since there is no distinct anatomical structure which marks this boundary. The virtual annulus is not circular in most patients. The accurate measurement of virtual aortic annulus is important especially for TAVI planning. 3D TOE is the suggested technique to measure the virtual annulus size in those patients who cannot have contrast CT. Multiplanar reconstruction (MPR) is the proposed method. **Image A** This method provides two longitudinal planes, orthogonal each other (white and green lines), at the end of systole. By adjusting the position of a transverse plane (red line), the aortic leaflets are transected exactly at the level of their lowest hinge points, corresponding to the virtual annulus (red dotted line). Planimetry and measurement of diameters. Minimum and maximum diameters can be obtained. Automated modelling of the aortic root also yields annular perimeter (which is comparable with the manual planimetry in the MPR), the annular area, and minimum and maximum diameters. These measurements are comparable with those taken by planimetry in the MPR. **Image B** shows the automated modelling of the aortic root.	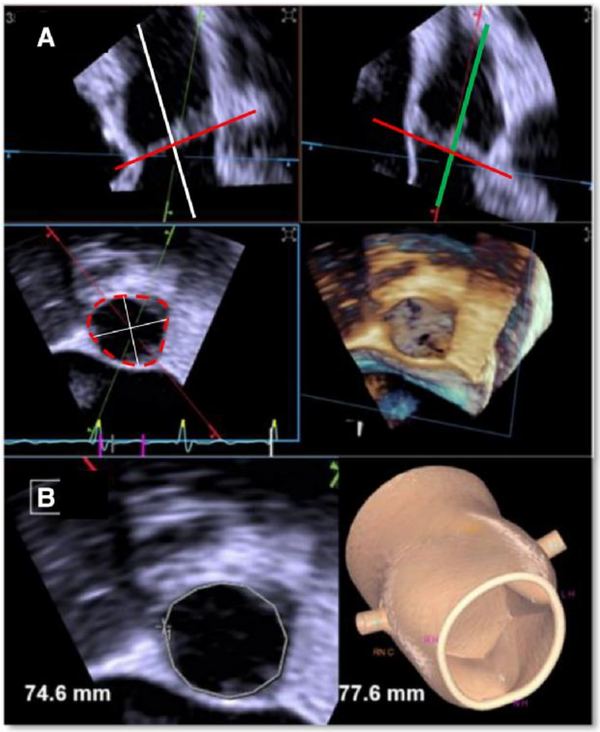
The LVOT The LVOT, like the annulus, is seldom a circular structure. 3D TOE is a good method to obtain the actual LVOT area (and diameters) rather than assuming a circular shape and measuring a single diameter. The area of LVOT can be measured at various distances from the annulus (1–5 mm). The cut-planes are centred in the LVOT to generate a short-axis view of the LVOT. Planimetry is performed in this view to obtain an area of the LVOT, which can be used to compute AV area by continuity equation. LVOT area can also be obtained by automated modelling of the aortic root including the LVOT **Image A** The cut-planes are centred in the LVOT to generate a short-axis view of the LVOT. **Image B** Planimetry and automated modelling of the aortic root including the LVOT. The LVOT area is automatically measured at various distances from the annulus (1–5 mm). The measurement shown here is at a comparable location with the MPR method, and the measurements are similar.	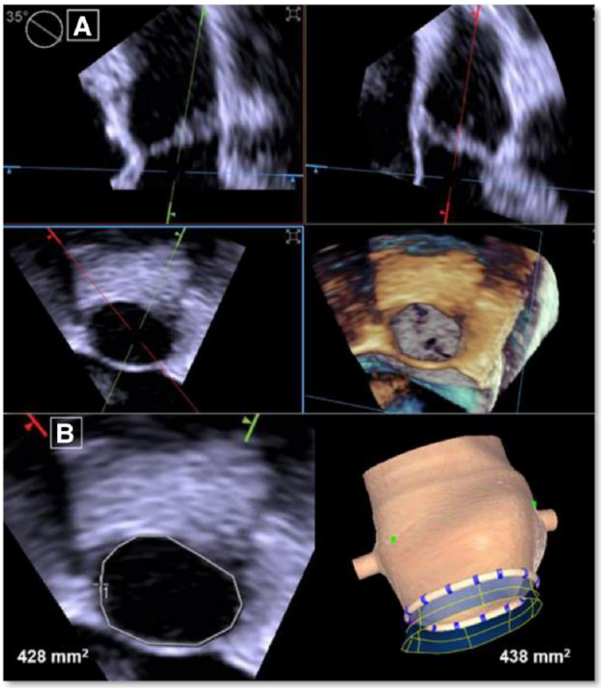

Continued

Table 16 Continued

Description	Image
Valve area MPR from the volumetric data set of the AV is the advised modality to calculate the AV area. Image A The cut-planes are positioned at the leaflet tips to generate the short-axis MPR in which planimetry is done to obtain AV area. Image B Automated modelling can also be used to obtain AV area without the need to position the cut-planes in the MPR. The AV area obtained by this method is comparable with the manual method.	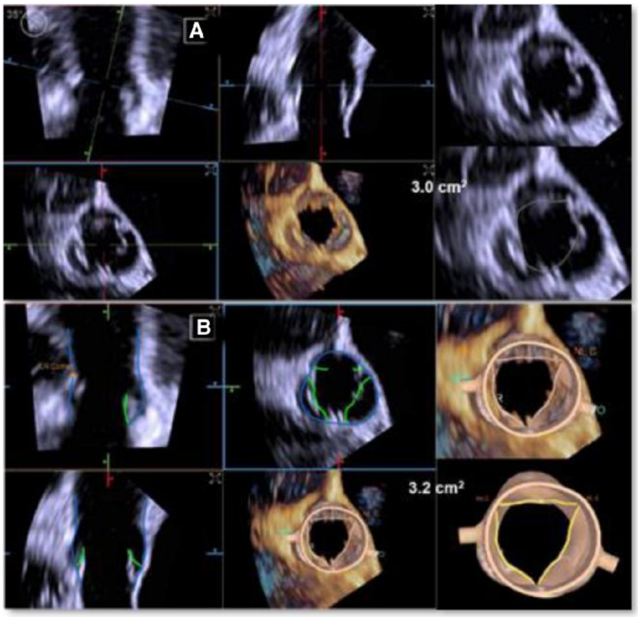
Coaptation height and coaptation zone[47] '**Coaptation height**' is the vertical distance between the aortic annular plane to the tip of the leaflets at coaptation (in diastole). This is usually 7–12 mm and a key determinant of the AO. Indeed, significant AR invariably ensues when it is <4 mm. '**Coaptation zone**' is the leaflet surface of the ventricular side of the leaflets that appose during coaptation. This usually extends 4–6 mm from the free edge of the leaflets. **Image A** shows the coaptation height. **Image B** shows the coaptation zone.	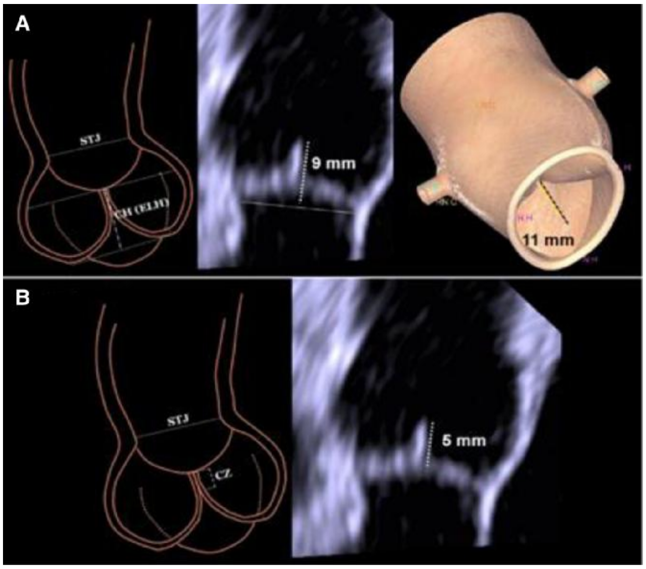

Continued

Table 16 Continued

Description	Image
Leaflet geometric height and free-edge length **Image A** The curved distance along the surface of the leaflet from the lowest insertion point to the free edge forms the geometric height of each leaflet. The normal range is 12–19 mm. **Image B** The free margin or edge length is the distance measured on free margin of each leaflet from commissure to commissure. The lengths shown here are within normal range (26–35 mm). The leaflet height-to-length ratio is an important determinant of occurrence of AR.	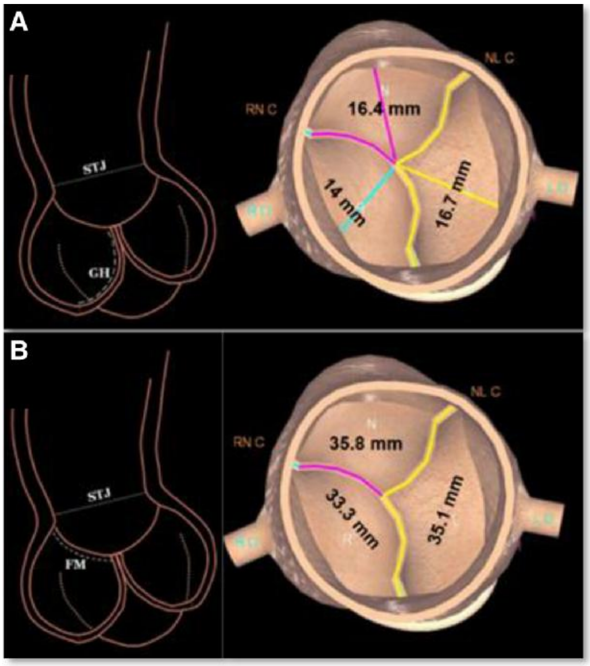
SOV diameters The SOV diameters have important role in preventing trauma to the AV leaflets, and the size is a key measurement to plan TAVI. The diameters are optimally measured from 3D TOE volumetric data set. **Images A, B, and C** show the maximal diameters of the right, left, and the non-coronary sinuses, respectively. In the short-axis MPR views, the red lines extend from the centre of the sinuses to the opposite commissure (cusp-to-commissure diameter). **Image D** shows the measurement of each of the SOV diameters. **Image E** shows the automated modelling from the volumetric data set average area (shown in image); the volume of the sinuses and diameters (not shown) can be measured.	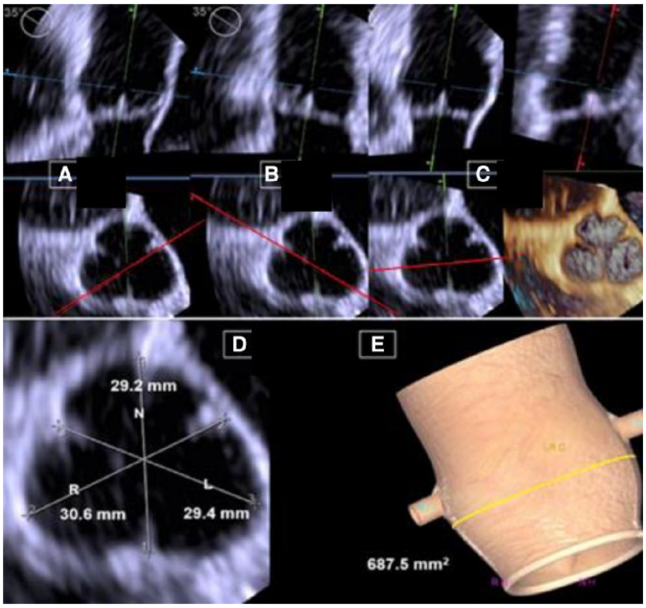

Continued

Table 16 Continued

Description	Image
STJ The size of STJ can be measured manually as area or diameters using the MPRs centred at the STJ. Alternatively, the STJ can be sized by automated modelling from the 3D TOE data. Dilatation of the STJ is often the instigating event in the aortic root dilatation causing AR in the elderly, and remodelling the STJ using a graft is a fundamental concept in restoring valve leaflet coaptation. **Image A** shows the area and diameters of STJ can be measured manually using the MPRs centred at the STJ. **Image B** shows the STJ can be sized by automated modelling from the 3D TOE data.	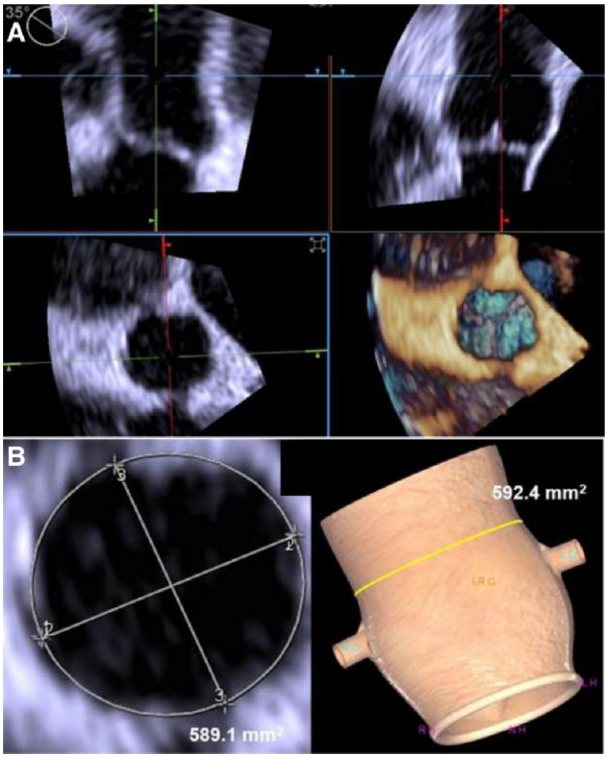
ICD and the coronary ostia height The ICD is best measured by 3D TOE. The average of the three ICDs or the diameter of the best fit circle that includes the three commissures can be used to size the graft during aortic valve-sparing aortic root replacement (VSSR). **Image A** shows the normal values. **Image B** shows the LCA ostia in the MPR (dotted circle). **Image C** shows the height (20 mm) which is higher than the usual normal range. The RCA is not visible in the MPR. **Image D** Both coronary ostia were identified by automated modelling of the root.	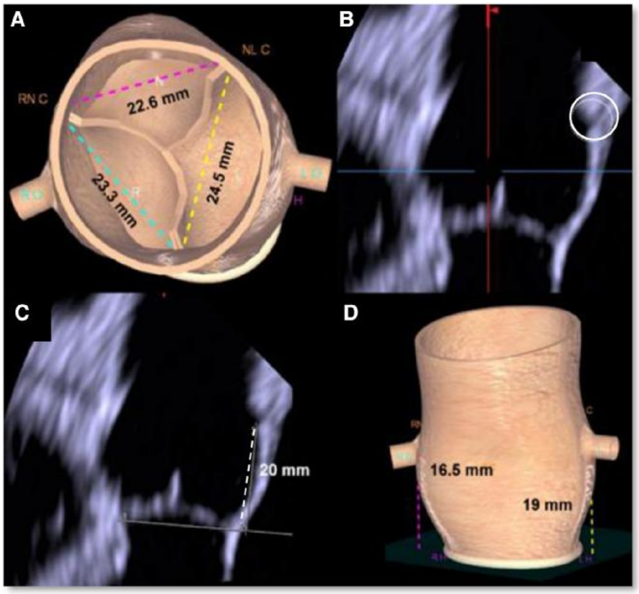

Continued

Table 16 Continued

Description	Image
The aorto–mitral angle The aorto–mitral angle is the angle formed by the aortic and mitral annular planes and can be measured from 3D TOE volumetric data set. Both aortic root and the MA can be modelled from the volume data. The angle can also be measured from the MPR or by the automated modelling method. **Image A** The aortic root and the MA can be measured from MPR or modelled from the volume data. **Image B** shows the relationship of the aortic root and the MV from the posterior–anterior orientation. **Image C** shows the angle formed by the aortic (yellow dotted line) and the mitral annular planes (pink dotted line) as 123° in systole (which is within the normal range).	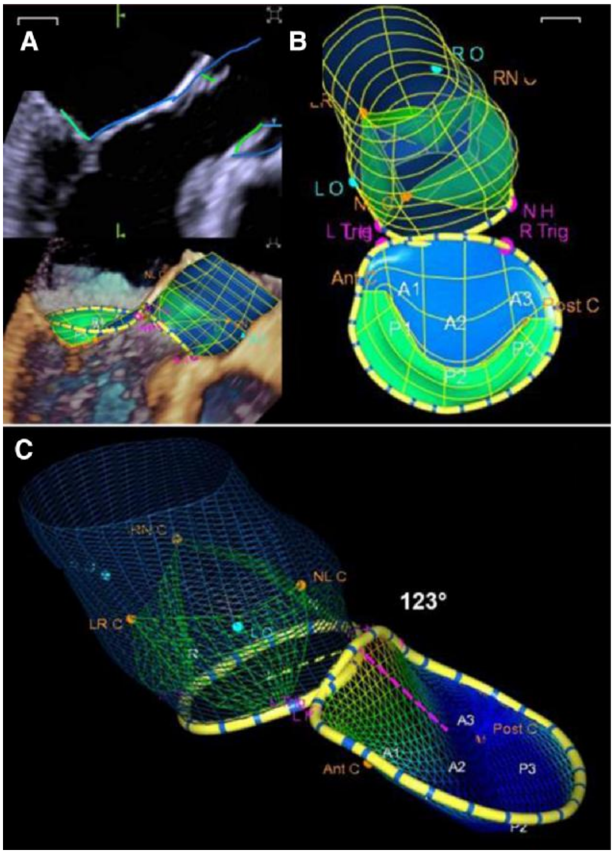

Key points

The advent of aortic valve-sparing surgery and TAVI techniques has emphasized the interest on the quantification of the aortic root.

The boundary that connects the lowest insertion points of the leaflets to the LVOT is the 'virtual annulus', since there is no distinct anatomical structure which marks this boundary.

Several measurements can be done using MPR or various automated modelling systems. These measurements (LVOT, valve area, coaptation height and coaptation zone, leaflet geometric height and free-edge length, sinus of Valsalva (SOV) diameters, STJ, intercommissural distance (ICD) and the coronary ostia eight, and aorto–mitral angle) may have importance in planning aortic valve repair and in TAVI.

Aortic stenosis

The severity of aortic stenosis is reliably determined by 2D TTE, continuous wave (CW), pulsed wave (PW), and colour Doppler. 2D TOE can be used in the setting of non-diagnostic TTE imaging to assess the morphology of aortic valve and aortic root. 'Planimetry' of the aortic valve area (AVA) with both 2D TOE and 3D TOE is accurate compared with CT scan of excided valve.[48–50] However, both 2D and 3D TOE have limitations. Indeed, ensuring that the planimetry is done at leaflet tips can be challenging with 2D TOE and require experience to identify the appropriate plane exactly passing through the tip of leaflets, while the reliability of 3D TOE may be limited in markedly calcified AV. However, new automated 3D TOE software allows accurate modelling and reproducible quantification of aortic annular and root dimensions with high feasibility. An excellent correlation between measurements and the agreement in prosthesis sizing between 3D TOE and multidetector computed tomography (MDCT) suggest the use of 3D TOE in clinical practice as potential alternative to MDCT before TAVI.[49] *Table 17* illustrates the quantitative assessment of aortic stenosis and 3D TOE examples.

Table 17

Description	Images
Planimetry of the AVA **Image A**, top, shows 3D TOE of a calcified AV in the short- and long-axis orientations. The bottom row shows 2D MPR from the 3D data where the cut-planes can be positioned at the tip of the valve leaflets to provide a short-axis MPR (bottom row, right) for planimetry. **Image B** 2D TOE has better spatial resolution than 3D-derived MPR. Of note, the anatomic planimetric area is usually larger than the area derived by the equation continuity and standard severity thresholds for AVA are based on continuity equation assessments.	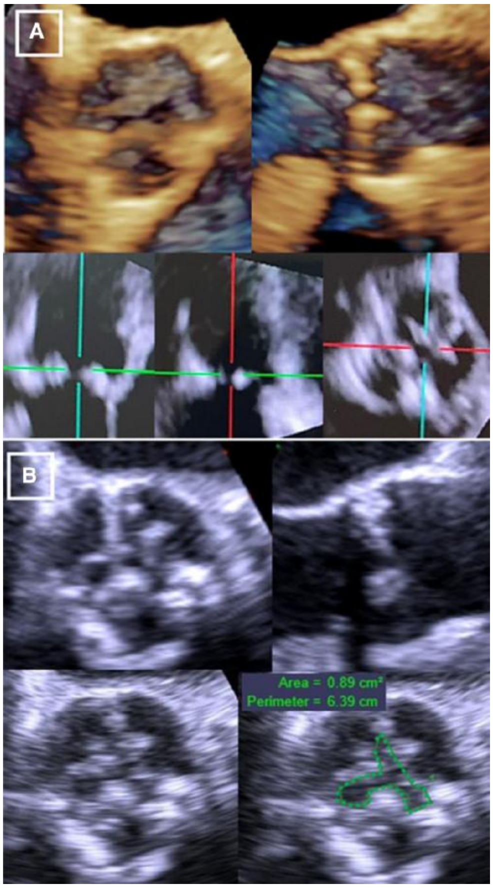
Planimetry of LVOT area 3D TOE can also be used to measure the LVOT area without assuming a circular geometry. Doppler parameters can be combined with 3D LVOT areas to calculate AVA. **Image A** Using MPR data, 3D TOE can measure the LVOT. The location in the LVOT can be specified (distance from the hinge points). The LVOT area in the MPR at that location is shown on the left in the bottom row. The LVOT can also be modelled automatically from the 3D data (on the right in the bottom row) and the area at various distances (green, yellow, and cyan lines represent 2, 3, and 4 mm from the annulus—black arrow) can be automatically obtained.	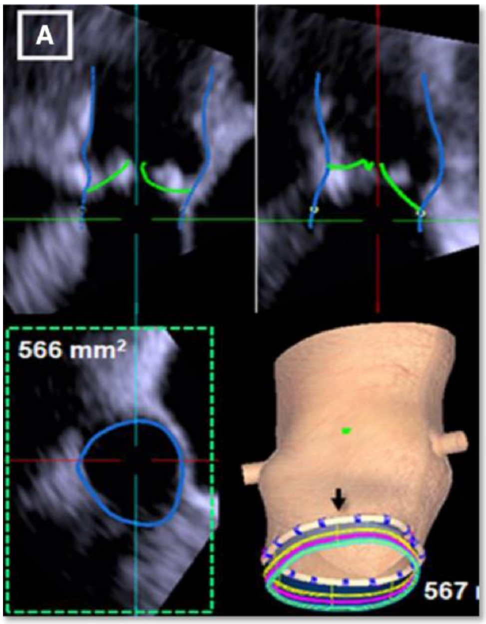

Continued

Table 17 Continued

Description	Images
Planimetry of the virtual annulus 3D TOE can be used to measure the aortic annulus size in those who cannot have contrast CT when planning for TAVI. **Image A** Volume rendering modality. Even though the AV leaflets are not well imaged in calcific AS by 3D TOE, the virtual annulus is usually well seen in the volume data set. **Image B** On the left, automated modelling of the aortic root yields the minimum and maximum annulus diameters and the annular perimeter and area. These measurements are comparable with that obtained with CT (on the right side of the image).	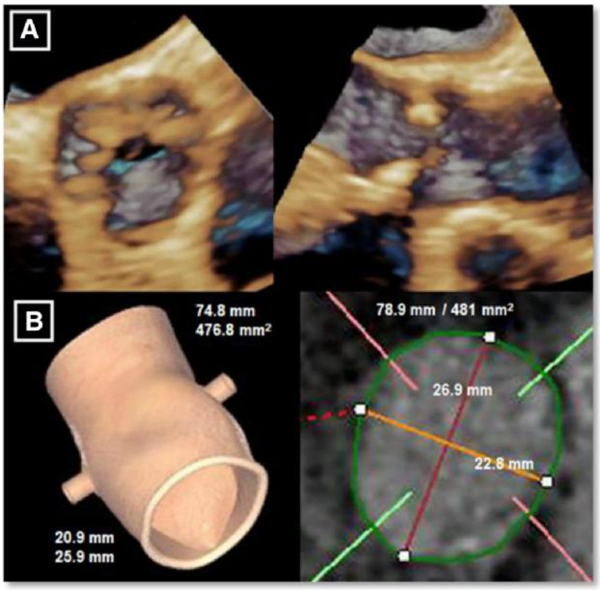

Key points

The severity of aortic stenosis is reliably determined by 2D TTE, CW, PW, and colour Doppler. 2D TOE can be used in the setting of non-diagnostic TTE imaging to assess the morphology of aortic valve and aortic root.

Planimetry of AVA with both 2D TOE and 3D TOE is accurate compared with CT scan of excided valve.

In patients scheduled for TAVI who cannot have contrast CT, virtual aortic annulus can be reliably measured by 3D TOE.

3D TOE can be used to measure the LVOT area without assuming a circular geometry. Doppler parameters can be combined with 3D LVOT areas to calculate AVA.

Aortic regurgitation

The main mechanisms of AR are (i) abnormalities of aortic leaflets and (ii) deformities of aortic root or ascending AO. Other causes of acute AR include infective endocarditis (IE) and aortic dissection.[51]

AR can be assessed with 2D TTE, CW, PW, and colour Doppler. However, 2D TOE images may allow a precise assessment of mechanism of regurgitation and a better definition of eccentric jets. Three main mechanisms of AR have been described:[52]

- Type 1 dysfunction—when the dimensions of any component of the aortic root (aortic annulus, the sinuses of Valsalva, and the STJ) significantly exceeded the upper limits of normal values and no other cause of AR was identified; in this case, the jet is often central.
- Type 2 dysfunction—in the presence of an eccentric AR jet and either a cusp prolapses or a cusp fenestration. In this setting, two types of prolapse could be recognized: (i) complete leaflet prolapse or leaflet flail, when a complete eversion of the leaflet into the LV outflow tract in long-axis views is seen, and (ii) partial leaflet prolapse when the distal part of a cusp was prolapsing into the LV outflow tract. The latter is usually associated with clear bending on the cusp body.
- Type 3 'dysfunction' is considered in the presence of poor cusp tissue quality, including cusp retraction, extensive erosion or destruction due to infective endocarditis, and cusp calcifications (spot, bigger interfering with leaflet motion and extensive producing both stenosis and insufficiency).

Identification of these mechanisms helps in determining the feasibility of the surgical aortic valve repair.

'Congenital bicuspid aortic valve' (BAV) condition is a heterogeneous valvulo-aortopathy. Recently, the International Consensus Classification and Nomenclature for the congenital BAV condition recognizes three types of bicuspid valves.[53]

(1) The fused type is the more common BAV characterized by two of three cusps appearing fused within three distinguishable sinuses of Valsalva. A fibrous ridge (raphe) between the fused cusps is often present. The presence of raphe and the symmetry of the fused type phenotypes are critical aspects to be described.
(2) The two-sinus type (latero–lateral and antero–posterior phenotypes).
(3) The partial-fusion (forme fruste) type.

These phenotypes can be identified with 3D TOE.

Table 18 shows the quantitative assessment of AR and 2D/3D TOE and morphological bases using an automated quantitative modelling of the aortic root. 3D TOE examples of types of AR dysfunctions, BAV, infective endocarditis, periaortic abscess, and aortic dissection follow. In these diseases, 3D TOE plays a major role.

Table 18

Description	Images
Images A and B Real-time 3D TOE provides a method to obtain 3D colour flow data (CFD) in AR. A central jet of AR is seen in both 2D and 3D CFD TOE. **Image C** shows 2D CFD MPRs can be generated at the location of the VC; 3D flow convergence zone [proximal isovelocity surface area (PISA)] is also seen. **Image D** shows the VC area can be identified by the cross-sectional MPR and measured by planimetry. Of note, there are no systematic and reliable data on the use of 3D TOE PISA for assessing the severity of AR.	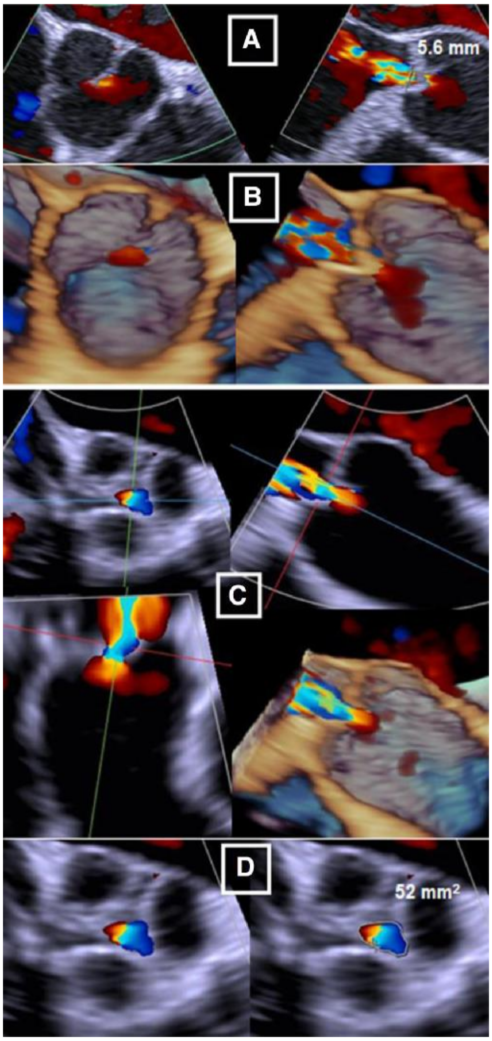
Morphological basis of AR **The image** shows automated quantitative modelling of the aortic root from 3D TOE in normal (left column), dilated root with no AR (middle column), and dilated root with significant AR (right column). The aortic leaflets undergo active remodelling to compensate for increasing ICD. The normal ICD distance is shown on the left column in an individual with no AR. In the middle column, the ICD distance, free-edge length, and the geometric height have increased, to provide an effective seal of the central aortic orifice. This prevents AR when the aortic root is moderately dilated. In the right column, as the aortic root dilates further, the ICD distance and the leaflet free-edge length are progressively increased in an attempt to prevent AR. However, the AV leaflets increase in length, but the compensatory increase in height is limited. This discrepant morphological response results in ineffective sealing in diastole, formation of the regurgitant orifice, and occurrence of AR as shown in the bottom picture in the right column.	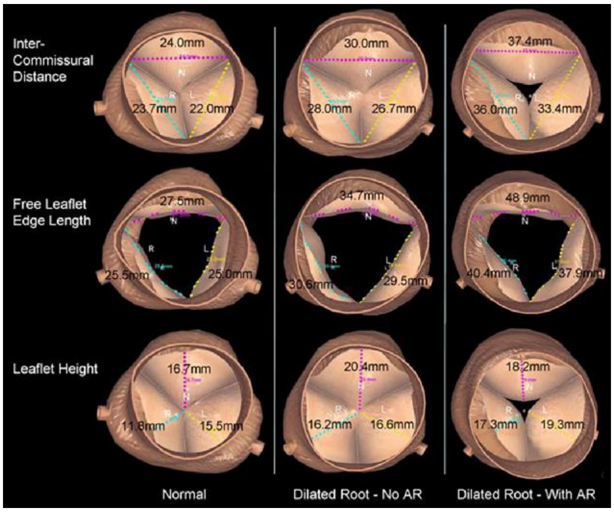

Continued

Table 18 Continued

Description	Images
Type 1 dysfunction **Image A** Dilatation of STJ causing a central regurgitant orifice (arrow). **Image B** The corresponding surgical image.	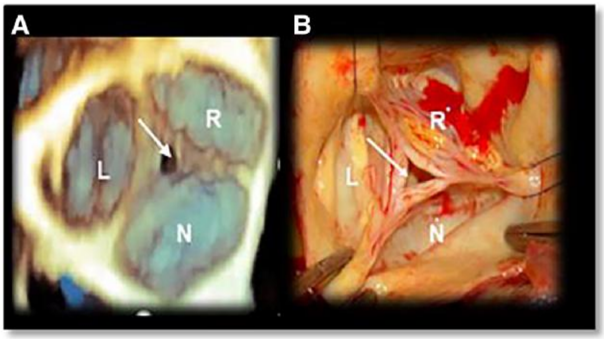
Type 2 dysfunction **Image A** **2D TOE** 2D TOE showing severe AR due to a partial prolapse of the right coronary leaflet. The regurgitant jet hits the body of the AML. **Image B** 2D TOE without colour Doppler showing the partial leaflet prolapse. The red curved arrow marks the direction of the jet which deforms the AML (concave towards the LV). The arrow points at clear bending of the cusp body ('fibrous band'). **Image C** 3D TE long-axis view of the same case illustrated in images A and B, showing the bending of the leaflet extends beyond the cross-section of image B (arrows). **Image D** 3D TOE of aortic leaflets in 'en face' view from the aortic perspective showing the bending extending radially along all the right coronary leaflet. The asterisk marks the regurgitant orifice.	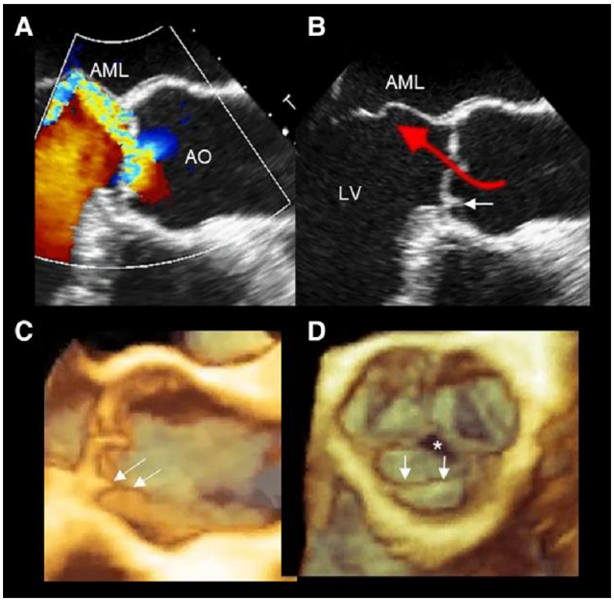

Table 18 **Continued**

Description	Images
BAV **Images A and B** Normal aortic valve with three-leaflet valve in diastole (image A) and in systole (image B); N, non-coronary leaflet; R, right coronary leaflet; L, left coronary leaflet. **Images C and D** Bicuspid valve with two sinuses and two commissures (asterisks) in diastole (image C) and in systole (image D). This phenotype is described as 'two-sinus type' (antero–posterior phenotypes). No raphe is visible. **Images E and F** In the 'fused type', two of three cusps appear fused within three distinguishable sinuses and three commissures (asterisks) in diastole (image E) and in systole (image F). The arrow points at a fibrous ridge (raphe) between the fused cusps. The presence of raphe and the symmetry of the fused type phenotypes are key aspects that need to be described. **Images G and H** Quadricuspid valve in diastole (image G) and in systole (image F). The yellow asterisks mark the four leaflets in diastole. The white asterisks mark the four commissures in systole.	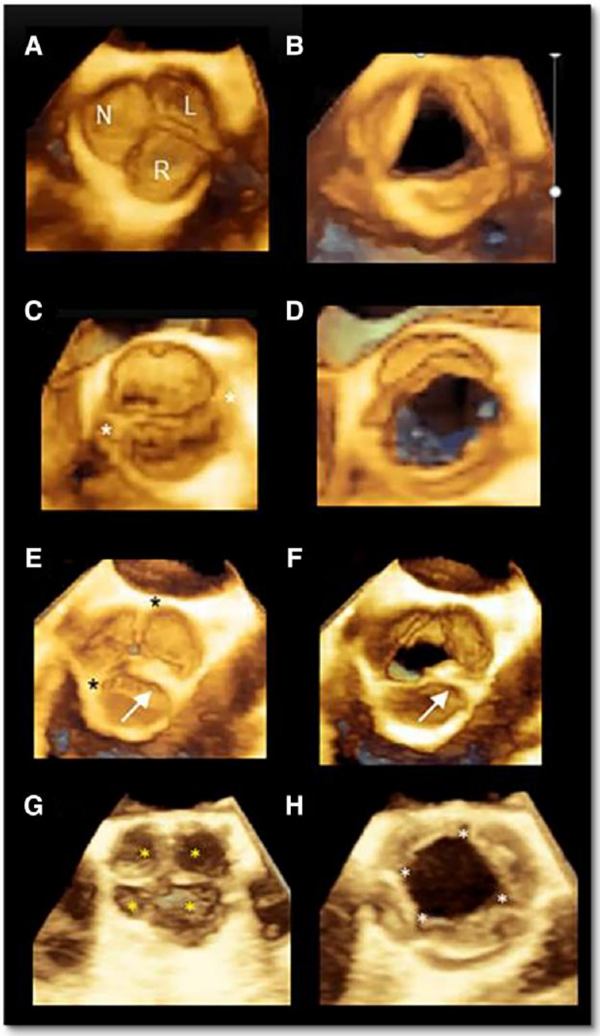
Infective endocarditis **Image A** 3D TOE image of an IE seen in long-axis cross-section. The endocarditis mass is encircled by a red circle. **Image B** 3D TOE image of the same case in 'en face' view from the aortic perspective.	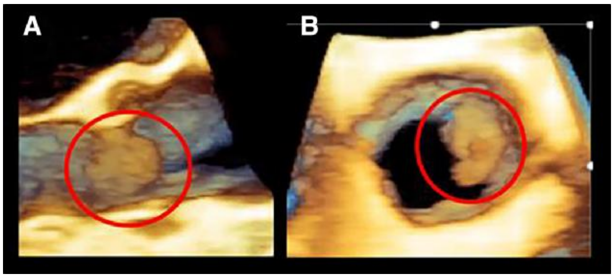

Continued

Table 18 Continued

Description	Images
Aortic dissection Aortic dissection is defined as separation of the layers within the aortic wall. Tears in the intimal layer result in the propagation of dissection due to blood entering into the intima–media space. **Images A and B** Images show a 3D TOE of an aortic dissection in long- and in short-axis views, respectively. 3D TOE allows a 'panoramic' view of the dissection with a visualization of the true (TL) and false (FL) lumen and their sizes. **Image C** 3D TOE long-axis view from upper oesophageal approach. It is clear as the FL is blocked by STJ (Arrow). **Image D** 3D TOE colour Doppler of descending thoracic aorta AO. An entry point between TL and false lumen can be visualized with the colour Doppler (Arrow).	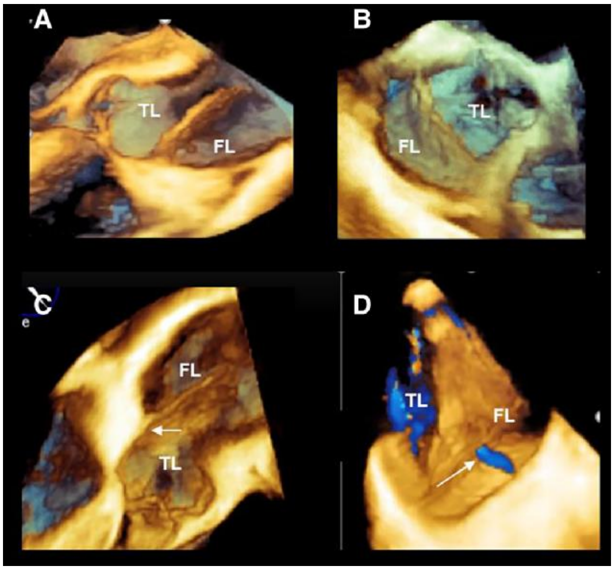

Key points

Three main mechanisms of AR have been described: 'type 1, type 2, and type 3 dysfunction'. Identification of these mechanisms helps in determining the feasibility of the surgical aortic valve repair.

Congenital BAV condition is a heterogeneous valvulo-aortopathy. Three types can be distinguished: (i) the fused type, (ii) two-sinus type (latero–lateral or antero–posterior phenotypes), and (iii) partial-fusion (forme fruste) type. These phenotypes can be identified with 3D TOE.

Causes of acute AR include IE and aortic dissection. In both clinical scenarios, 3D TOE has a relevant role.

Section II

Tricuspid valve

Introduction

Compared with the MV, 3D TOE imaging of the tricuspid valve (TV) is more challenging for the following reasons:

(a) The TV is further away from the transducer location and is larger than the MV. The TV is, in fact, positioned more anteriorly, and the normal TV orifice area is up to 9 cm^2. Consequently, imaging the entire valve from the mid-oesophageal level requires a large field of view. Since in the far field the scan line (and sectors) density is diminished, the spatial resolution and, consequently, the imaging quality of 3D TOE result poorer than that of MV.

(b) The TV is positioned obliquely to the direction of 3D pyramidal ultrasound beam. Thus, the reconstructed image depends less on axial resolution and more on lateral resolution. Moreover, because of their obliquity, the leaflet surface reflects scattered rather than specular echoes. Both these factors contribute to further deterioration of image quality.

(c) Leaflets of the TV are thinner (~ 1 mm) than leaflets of MV. Obliquity and the thinness cause confounding dropout artefacts which adversely affect the optimal visualization of the leaflets.

As for the other valve, this section will begin with 3D TOE images of the normal anatomy of TV.

Anatomy of normal TV

Even though TV is no longer the 'forgotten' valve, its anatomy is still poorly understood. Despite the above-mentioned limitations, 3D TOE plays a major role in defining anatomy/pathology of the TV especially because of its ability to image the valve 'en face' either from an atrial or from a ventricular perspective. These views allow a better identification of the number and location of TV leaflets. Additional tangential/oblique views may also be useful for visualizing morphological details.[54–57]

The major anatomic features (i.e. annulus, leaflets, and sub-valvular apparatus), the display modalities and the corresponding 3D TOE images are illustrated in *Table 19*.

Table 19

Description	Image description	Images
Tricuspid annulus (TA) The TA can be divided into two distinct segments: a C-shaped 'mural' segment which corresponds to the insertion of anterior and posterior leaflets on the free wall of the RV and a shorter straight 'septal' segment, which corresponds to the insertion of the septal leaflet. 'There is not' a distinct fibrous ring that sustains the leaflets. The mural segment consists of the convergence of four components: ventricular and atrial myocardium (with epicardium and endocardium on the left and right sides, respectively), hinge line of tricuspid leaflets, and, externally, the epicardial adipose tissue. The septal segment consists of only the hinge line of the septal leaflet which, posteriorly, lines the inferior margin of the muscular AVS while anteriorly divides the MS into two parts: the atrioventricular and the interventricular MS (images C and D). The TA 'has dynamic structure', having two main systolic motions: 'the sphincteric contraction and the excursion towards the right ventricular apex'. Both these motions are asymmetric, involving predominantly the mural segment. TA is larger at ventricular end-systole/early diastole and during the atrial systole (which allows for large flow volumes under low pressure) and smaller at end-diastole/early systole. The excursion towards the right ventricular apex results in a hinge-like motion of the TA, facilitating passive transfer of blood from the RA to the RV. The mural annulus is undulating, variably inserting either on the RA or on RV, and thus, it is influenced by both RA and RV size and function. The right coronary artery (RCA) runs adjacent to the mural segment. The AV node and the His bundle are located close to the septal segment.	**Images A and B** 3D TOE bi-caval view showing the TV in 'en face' perspective. The red dotted line marks the mural segment. The white dotted line marks the septal segment. It is clear as the sphincteric contraction involves the mural segment (arrows). **Images C and D** show a 3D TOE and 2D TOE trans-gastric view, respectively. Both images clearly illustrate the anatomical relationship between the septal leaflet (S) and the MS (arrow). **Image E** shows a longitudinally cropped 3D TOE image focused on the RA and RV. The images show the longitudinal movement of the lateral TA, with relatively less longitudinal septal annular motion, facilitating passive transfer of blood from the RA to the RV. **Image F** 3D TOE from 'en face' view of the base of the heart. This view shows the four valves: AO, pulmonary valve (PV), MV, and TV. The image shows the anatomical relationship between the septal leaflet (S), the atrioventricular node (AVN), and the His bundle (HIS). Finally, the RCA encircles the mural annulus.	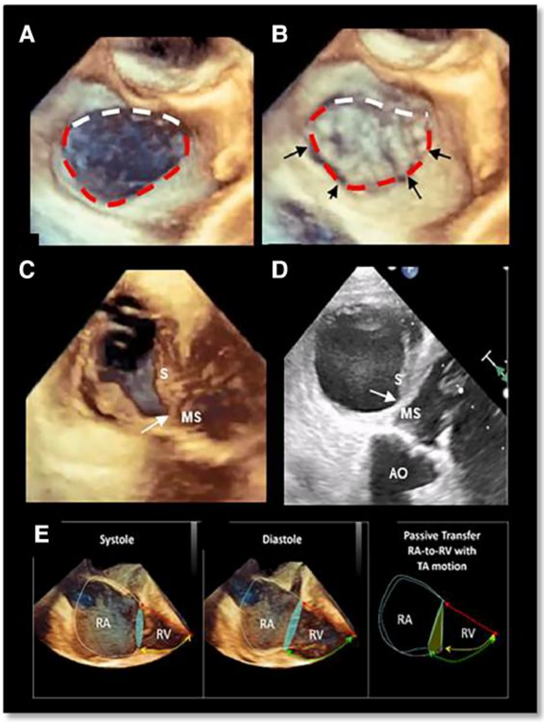 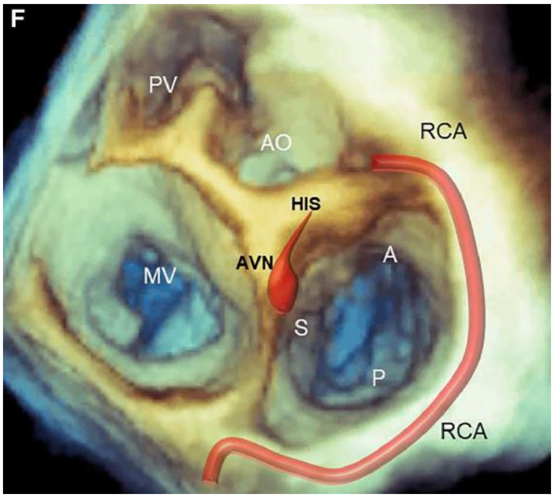

Continued

Table 19 **Continued**

Description	Image description	Images
Tricuspid leaflets The term 'tricuspid' supposes a valve with three well-defined leaflets. This assumption is not always true. Indeed, the pathologic studies have shown a large variability in terms of size and number of leaflets (up to six), and the presence of accessory leaflets is a very common finding. Distinction between leaflets and scallops is challenging with 3D TOE. '**The depth of indentations is the key**'. The 'deep' indentations at the point of junction between leaflets are called commissures and extend up to the TA. Conversely, 'scallops' are divided by 'short' indentations and extend only up to the middle of leaflet tissue. This distinction is not easy to assess with 3D TOE and colour Doppler. Thus, the three leaflets that insert on to the mural annulus can be also considered one single '**mural**' leaflet with three scallops. Since the mural annulus is characterized by significant changes in size during the cardiac cycle, it can be speculated that a 'multi-leaflet' (or a multi-scallop) veil inserted in a high-mobile mural annulus can better adapt to the annular sphincteric motion, ensuring a more effective sealing. Moreover, the short distance between commissures facilitates a complete opening of the leaflet tissue during the diastole. Recently, a novel nomenclature system was described for labelling the tricuspid leaflets and for determining the relative incidence of each morphological type (images A–L).[58] This is not a standard that is widely adapted yet.	**Image A1** shows 3D TOE of TV seen from an atrial perspective (septal, S; anterior, A; and posterior, P). **Image A2** shows a 'quadricuspid' valve. However, the same valve can be considered 'tricuspid' with the posterior leaflet having two scallops (P1 and P2). The four morphological types identified by Hahn et al. are as follows:[50] **Images A and B** 'Type I', three leaflets. **Images C and D** 'Type II', 2 leaflets. **Images E and F** 'Type IIIA', four leaflets with two anteriors. **Images G and H** 'Type IIIB', four leaflets with two posteriors. **Images I and J** 'Type IIIC', four leaflets with two septals. **Images K and L** 'Type IV', >4 leaflets. The incidence of type I morphology was 312 of 579 (53.9%), type II was 26 of 579 (4.5%), type IIIA was 15 of 579 (2.6%), type IIIB was 186 of 579 (32.1%), type IIIC was 22 of 579 (3.8%), and type IV was 14 of 579 (2.4%). Note the blue circle indicates the position of the anterior papillary muscle.	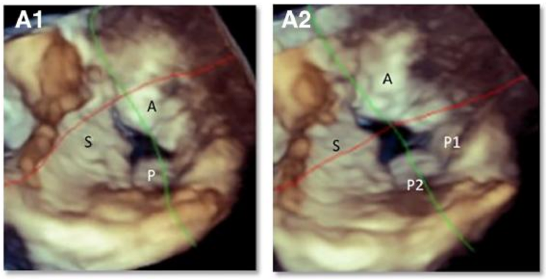 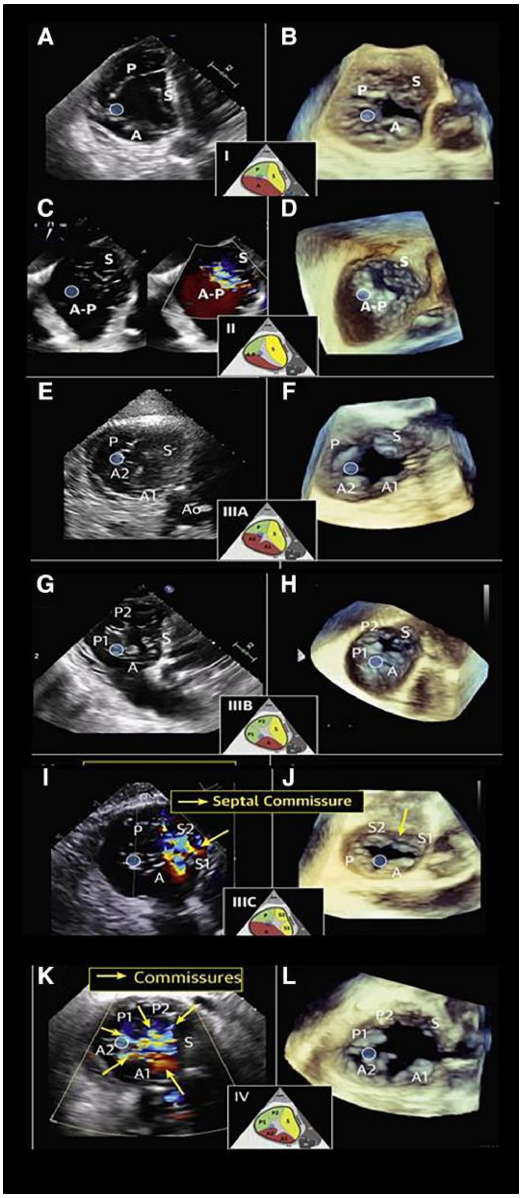

Continued

Table 19 Continued

Description	Image description	Images
The sub-valvular apparatus The PMs and chordae form the 'tensor apparatus' of the TV. There are three distinct PMs: anterior, inferior (or posterior), and septal PM.[50–53] The anterior PM (aPM) is the largest with chordae supporting the anterior and posterior leaflets. The inferior PM (iMP), often bifid or trifid, lends chordal support to the posterior and septal leaflets. Finally, the septal PM (sPM) is highly variable: being formed by multiple muscular/tendinous strands attached to the septal leaflet. Chordae may arise directly from the septum to the septal leaflet. Several thin muscular bars extend from the right ventricular wall to the ventricular aspect of the hinge line of leaflets in a crisscross fashion. These muscular bars, which look like the third-order chordae of MV, are believed to reinforce this segment of the annulus. The trabecula septomarginal, the moderator band, and the APM join together, forming a kind of U-shaped ridge that divides the RV inflow from the RV outflow tract.	**Images A and B** show the APM from trans-gastric view in 3D and in 2D TOE, respectively. **Images C and D** show the IPM from trans-gastric view in 3D and in 2D TOE, respectively. **Images E and F** show a longitudinally/obliquely cropped RV focusing on the trabecula septomarginal (TSM), moderator band (MB), and APM. These three structures join together forming a U-shaped ridge (red line) that divides the inflow to outflow of RV.	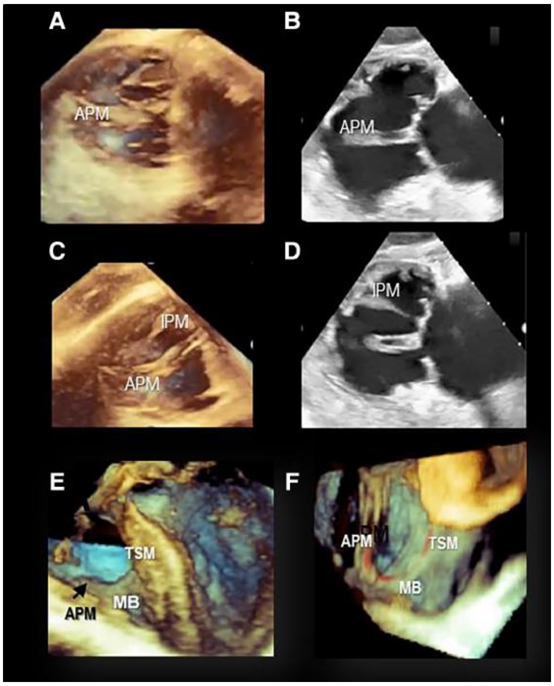

Acquisition and display modalities

There are many imaging planes for 3D TOE acquisition of the TV apparatus.[54–58] The quality of acquired images depends on body habitus (indeed, the long axis of the right heart could be respect to the coronary plane of the body, in horizontal, oblique or vertical position depending on the body habitus) and on right ventricle (RV) and right atrium (RA) size. Any 2D TOE cross-section (mid-oesophageal, deep oesophageal, or trans-gastric) in which leaflets are clearly seen could be used as 2D plane to acquire 3D TOE image. Once the entire TV is included in two orthogonal views, 3D TOE should be acquired in zoom modality and (when possible) using ECG-gating multi-beat acquisition. Tangential views and all the new display modalities (photorealistic and glass/transparency display) may help in defining anatomical details.

Four 3D TOE 'en face' views, all equally valuable and interchangeable, have been described:[56] the anatomical view, bi-caval view, trans-gastric view, and surgical view. Particularly useful during the tricuspid edge-to-edge clipping are the cross-section images inflow–outflow and the four-chamber views. Two anatomical land markers are important for identification of commissures between leaflets: the AO which is adjacent to the anteroseptal commissure and the coronary sinus (CS) which is very close to the posteroseptal commissure. *Table 20* shows the above-mentioned 3D TOE views and anatomical land markers.

Table 20

Image description	Image
Image A In the '**anatomical perspective**', the TV is usually acquired in four-chamber or in RV inflow–outflow view. The septal (S) leaflet (the easiest to be recognized being inserted of the atrioventricular septum) is located at nine o' clock. **Image B** In the '**bi-caval view**', the TV is shown with the septal leaflet located at 12 o'clock and the MV superiorly. **Images C and D** '**Trans-gastric views**' in systole and in diastole, respectively, and the septal leaflet located at 3 o'clock. Of note in trans-gastric view, the TV is seen from a ventricular perspective. **Image E** TV in the operating room ('surgical' view). The septal leaflet is located at 6 o' clock. **Image F** 3D TOE zoom modality from the atrial perspective rotated to show the same surgical view.	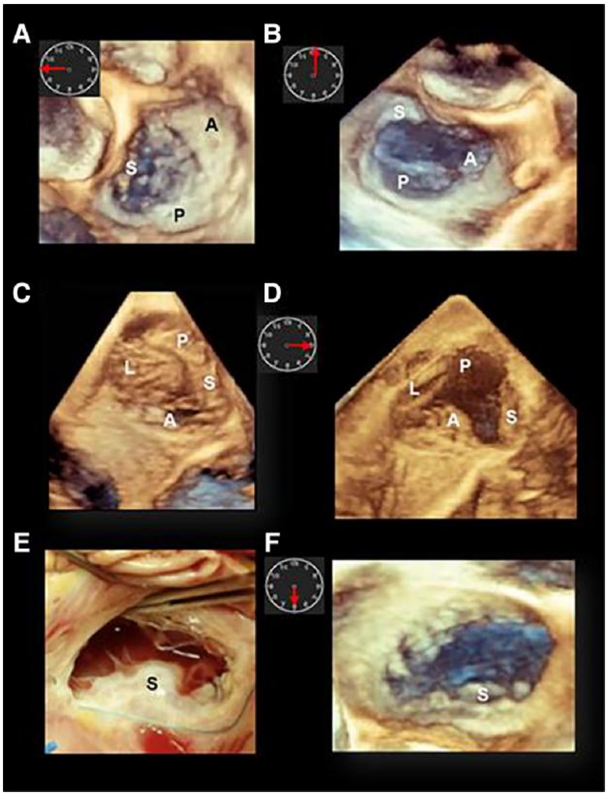
Image A 3D TOE inflow–outflow tract. **Image B** 3D TOE four-chamber view. RA, right atrium; RV, right ventricle.	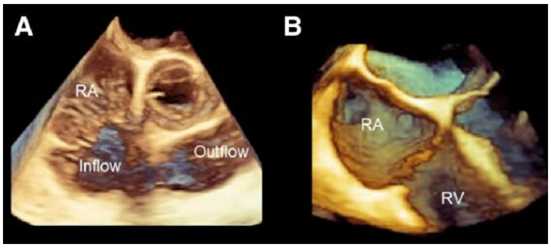
Image A Anatomic specimen showing the CS, as anatomic land marker for the posteroseptal commissure (asterisk), and the AO, not visible in the image, as anatomic land marker for anteroseptal commissure (asterisk). **Image B** The corresponding 3D TOE perspective.	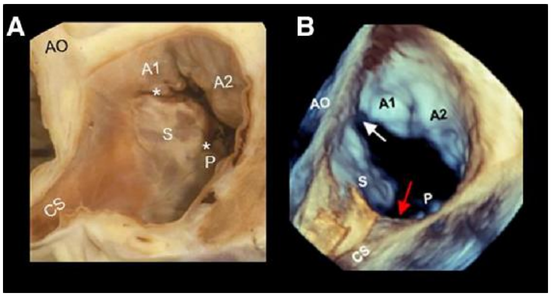

Key points

3D TOE imaging of the TV is challenging for the following because (i) it is far away from the transducer location, (ii) it is positioned obliquely to the direction of 3D pyramidal ultrasound beam, and (iii) leaflets of the TV are thin (∼ 1 mm).

Tricuspid annulus (TA) does not have a distinct fibrous ring that sustains the leaflets. It can be divided into a 'mural' component (which corresponds to the insertion of anterior and posterior leaflets on the free wall of the RV) and a 'septal' component (which corresponds to the hinge line of the septal leaflet).

Despite the name 'tricuspid', the assumption that the valve has three leaflets is not always true. The presence of accessory leaflets (up to six) is a very common finding.

There are three distinct PMs: the aPM is the largest and the most constant, the iMP is smaller than the anterior and often bifid or trifid, and the sPM is the most variable: being formed by multiple muscular/tendinous strands.

Any 2D TOE cross-section in which leaflets are clearly seen could be used as 2D plane to acquire 3D TOE image. A 3D TOE image should be acquired in zoom modality using ECG-gating multi-beat acquisition.

Four 3D TOE 'en face' views have been described: the anatomical view, bi-caval view, trans-gastric view, and surgical view. Particularly useful during the tricuspid edge-to-edge clipping are the cross-section images inflow–outflow and the four-chamber views. Two anatomical land markers are important for identification of commissures: the AO (adjacent to the anteroseptal commissure) and the CS (close to the posteroseptal commissure).

TV disease

Classification

Tricuspid stenosis

Obstruction of the native TV may be caused by the following four conditions: (i) rheumatic disease, (ii) congenital abnormalities, (iii) metabolic or enzymatic abnormalities, and (iv) active infective endocarditis.[59]

Tricuspid regurgitation

The aetiology of tricuspid regurgitation (TR) is generally divided into 'primary' (or organic due to leaflet pathology) and 'secondary' (or functional 'non-leaflet pathology).[60,61] Primary TR accounts for 7.4% of cases, whereas secondary TR accounts for 92% of cases. Newer classification systems define a third class of TR, related to a cardiac implantable electronic device (CIED).[62,63] This was formally an aetiology within the primary classification; however, the presence of an external device which may affect leaflets as well as sub-valvular apparatus justifies making this a separate category.

Primary TR

'Primary TR' results from structural abnormalities of valve apparatus, may be congenital or acquired in nature, and accounts for only 10–15% of all severe TR. The most common congenital cause of TR is the Ebstein anomaly characterized by an apical displacement of the leaflets which arise directly from the wall of the RV. Acquired causes of primary TR include endocarditis and tumoural masses, iatrogenic injury (such as RV endomyocardial biopsy), drug-induced leaflet damage (such as anorectic drugs, dopamine agonists, and ergot alkaloids), systemic diseases (such as lupus erythematosus and sarcoidosis), radiation, rheumatic disease, endocarditis, and trauma. *Table 21* shows some examples of primary TR and the corresponding 3D TOE images.

Table 21

Primary (organic) TR	Image
Carcinoid disease The characteristic pathological findings are endocardial plaques of fibrous tissue that very frequently involve the tricuspid and the PV, causing thickening and distortion of valve leaflet with consequent regurgitation, stenosis, or both. **Image A** shows a bi-commissural 2D TOE with thickened leaflets (red arrow) in patients with carcinoid disease. **Image B** shows the 3D TOE zoom modality 'en face view' from overhead of the same patients of image A. **Images C and D** show a 3D TOE 'en face view' zoom modality from overhead of a second patient with carcinoid disease. Markedly thickened (red arrows) and restricted leaflet closing and opening (white arrows) are clearly visible.	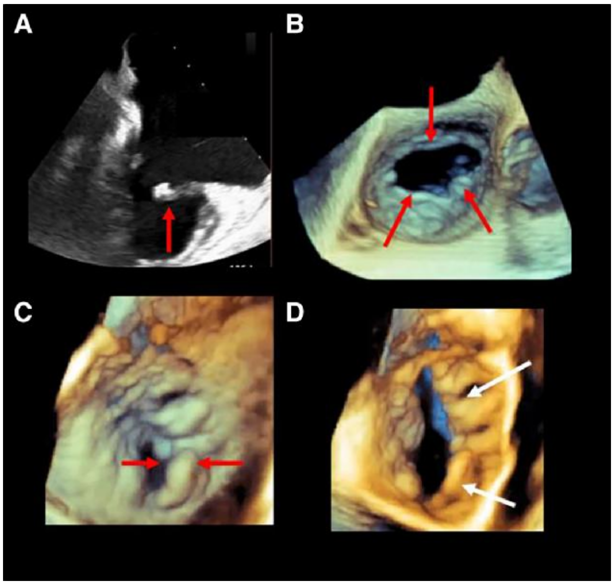
Primary TR due to IE is less frequent than left-side IE accounting for 5–10% of all IE cases. The major risks factors for IE on TV are intravenous drug abuse, intracardiac device, and central venous catheters. **Image A** Large endocarditis vegetation (red circle) in a patient with catheter (red arrow). **Image B** Endocarditis vegetation in drug abuser patient.	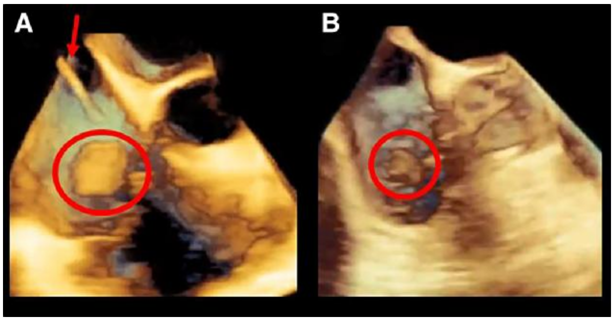
TV prolapse Normal TV is slightly redundant. Thus, due also to slightly non-planarity of TA, some degree of leaflet protrusion in RA in otherwise normally structured TV can be observed. An excessive protrusion into the RA, with redundancy of leaflet tissue and significant TR, is a typical finding of myxomatous TV disease. **Image A** 3D TOE of TV acquired in zoom modality from overhead. The asterisks point the prolapsing leaflet tissue. **Image B** 3D TOE of TV acquired in zoom modality and rotated to obtain a tangential view. The arrow points at prolapsing tissue protruding in RA.	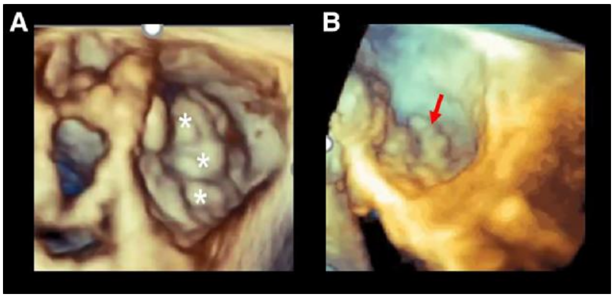

Continued

Table 21 **Continued**

Primary (organic) TR	Image
CIED CIED is one of the major causes of TR. Mechanisms that may cause TR are leaflet restriction/adhesions, leaflet perforation, and sub-valvular interference.[63] 3D TOE is an important tool for assessing these mechanisms due to its ability to visualize long segments of catheters. Leads located in commissural positions or in the centre of the valve were less likely to be associated with significant TR. Leads adhering or impinging on the leaflet are usually associated with greater degrees of TR. 'The motion of the lead is the key' in defining its role in TR. **Images A and B** 3D TOE acquired at mid-oesophageal level in diastole (A) and systole (B). The images show the catheter (Cat), positioned in one commissure. This position appears to not interfere with leaflet motion. The Cat, in fact, appears to be immobile during the cardiac cycle. In this case, no significant TR was noted. Of course, with 3D TOE, the trajectory of the Cat is clearly visualized. **Images C and D** 3D TOE from trans-gastric view in diastole (C) and in systole (D). The Cat is positioned on the commissure between septal and posterior leaflets (red arrow). The Cat does not move during the cardiac cycle. **Images E and F** 2D TOE trans-gastric longitudinal view showing the catheter (arrow) moving during the cardiac cycle, interfering with the motion of leaflets, and causing a severe regurgitation. **Images G–J** Four still frames of TOE mid-oesophageal acquisition focused on the RA and RV. The patient has three leads: two in the RA (asterisks) and one crossing the TV (Cat). Images clearly show as the Cat adheres to posterior/lateral leaflet (arrow) interfering with a normal leaflet coaptation.	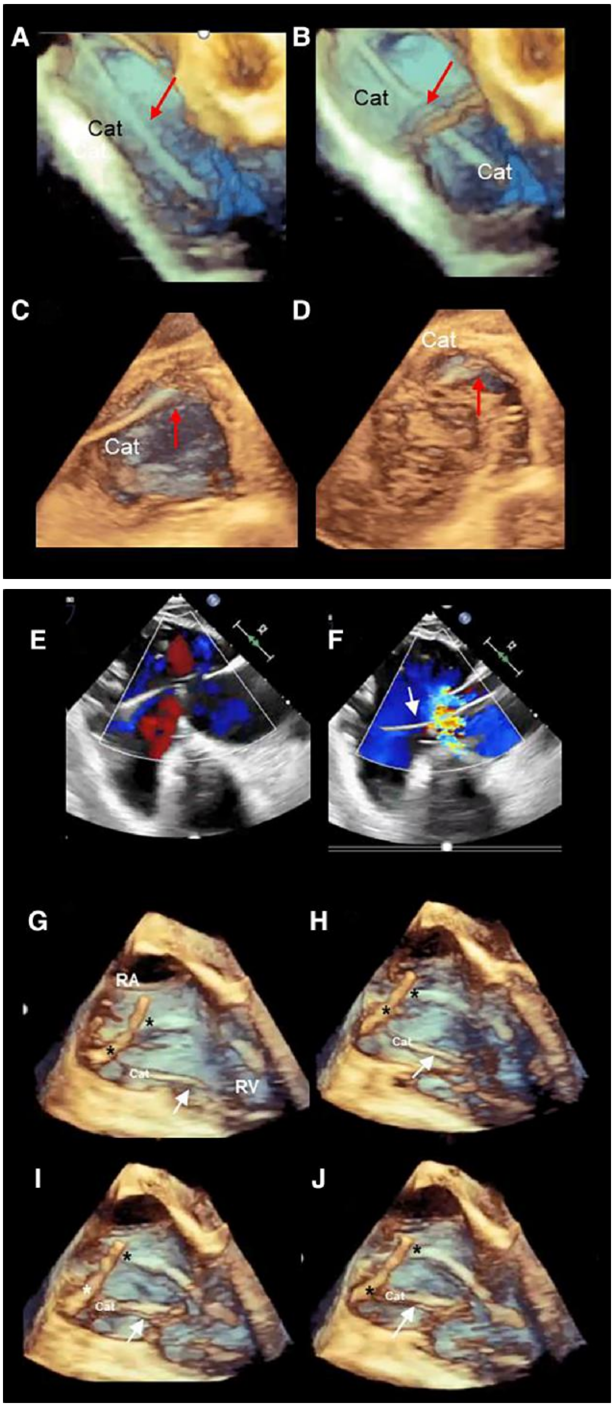

Secondary (functional) TR

Secondary (functional) TR is much more common than primary TR, and it is seen in 85–90% of patients with TR. The term secondary functional typically refers to TR which occurs as a consequence of geometric deformation of the tricuspid apparatus, in the absence of structural lesions of the valve.

Several disease processes can cause functional TR: left-side valvular disease of LV dysfunction, pulmonary hypertension (both pre- and postcapillary), primary RV dysfunction (due to RV myocardial disease or RV myocardial infarction), and isolated atrial dilatation of dysfunction (mainly due to AF). Despite the numerous aetiologies, two main mechanisms can be identified: the 'ventriculogenic' (or ventricular functional TR) and the atriogenic (or atrial functional TR) mechanisms.[64,65]

- The 'ventriculogenic' mechanism mirrors that of the symmetric patterns of functional MR. The increase in right ventricular volume and changes in shape (more spherical) disrupt the normal spatial relationships between leaflets, chordae, and PMs leading to leaflet tethering, dilatation and flattening of the TA, tenting, and apical leaflet coaptation.
- The atriogenic mechanism consists of an abnormal increase in the right atrial (RA) volume and tricuspid annular dilation, due to AF, leading to leaflet malcoaptation at the level of the annulus.

3D TOE is an important tool for an accurate assessment of mechanisms of TR, severity of TR, and more detailed evaluation of the extent of right-heart remodelling.

Although the pre-procedural planning of transcutaneous TV repair is based on a multimodality approach, 3D TOE plays an important role in (i) analysing TV morphology (number of leaflets, annular dilations, interference of catheter with leaflet motion, leaflet gap and 3D VCA, subvalvular apparatus, etc.), (ii) defining the degree and aetiology of TR, and (iii) analysing anatomic relationships amongst TV apparatus and surrounding structures. Since 3D TOE enables visualizing the TA 'en face' perspective, a countless number of diameters, circumference, and area can be measured. These parameters are relevant either before or after the procedure. However, systematic and consistent data that support the superiority of 3D TOE vs. the simple indexed tricuspid annular diameter are not still available.

Table 22 shows the different morphologies of secondary TR and the corresponding 3D TOE and schemes.

Table 22

Image description	Image
Ventricular functional TR **Image A** TV acquired in *x*-plane 2D TOE in short- (left-side picture) and in long-axis cross-section (right side picture). The image shows a ventricular dilatation, particularly of the mid and apical regions resulting in a more spherical ventricle (red dotted line) and tethering of the tricuspid leaflets. The blue and green lines are superimposed to posterior (P) and anterior (A) leaflets. The leaflets close apically to the annular plane (green dotted doubled-head arrow) forming a tenting. **Image B** shows the displacement of the PMs (red arrows). **Atrial functional TR** **Images C and D** show the RV is less dilated and the conical shape is maintained (red dotted line). Leaflet tethering is less prominent; however, there is marked dilatation of the TA and RA.	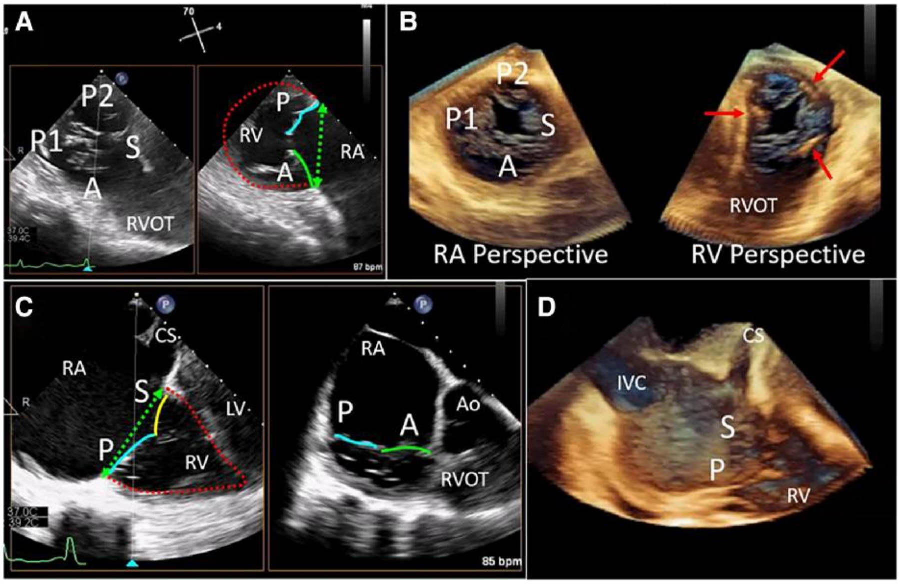

Continued

Table 22 Continued

Image description	Image
Differences between atriogenic and ventriculogenic functional TR.[66] The figure shows shape, size, and leaflet position of three annular shapes compared with normal TV (with permission from Utsunomiya H, Harada Y, Susawa H et al. European heart journal cardiovascular imaging 2020;21:1068–1078). **Normal TV geometry** **AF and severe TR** The annulus is dilated. However, there is no tenting, and RV has a normal size and shape. **Torrential atriogenic TR** Progressive RA and/or RV remodelling and dysfunction due to chronic volume overload result in further TA dilation, PM displacement, and leaflet tethering. The morphology of torrential atrial functional TR becomes similar to that of ventricular functional (VF) TR with sinus rhythm.	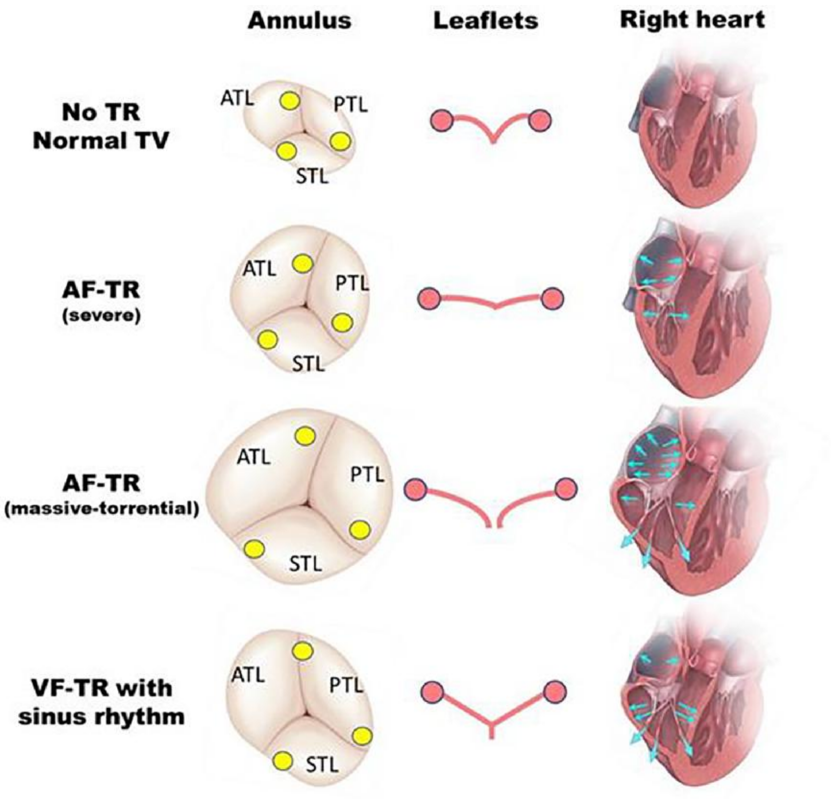

TR severity quantification tools

Echocardiography is the most widely used methodology to assess TR severity.[67–71] A multi-parametric and hierarchical approach to TR assessment has been suggested over the years (mild, moderate, and severe). However, given the complex, variable nature of the TV leaflets, the regurgitant orifice is often irregular, frequently with multiple leaks, and the coaptation zone non-planar. In addition, regurgitant jets are driven by low pressure and do not generate the same momentum as on the left heart, being very sensitive to changes in preload and cycle length. These combined anatomic and haemodynamic variables limit the utility of many echocardiographic parameters, in particular those utilizing colour Doppler and/or single measurements of a time frame. Finally, as in mitral regurgitation, the lack of a true comparator 'gold standard' is the major limitation to any attempt to quantify TR.

Table 23 describes three new quantitative measures utilizing 3D TOE echocardiography which have been recently explored.

Table 23

<table>
<tr><th>Description</th><th>Image</th></tr>
<tr><td>

VCA

3D TOE VCA is a rapid and reproducible method with an incremental value for quantification of particularly severe regurgitant lesions. This method is a 'surrogate' of regurgitant anatomic orifice and has been correlated with the multi-parametric assessment of TR using TTE. However, it must be said that it is sensitive to technical factors and demonstrates intervendor variability.[67] Outcomes studies using 3D VCA may clarify the appropriate cut-off for grading the severity of regurgitation.

Image A shows an example of the use of 3D colour Doppler to planimeter the VCA.

</td><td>

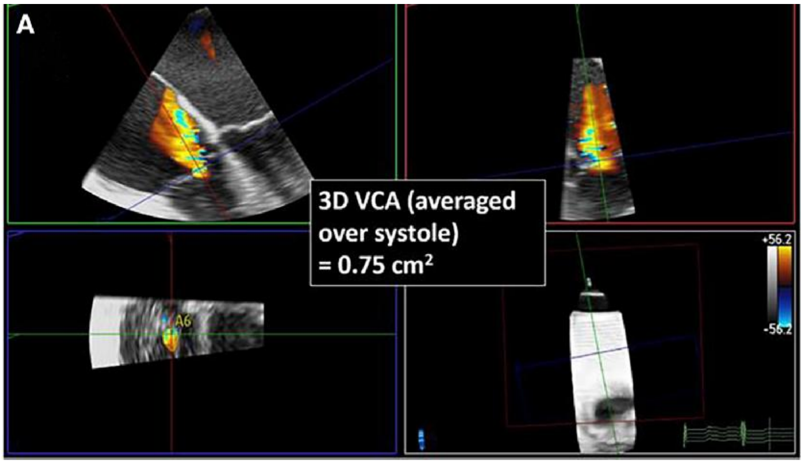

</td></tr>
<tr><td>

Volumetric method using 3D TOE annular area

This method can permit a more accurate quantitation of diastolic stroke volume (3D TOE tricuspid annular area is 19% smaller compared with semiautomated measurement by CT). 3D annular area multiplied by the annular pulsed wave velocity time integral results in the total diastolic stroke volume. Subtracting the forward stroke volume (from either the left or right ventricular outflow tract) yields the regurgitant volume.

Image B shows an example of this method.

</td><td>

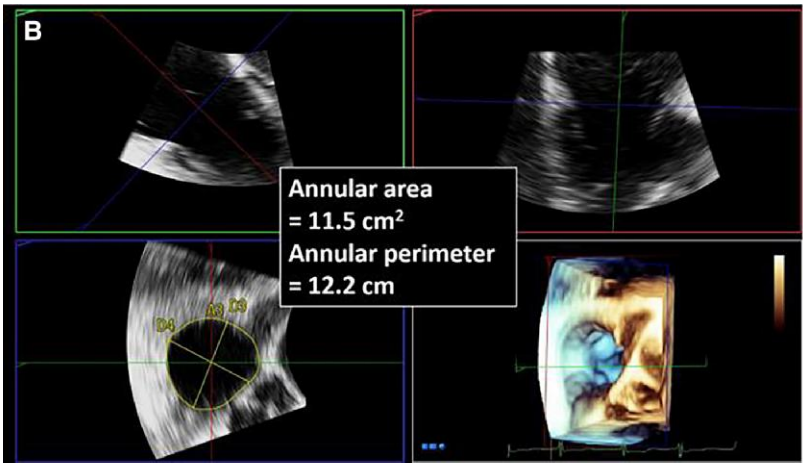

</td></tr>
<tr><td>

3D single-beat PISA[72]

Using a software specifically developed for 3D PISA determination, 3D TOE PISA–derived EROA correlated well with 3D VCA planimetry ($r = 0.97$, $P < 0.001$) and quantitative Doppler echocardiography ($r = 0.97$, $P < 0.001$). This method appears feasible in the clinical setting and more accurate than the conventional 2D PISA method for assessment of TR severity. However, it has not been extensively validated.

Image C shows an example of this method.

</td><td>

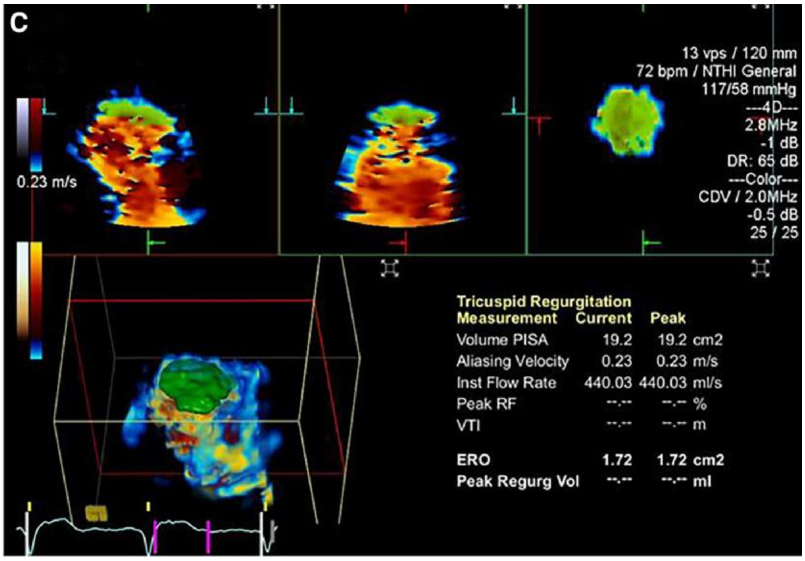

13 vps / 120 mm
72 bpm / NTHI General
117/58 mmHg
---4D---
2.8MHz
-1 dB
DR: 65 dB
---Color---
CDV / 2.0MHz
-0.5 dB
25 / 25

Tricuspid Regurgitation

Measurement	Current	Peak
Volume PISA	19.2	19.2 cm2
Aliasing Velocity	0.23	0.23 m/s
Inst Flow Rate	440.03	440.03 ml/s
Peak RF	--.--	--.-- %
VTI	--.--	--.-- m
ERO	1.72	1.72 cm2
Peak Regurg Vol	--.--	--.-- ml

</td></tr>
</table>

Post-surgery and transcatheter assessment

Assessment of TV function following surgical or transcatheter repair or replacement relies heavily on 2D echocardiographic imaging. 3D TOE may provide additional diagnostic information regarding mechanisms of dysfunction, including visualization of vegetations, pannus, thrombi, degenerative changes, and/or immobile leaflets. However, given the imaging limitations (i.e. far field imaging and off-axis imaging) and lower line density and frame rates of 3D image processing, the assessment of TV prosthetic morphology may be particularly limited.

Section II

Prosthetic valves

Introduction

Prosthetic heart valves (PHVs) can be classified into three broad categories: (i) mechanical (bileaflet, tilting disc, and ball-and-cage), (ii) surgical biological (stented, unstented, and homograft), and (iii) transcatheter bioprosthetic valves. Some of them are no longer implanted and will not be discussed here. The haemodynamic performances of the most recent and commonly used PHVs are very close to that of native valve with low resistance to the forward flow and trivial regurgitant backflow.

PHV dysfunction is potentially a life-threatening complication. Thrombus/pannus obstruction/regurgitation, paravalvular leak (PVL), bioprosthetic structural valve degeneration, and endocarditis are the main PHV dysfunctions.[73]

2D TTE/ TOE, Doppler, and colour Doppler examination are the first steps in the assessment of PHVs, and, importantly, these techniques can be performed in any clinical scenarios and in every setting including emergency departments and operating rooms. Currently, in some specific clinical scenario, fluoroscopy, CT scan, cardiac magnetic resonance, and FDG-PET/CT are also used as complementary tools for the diagnosis and management of PHV complications.[73,74]

3D TOE plays a major role in PHV dysfunction. In particular for mitral PHVs, the ‘realistic’ images of 3D TOE add incremental value analogous to imaging of native MV. The most valuable images of mitral prostheses are acquired from atrial perspectives. From this view, the atrial side of mechanical PHVs is clearly seen without shadowing and reverberations produced by the metallic parts which are projected on the ventricular side (just opposite to what occurs with TTE). Rings used in the surgical annuloplasty can also be readily appreciated by 3D TOE.[75]

In this section, we explore the role of 3D TOE in mitral and aortic prosthesis and in mitral prosthetic rings.

Mitral prosthetic valve

Two main types of mitral PHVs are currently used for surgical procedures: the stented biological and the bileaflet mechanical. A comprehensive understanding of normal PHV morphology and occluder mechanisms is an essential pre-requisite to identify pathological states. 3D TOE normal aspects and dynamics of stented biological and the bileaflet mechanical PHVs are illustrated in *Table 24*.

Table 24

Image description	Image
Stented biological PHVs The stented biological PHVs consist of three leaflets mounted on circular annular ring with three struts extending into the inflow portions of the LV. For mitral PHV, the best acquisition modality is the zoom multi-beat ECG-gating acquisition, which allows acquiring images with volume rate up to 90–100 Hz without colour and up to 25–30 Hz with colour Doppler. Using the zoom modality single-beat, the volume rate decreases up to 25 Hz without colour Doppler and up to 15 Hz with colour Doppler, greatly depending on volume size. **Images A and B** Biological PHV from the atrial perspective in diastole (image A) and in systole (image B). The asterisks mark the three leaflets. **Images C and D** The same valve seen from the ventricular perspective in diastole (image C) and in systole (image D). The asterisks mark the three struts. Of note, biological tissue does not produce shadowing or artefacts. **Images E and F** 3D TOE colour Doppler in diastole (image E) and in systole (image F). In stented biological prostheses, trivial or mild central regurgitant jet can be seldom seen (arrow in image F).	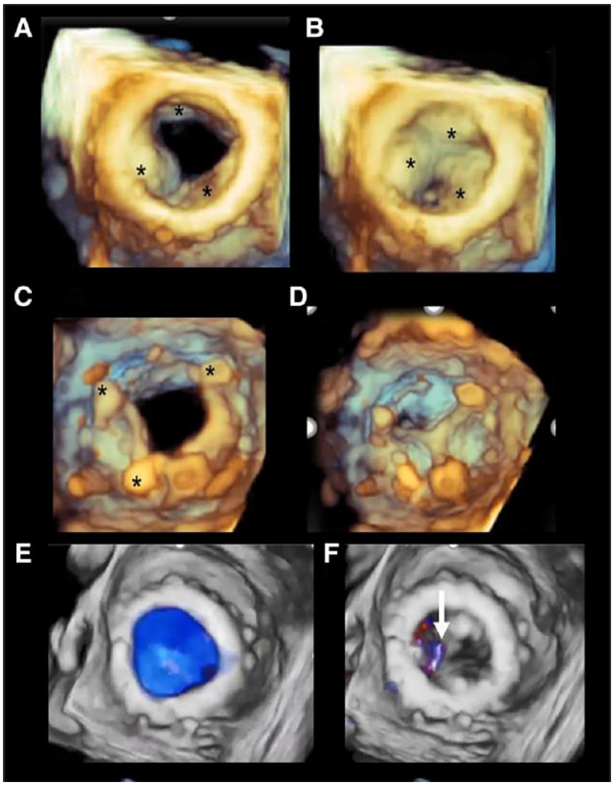

Continued

Table 24 **Continued**

Image description	Image
Bileaflet mechanical PHVs These mechanical PHVs consist of two semilunar disc occluder attached to a rigid valve ring by two small hinges. The opening angle of the occluder relative to the annulus plane ranges from 75° to 90° with a smaller, slit-like central orifice and two larger semi-circular orifices. As for stented biological, the zoom modality multi-beat ECG-gating acquisition is the best acquisition modality. **Images A and B** 3D TOE images from the atrial perspective in diastole (image A) and in systole (image B). The arrows show the direction of the diastolic flow through the slit-like central orifice (small arrow) and the semi-circular orifices (curved arrows). The two hinge pivots can be positioned parallel to the line connecting the two native commissures (anatomic orientation) or perpendicular to it (anti-anatomical orientation). How orientation is associated with the better intracardiac flow dynamic is unclear. In this example, the spatial orientation is anti-anatomical. Notably, the metallic components such as the hinges are thicker than they actually are, being subjected to blooming artefacts (image B red circle). **Images C and D** 3D TOE images from a tangential view in diastole (image A) and in systole (image B). The asterisk points at one disc seen 'en face'. **Images E and F** Bileaflet mechanical valve seen in cross-section (longitudinal view) in diastole (image E) and in systole (image F). The arrows mark the huge reverberations projected in the LV by a metallic structure. **Images G and H** Photorealistic image of bileaflet mechanical valve in diastole (image G) and in systole (image H). The arrow in image H points at stiches that appear thicker than they actually are (blurring artefacts).	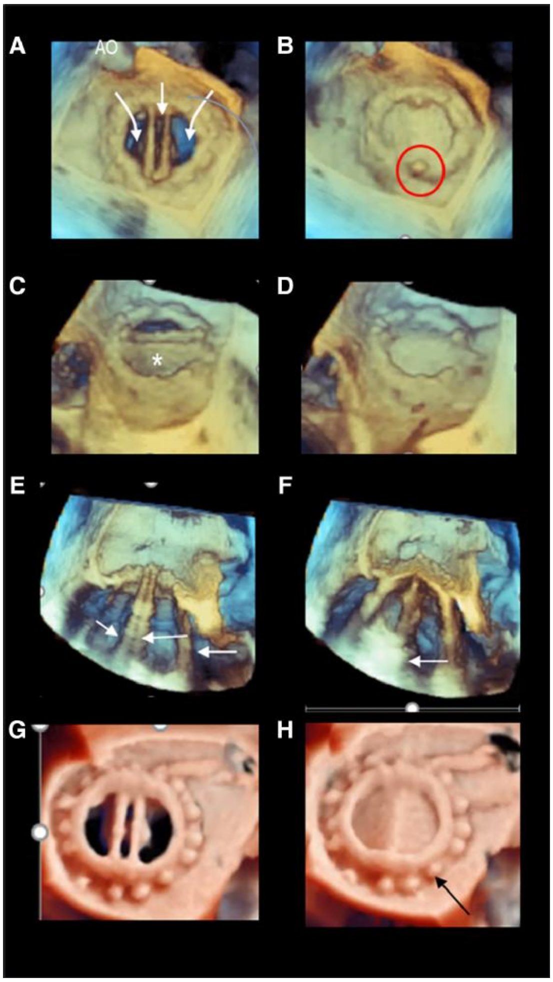
Normal 3D TOE colour Doppler[76] Mechanical bileaflet prostheses have a 'leakage backflow'. This 'built-in' regurgitation prevents blood stasis and thrombus formation using a washing effect. The normal leakage backflow jets extend around the space between the discs and the ring and are short in duration and narrow. **Images A and B** 3D TOE colour Doppler from an atrial perspective in diastole (image A) and in systole (image B). In systole, the leakage backflow jets are clearly visible all around the hemi-disc (arrows). **Images C and D** Same case in tangential perspective in diastole (A) and in systole (B). The systolic image shows these jets are small and narrow, extending into the LA only for few millimetres.	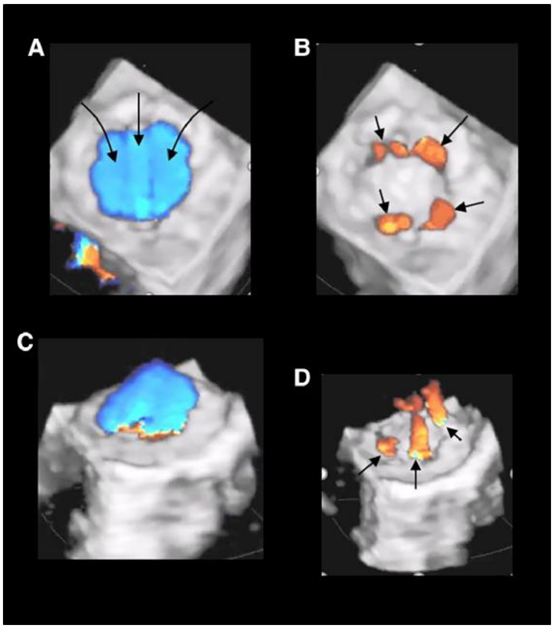

Prosthetic MV obstruction/regurgitation

Valve thrombosis and pannus ingrowth account for the vast majority of non-infectious causes of prosthetic valve dysfunction.[77–79]

'Thrombosis' is more likely to occur early after PV implantation in a setting of inadequate anticoagulation, and it is more common with mechanical prostheses. The interference of thrombus with the occluders may cause various degrees of obstruction/regurgitation and embolic phenomena.

Unlike thrombosis, pannus is more likely to occur long after valve replacement, independently from anticoagulation level and may cause a variable degree of obstruction and regurgitation.

2D TTE, TOE Doppler, and colour Doppler are essential for the diagnosis of mitral PV obstruction and should be advised as first line. 3D TOE allows a full vision of the entire atrial surface of the prosthesis and surrounding structures detecting the presence, extension, and localization of any mass attached. In biological PV degeneration, the 'en face' views from atrial and ventricular perspectives provide a 'panoramic' view of the degenerate valve leaflet.[73]

Table 25 shows examples of 3D TOE of mitral PV obstruction.

Table 25

Image description	Image
Mechanical prosthetic obstruction **Images A and B** 3D TOE bileaflet PVs from the atrial perspective in diastole (image A) and in systole (image B) showing in systole only one disc closes properly, causing both obstruction and regurgitation (image with permission of Manuela Muratori J. Cardiovasc. Dev. Dis. 2021). **Images C and D** 3D TOE bileaflet PVs from the atrial perspective in diastole (image A) and in systole (image B). The diastolic still frame shows two small masses close to one hinge of the prosthesis (arrows). In systole, one of the discs does not close properly. **Images E and F** 3D TOE bileaflet PVs from the atrial perspective in diastole (image A) and in systole (image B). In diastole, two small thrombi are seen on the two hinges (arrows). In systole, the thrombosis affects the entire contour of the valve (arrows).	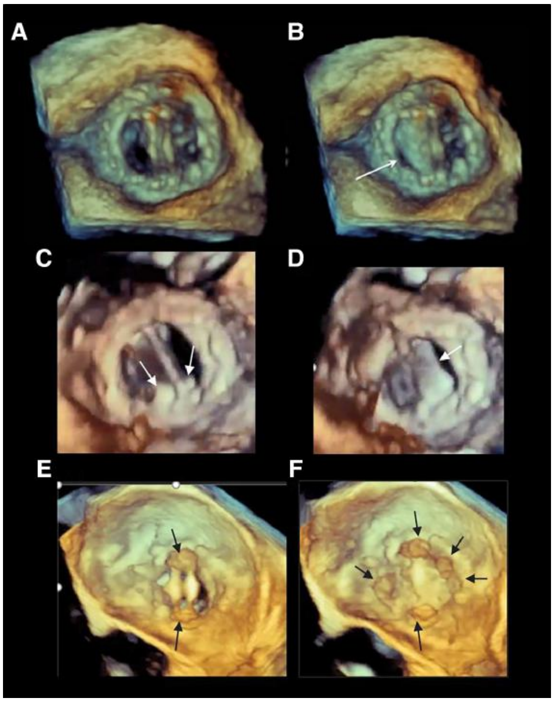
Biological prosthetic obstruction **Image A** 3D TOE from the atrial perspective in systole (A). The valve is severely degenerated, and the three leaflets are no longer recognizable. The asterisk marks the stenotic orifice. **Image B** The corresponding surgical specimen. **Images C and D** Same case seen with the photorealistic modality with the source of light positioned behind the valve in diastole (image A) and in systole (image B). The asterisk in image B marks the stenotic orifice.	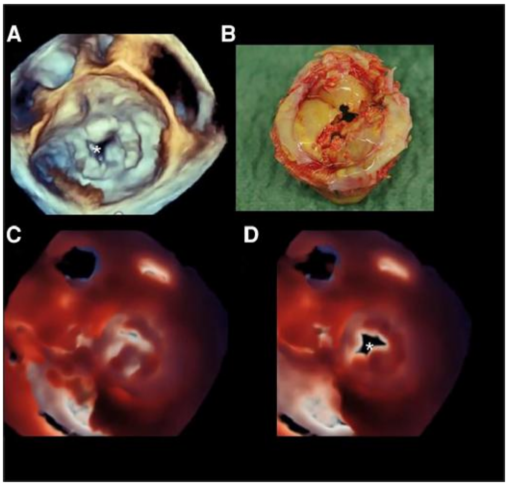

Continued

Table 25 **Continued**

Image description	Image
Biological PV endocarditis **Images A and B** 3D TOE from a lateral perspective. Two systolic still frames showing multiple high-mobile endocarditis masses (arrows). The lateral perspective allows a better perception of the extension of the masses into the LA. **Images C and D** Same case of images A and B after having cropped the 3D data set longitudinally. The longitudinal cross-section is seen in systole (image C) and in diastole (image D). The images show the systolic and diastolic excursion of the masses (white arrows). The blue light arrows show the masses originate from the sewing ring.	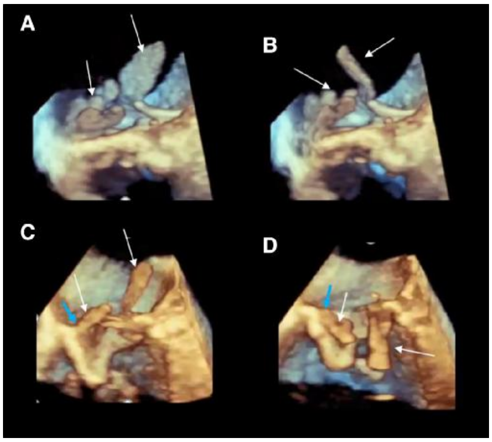

Prosthetic mitral PVL and annuloplasty ring dehiscence

PVL is due to incomplete seal between the implanted PV sewing ring and native annulus. Calcification of intrinsic friability of the annulus may preclude an adequate suturing. Not rarely, the PVL is precipitated by an infective endocarditis. The most common symptoms suggestive of PVL are heart failure (due to severe regurgitation trough a large PVL) and haemolytic anaemia (due to red cell destruction through a narrow and serpiginous channel). In 'annuloplasty-based MV repair', suture leak causes separation between the prosthetic ring from the underlying native annulus.

Although 2D TTE remains the first diagnostic step, not rarely shadowing and reverberations of the non-biological material of the PV cover the atrial side of the prosthesis and the regurgitant jets. Thus, 2D TOE is essential in the evaluation of patients with suspected PVL.

3D TOE is the 'ideal' technique for the evaluation of the PVL, allowing an accurate determination of the anatomic characteristics, i.e. the number, site, size, and shape (circular, linear, crescent, or irregular).[80] The severity of regurgitation with 3D TOE can be assessed with the same criteria used to define the severity of native MV. As in mitral regurgitation, 3D vena contracta (VC) is the easiest method.

Table 26 shows some 3D TOE examples of mitral PVLs and annuloplasty ring dehiscence.

Table 26

Image description	Image
Mitral prosthetic PVL The 3D TOE images should be displayed in the surgical view, with the aortic valve at the top (12 o'clock) and the left appendage at approximately the 9 o'clock position. Once the PVL/s are detected, other views may confirm the diagnosis. The best acquisition modality is the zoom modality multi-beat ECG-gating. In case of AF, zoom modality single-beat is also useful provided that the pyramidal data set includes only the prosthetic valve and immediate surrounding structures. **Images A and B** 3D TOE from the atrial oblique perspective (image A) and in tangential view (image B) showing two leaks (curved arrows). **Images C and D** 3F TOE from the atrial perspective showing a circular PVL (image C, curved arrow) and linear/crescent PVL (image D, arrows). **Images E and F** 3D TOE from the atrial perspective in volume rendering (image E) and using the free source of light (image F) showing a large crescent PVL (arrows). **Images G and H** Large PVL (asterisks) from the atrial (image G) and ventricular perspective (image H).	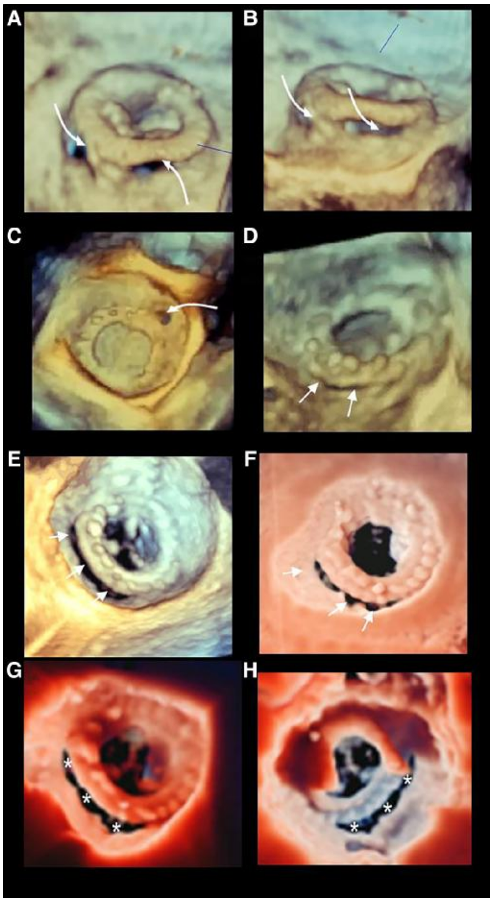
3D TOE colour Doppler PVL may not be identified by the 3D TOE imaging alone particularly when it is located in very close proximity to the ring. In such a case, colour Doppler is essential. Indeed, it is important to integrate 3D structural information with 3D colour Doppler, as dropout artefacts close to the prosthesis can be mistaken for a gap. **Image A** 3D TOE from the atrial perspective of a mechanical PVL. The arrows mark the two leaks. **Image B** Same case with colour Doppler (arrows). **Image C** 3D TOE from the atrial perspective. The white arrow marks a percutaneous implanted plug (image C arrow). However, the 3D TOE images do not identify a PVL. **Image D** Same case. 3D TOE colour Doppler identifies a large regurgitant jet (black arrows).	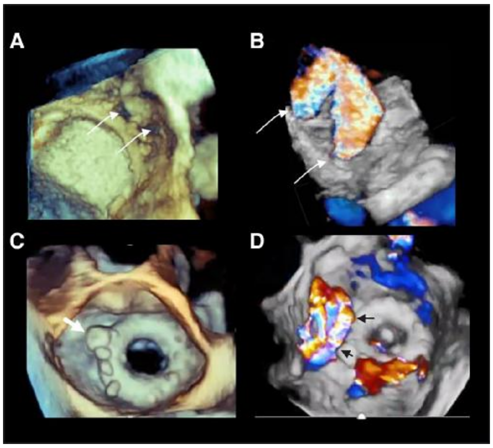

Continued

Table 26 Continued

Image description	Image
Severity of regurgitation **Image A** Long-axis view showing the long-axis cross-section (red line) and the perpendicular short-axis cross-section of the PV regurgitant jet to obtain the VC. **Image B** A cross-section planimetry of the VC (dotted line).	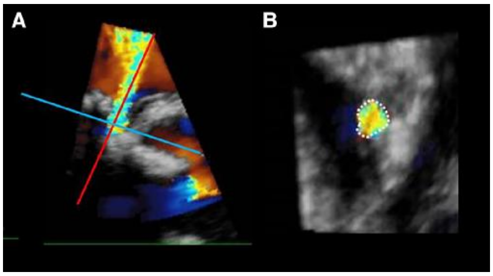
Annuloplasty ring dehiscence[81] The annuloplasty ring dehiscence usually does not disrupt the attachment between the native leaflets and native annulus. This pathomorphological peculiarity has two consequences: (i) ring dehiscence is not amenable for percutaneous leak closure; (ii) the underlying leaflet may close in systole the leak preventing regurgitation. An aggressive annular downsizing may expose the annulus-ring system to greater stress, with abnormal annular stress distribution and consequent dehiscence. **Images A and B** 3D TOE in diastole (image A) and in systole (image B) showing an extensive ring dehiscence in diastole (asterisks) which is covered by leaflet tissue in systole (red arrow). **Images C and D** Same case of images A and B. 3D TOE cropped in longitudinal view, showing the ring dehiscence in diastole (red curved arrow), while in systole, the leaflet tissue (red circle) closes the leak. **Images E and F** Same case of images A and B. 3D TOE colour Doppler shows as in diastole (image E) a laminar flow (red arrow) crossing the dehiscence, while in systole, the leaflet tissue prevents regurgitant flow (white arrow).	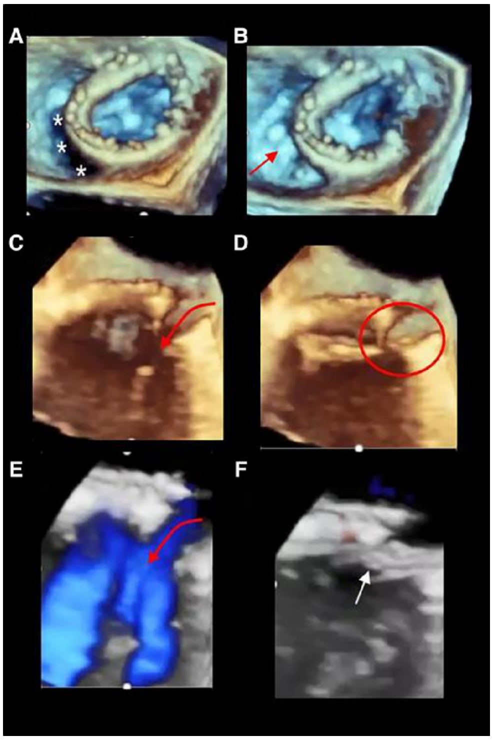

Prosthetic aortic valve obstruction/regurgitation[82]

3D TOE assessment of aortic protheses is more challenging than mitral prostheses for the following three reasons: (i) aortic PVs are usually smaller, and anterior components of the prosthesis are in the far field during 3D TOE examination, (ii) the position of the aortic valve is oblique with respect to the angle of incidence of the pyramidal data set, and (iii) reverberation artefacts and acoustic shadowing by prosthetic material cause a degradation in 3D TOE echocardiographic images. Thus, in general, visualization of 3D TOE aortic PVs is poorer than that of mitral PVs. Nonetheless, sewing rings, disc occluders, and bioprosthetic leaflets can be readily seen in 'en face' perspective and, more importantly, in a single acoustic window, without probe manipulations. Thus, 3D TOE can help in detecting PV thrombosis and pannus and PVL, complementing the role of 2D TOE.

Table 27 shows some 3D TOE examples of aortic PV dysfunction.

Table 27

Image description	Image
'**PV thrombosis and pannus ingrowth**' account for the vast majority of non-infective causes of aortic prosthetic valve dysfunctions. In particular, pannus is more common with aortic than with mitral prostheses. Pannus originates from the sewing ring and may extent to the orifice, hinge of mechanical valve, or leaflets, causing restriction of leaflet mobility and narrowing of the outflow tract orifice. **Image A** shows a pannus ingrowth (arrows) arising from the sewing ring and extending to the orifice. **Image B** shows the corresponding anatomic specimen. **Image C** 3D TOE images from aortic perspective showing a PVL (arrow). PVL is due to poor tissue quality of the native annulus due to friability and calcification. **Image D** Same case with colour Doppler. **PVLs in TAVI** The main mechanisms of PVLs in TAVI include undersizing of the implanted valve and asymmetric calcifications in the landing zone that preclude complete stent expansion. **Images E and F** show two different 3D TOE perspectives showing a PVL in TAVI (arrows). **Images G and H** PVL before (image G arrow) and after (image H) percutaneous closure (arrow).	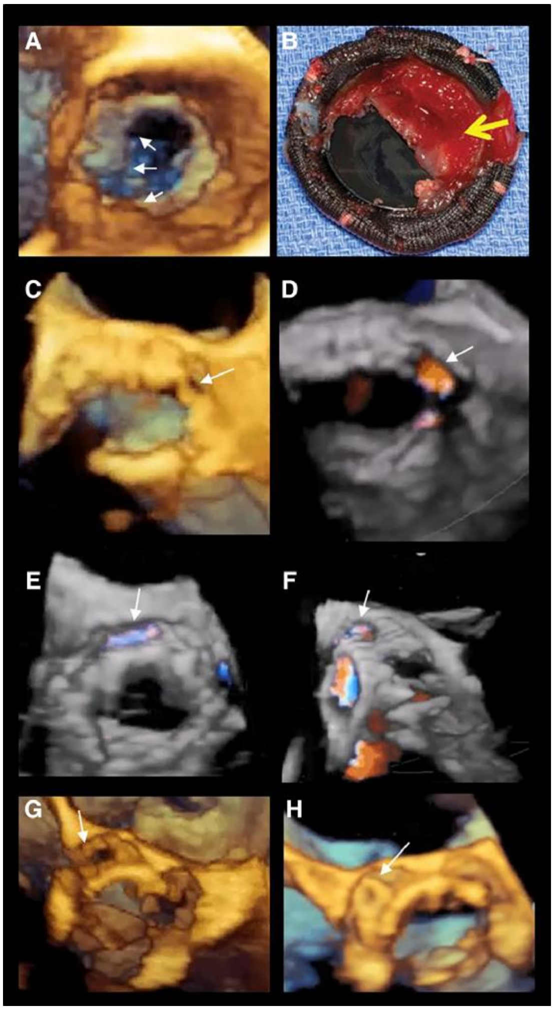

Section II

Intracardiac cardiac masses and infective endocarditis

Introduction

The term 'cardiac masses' refers to a heterogeneous group of abnormal structures within or adjacent to the heart. Primary cardiac tumours (benign and malign), metastasis from extra-cardiac tumours, and 'non-tumoural masses', such as intracardiac thrombi and vegetations, are the most common types of cardiac masses.

Superiority of 2D TOE over 2D TTE for the detection of cardiac masses has been shown convincingly and has been one of the driving forces for the adoption of 2D TOE as an essential diagnostic tool in clinical practice.[83] This is also true for the detection of small vegetations and abscess formation, especially in the context of prosthetic valves.[82]

However, using 2D TOE, it may be difficult to reconstruct tridimensional masses having an irregular shape even when multiple planes are used: fringes of the mass, in fact, may appear and disappear through the echocardiographic plane. Not surprisingly, the size of an irregular-shaped mass may be underestimated when using 2D TOE.[84]

Conversely, 3D TOE shows the following advantages over 2D TOE:

(a) Allows a panoramic and comprehensive views of the masses, accurately assessing size and extent
(b) Provides a more accurate assessment of the anatomical relationships to adjacent structures
(c) By rotating and/or properly cropping the volumetric data set allows obtaining unusual perspectives which may further enhance the diagnostic accuracy

However, whether this superiority translates into clinically meaningful incremental information is less clear and not yet rigorously proven. In this section, we describe some types of masses where 3D TOE has convincingly shown, for its intrinsic characteristic, the highest accuracy.

Table 28 shows examples of the most frequent intracardiac tumours, infective endocarditis, and aortic atheroma.

Table 28

Intracardiac tumoural masses		
Cardiac myxoma[85–88]	**Image description**	**Images**
Cardiac myxomas usually take origin from the atrial wall. A total pf 75% of myxomas develop in the LA (mainly around the FO), 18% develop in the RA, and 6% in both left and right ventricles. The myxoma may be either pedunculated or sessile. The myxoma may contain cysts or areas of necrosis of haemorrhage.	**Image A** 2D TEE showing a spherical sessile myxoma (M) arising at the junction between FO and SS. **Image B** The corresponding 3D TOE. **Image C** Sessile myxoma (M) attached to the lateral wall of the LAA. **Image D** The corresponding 3D TOE image.	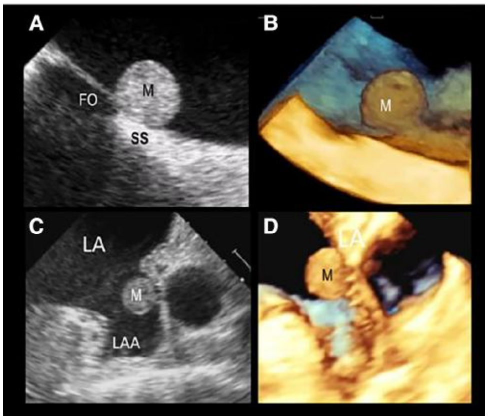
Macroscopically, '**two distinct types**' of myxoma can be distinguished. The most frequent has a rather compact structure (round or ovoid) with a smooth or lobulated surface. This type of myxoma adjacent to the mitral orifice may cause intermittent obstruction. The second type has an irregular aspect with fines villous excrescences. This type of myxoma may cause MV obstruction or, more frequently, peripheral embolism.	**Image A** 2D TOE appearance of compact ovoidal-shaped myxoma (M) with smooth surface. **Image B** The corresponding 3D TOE image. **Image C** 2D TOE appearance of a myxoma with multiple fines villous excrescences. **Image D** The corresponding 3D TOE image.	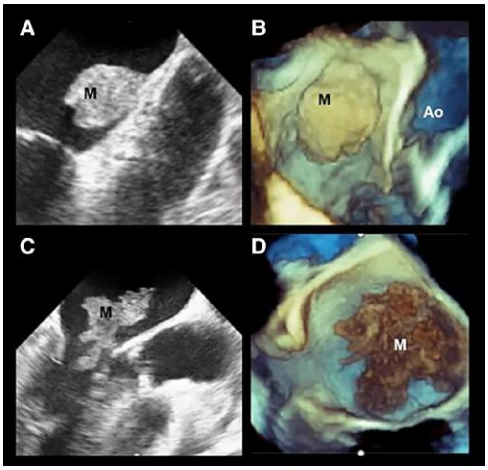
Papillary fibroelastoma[89]	**Image description**	**Image**
Papillary fibroelastoma (PFE) is one of the most common cardiac tumours with a predilection for being attached to the valvular endocardium. Histologically, it is a fibrous nodule covered by an endothelial layer in continuity with that of underlying leaflet. Usually, PFE is asymptomatic and discovered incidentally in a routine echocardiographic examination. More rarely, it may cause systemic embolism or acute coronary syndromes due to transient occlusion of the coronary ostia.	**Images A and B** 3D TOE cropped image of the AO in long-axis view. **Image B** Magnified image of the structures inside the red square of image A. The image shows a papillary fibroelastoma (arrows). **Image C** Same case. 3D TOE image of the AO in short-axis view. **Image D** Magnified image of the structures inside the red square of image A. The image shows that the papillary fibroelastoma is attached to the left coronary leaflet (arrows).	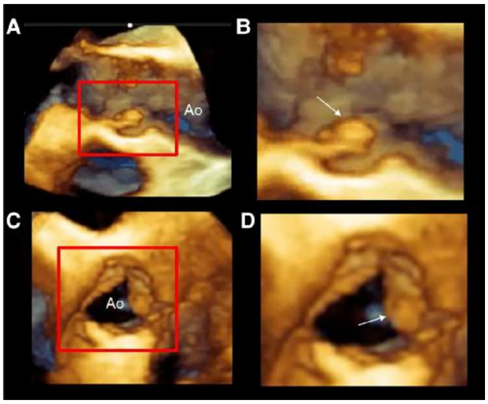

Continued

Table 28 Continued

Intracardiac tumoural masses		
Infective endocarditis (IE)[90,91]	**Image description**	**Image**
Vegetations are the hallmark of IE. They are formed by a colony of bacteria within a meshwork of fibrin, platelets, and inflammatory cells. Although endocardial lesions are often the 'primum movens', particular virulent bacteria may directly infect healthy endothelium leaflet. The vegetations are usually attached to the upstream side of valve leaflets. The size and mobility of vegetation matter. Large and highly mobile vegetations are strong predictors of peripheral embolic events.	**Images A and B** 'Oscillating' high-mobile vegetations on both mitral leaflets (red circles), in diastole (image A) and in systole (image B). **Image C** Long vegetation in systole (double-headed red arrow). **Image D** Same case in diastole: the curved red arrows show a small abscess in the posterior annulus.	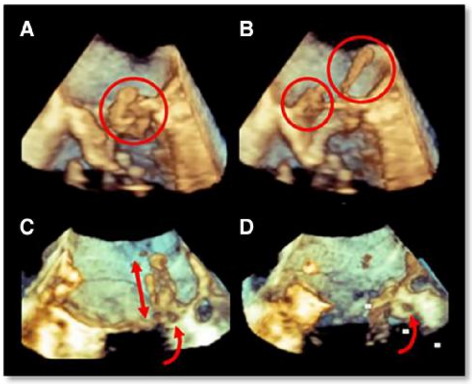
The 'kissing' effect occurs when a vegetation attached to the ventricular side of the aortic leaflet protrudes into the LVOT, 'physically' striking the ventricular surface of AML. This mechanism of propagation explains why the vegetation is attached to the ventricular surface of AML rather than on its atrial surface.	**Image A** 2D TOE long-axis view showing a long vegetation of ventricular surface of the anterior leaflet (white arrow) and the aortic vegetation (red arrow) in diastole. **Image B** Same case in systole. **Images C and D** 3D TOE of the same case in diastole and in systole, respectively. The red arrow points at the aortic vegetation. V, vegetation.	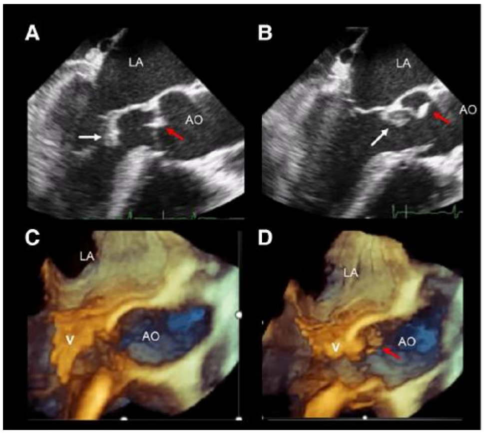
Complications of IE	**Image description**	**Image**
Leaflet perforation Severe regurgitation due to leaflet perforation (or to extensive leaflet erosion) identifies patients at risk of heart failure.	**Image A** 3D TOE showing a BAV with raphe from an aortic perspective. The arrows point at raphe and at perforation. The asterisk marks a dropout artefact. **Image B** The corresponding surgical view.	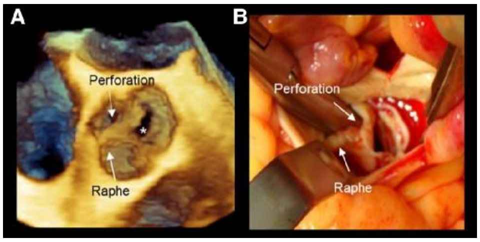

Continued

Table 28 Continued

Intracardiac tumoural masses		
Complications of IE	**Image description**	**Image**
Paravalvular aortic and mitral abscesses[92,93] These are the most life-threatening complications of IE. The most common sites of abscess are the annular regions. The rupture of a mitral annular abscess may cause a fistulous communication between the right and left ventricles, while a rupture of an aortic abscess may result in a communication between the AO and left or right atrium or between the AO and LV.	**Image A** 2D TOE long-axis view in a patient with aortic bioprosthetic who developed an aortic abscess (asterisk). The arrow points at the communication between abscess and LV. **Image B** 3D TOE corresponding image of image A. **Images C and D** Same case of images A and B. The images show the entry site (asterisk) in 'en face' view from an aortic perspective in two different moments of cardiac cycle. **Images E and F** 3D TOE glass view (image E) and CT (image F) showing a case of peri-annular channel around a mitral prosthesis, causing paravalvular regurgitation with systolic flow in the channel.	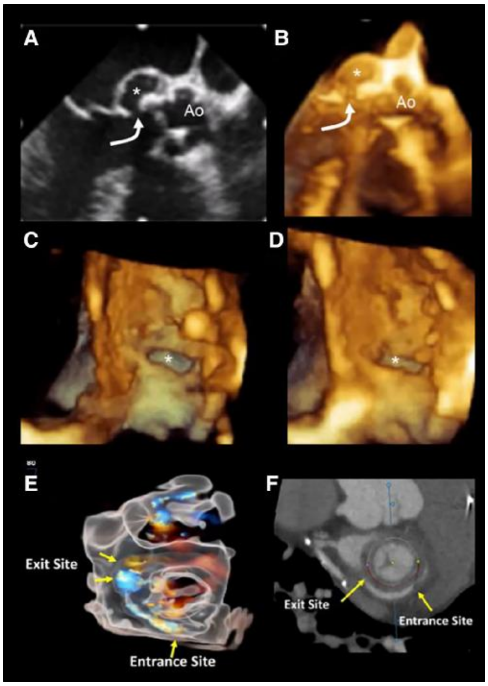
Protruding aortic atheroma[94] Protruding aortic atheroma within the AO may be a source of systemic embolization. Atheromatous plaques may be dislodged during cardiac catheterization. With the exception of aortic segment at the junction of the aortic arc and descending AO, 2D TOE remains the first-line and the most versatile technique for imaging aortic atheromatous plaques. 3D TOE provides an accurate definition of irregularities, protrusions, ulcerations, and mobile segments which are shown in a topographic map.	**Images A and B** Dual simultaneous images showing an irregular plaque. The arrow points at an excavation within the plaque. **Images C and D** 3D TOE of the same case in two slightly different perspectives. The plaque appears larger than that of 2D TOE. The arrows point to the cavern-like excavation.	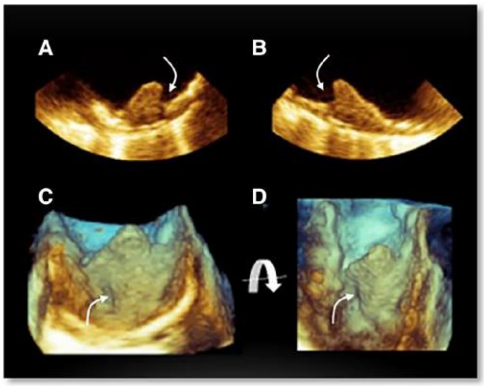

Section II

Part 2

Interatrial septum, patent foramen ovalis, and atrial septal defect

Introduction

Left-sided percutaneous structural heart diseases and complex electrophysiological procedures require access to the left atrium (LA) via transseptal puncture. Thus, a thorough understanding of the anatomy of the interatrial septum (IAS) is critical for a safe and effective crossing the IAS.[95–97]

Anatomy of normal IAS

The IAS is a fibro-muscular membrane that separates the LA and RA cavities and comprises the fossa ovalis (FO), the embryonic septum primum (SP), the septum secundum (SS), and the atrioventricular septum (AVS). The SS is an infolding of the atrial walls which surrounds the FO postero–superiorly, posteriorly, and postero–inferiorly, and it is filled by epicardial fat.

3D TOE has the unique ability to show the surface of the IAS from both LA and RA perspectives. Moreover, cropped sections show the different aspects of the FO and SS.

Table 29 describes the anatomy of the IAS and the corresponding 3D TOE images.

Table 29

Anatomy	Image description	Images
Orientation The IAS is oriented obliquely extending from the right–posterior to left–anterior position with an angle of ~60° with respect to the body in anterior–posterior position.	**Image A** 3D TOE 'large' zoom acquisition of the right side of the IAS. The volumetric data set is rotated to mimic the obliquity of the IAS with the body in the anterior–posterior position. **Image B** Fusion image showing the obliquity of the IAS in the anterior–posterior projection.	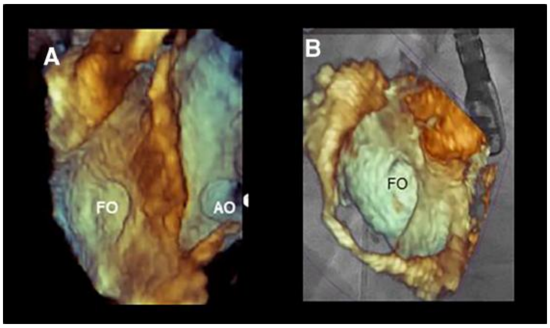
Acquisition 3D TOE images of the IAS can be acquired using all the available acquisition modes. The most effective is a single-beat acquisition from the bi-caval view. Progressive rotation and expansion of the volumetric data set in the **z**-axis direction allows obtaining the left side of the IAS.	**Image A** The image has been obtained with a zoom single-beat acquisition modality from the bi-caval view. **Image B** The image is progressively rotated up–down around the *x*-axis (curved arrow). **Image C** The image, showing the entire IAS, is obtained by increasing the volumetric data set in the z-direction (arrow). **Image D** The image is obtained with a rotation of 90° (curved arrow). The IAS is shown in attitudinal correct orientation.	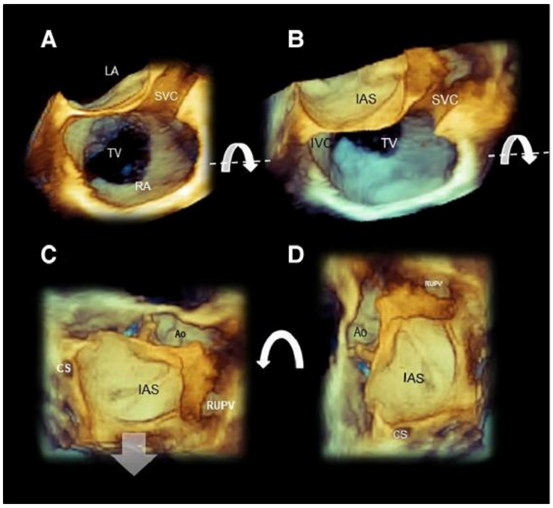
The left side The left side of the IAS is almost featureless. Usually, the surface of the FO is not entirely visible because of dropout artefacts. Rarely, a prominent ridge-like formation runs laterally to the FO. It can be speculated that this ridge is the result of an 'irregular fusion' between the FO and SS.[90]	**Image A** 3D TOE zoom modality of the left side of the IAS. The surface of the FO shows small holes due to dropout artefacts. These artefacts are primarily due to the thinness of the FO and to the fact that often the FO is not perpendicular to the ultrasound beam producing scattered rather than specular echoes. **Image B** 3D TOE zoom acquisition. The image shows the ridge (arrows).	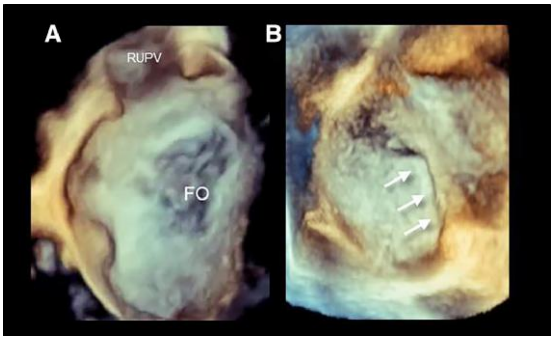
'**The septal pouch'**[97–100] is a blind-ended pocket due to an incomplete fusion between the SS and FO. The orifice of the pocket is more frequently open on the left side. Whether the stagnant blood in the pouch may contribute towards thrombus formation and be the source of emboli and cryptogenic stroke is still unclear.[96]	**Image A** 2D TOE bi-caval view showing a left pouch (arrow). **Image B** Same image in 3D. **Image C** 3D TOE in a photorealistic modality showing the septal pouch in 'en face' view (arrow) from the left perspective. **Image D** Same image rotated to visualize 'en face' the orifice of the pouch from the left perspective (arrow).	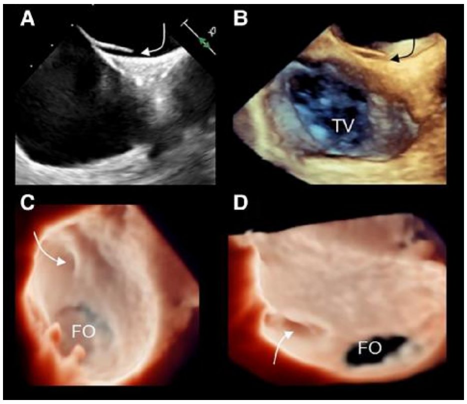

Continued

Table 29 Continued

Anatomy	Image description	Images
The right side When visualizing from the RA perspective, this region of the IAS appears to have a multifaced aspect: the FO is surrounded inferiorly by the IVC orifice, antero–inferiorly by the CS ostium, anteriorly by the septal leaflet of the TV, antero–superiorly by the non-coronary sinus of Valsalva of the AO, and superiorly by the SVC orifice.	**Image A** 3D TOE glass (transparency) mode showing the right side of the IAS. The particular position of the light source allows a clear vision of the 'crater-like' aspect of the FO. **Image B** Corresponding anatomic specimen (courtesy of Edgardo Bonacina, former pathologist at Niguarda Hospital Milan). **Images C–E** The right side of the IAS 'en face' view. An up-to-down rotation around the *x*-axis shows the inferior vena cava (IVC) (image D), while a down-to-up rotation shows the superior vena cava (SVC) (image E).	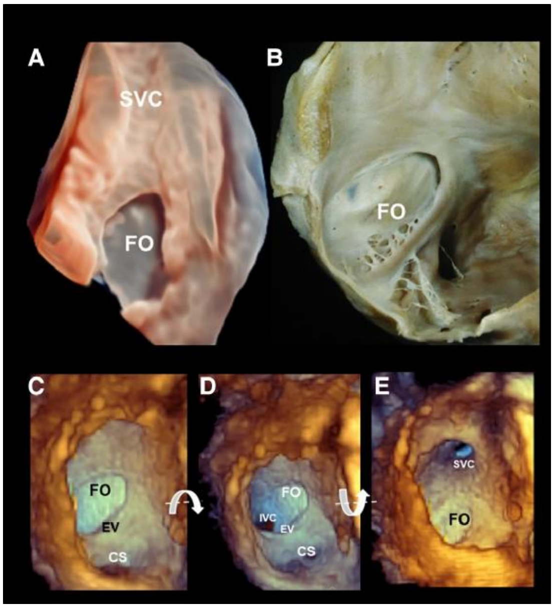
How to obtain a 3D TOE image of the right side One of the simplest ways is to use the zoom modality with the truncated pyramid which includes the IAS and surrounding structures [AO, left upper pulmonary vein (LUPV), superior vena cava (SVC), and CS]. From the left side, a right-to-left rotation of the volumetric data set allows acquisition of the right side of the IAS.	**Image A** 2D TOE bi-caval view. The truncated pyramid data set includes the IAS. **Image B** 3D TOE image obtained in zoom mode. **Image C** With a 90° rotation around the *z*-axis (curved arrow), the IAS is in a correct attitudinal orientation. **Image D–F** Progressive rotations right-to-left of the volumetric data set around the *y*-axis (curved arrows around the *y*-axis) reveal the right side of the IAS. (Modified with the permission of Faletra et al. JASE 2019)	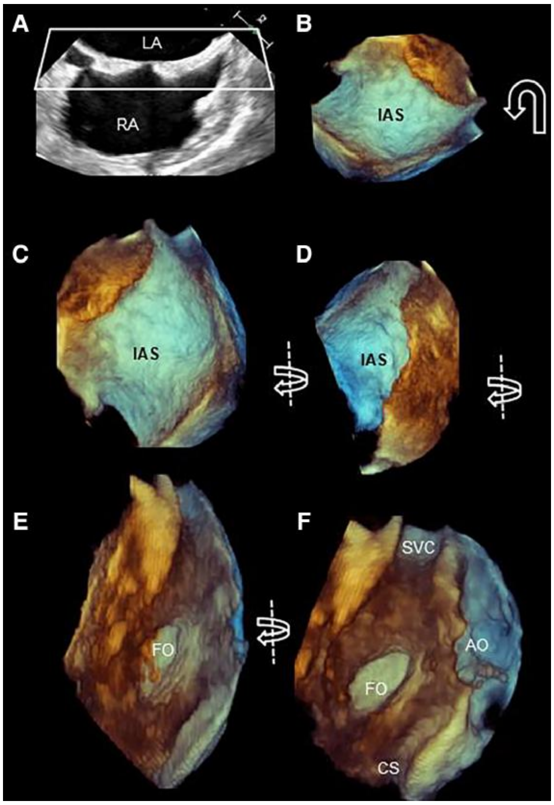

Continued

Table 29 **Continued**

Anatomy	Image description	Images
The 'true' IAS The FO is surrounded by the SS which is an infolding of the atrial wall (composed by a variable amount of epicardial fat) rather than a true muscular ridge. Consequently, the so-called lipomatous hypertrophy of the IAS is nothing else that an exaggerated amount of epicardial fat in this fold. Puncturing the SS means puncturing the RA wall and, consequently, causing an exit of the needle into the infolding (i.e. outside the atria).	**Image A** 3D TOE in a longitudinal cross-section. A normal IAS. The folding of SS is almost virtual. **Image B** Lipomatous IAS. The fat fills the infolding separating the atrial wall, but remains outside the heart. **Images C and D** 2D TOE still frames showing an incorrect trans-septal puncture. The needle (arrow) crosses the SS, instead of the FO.	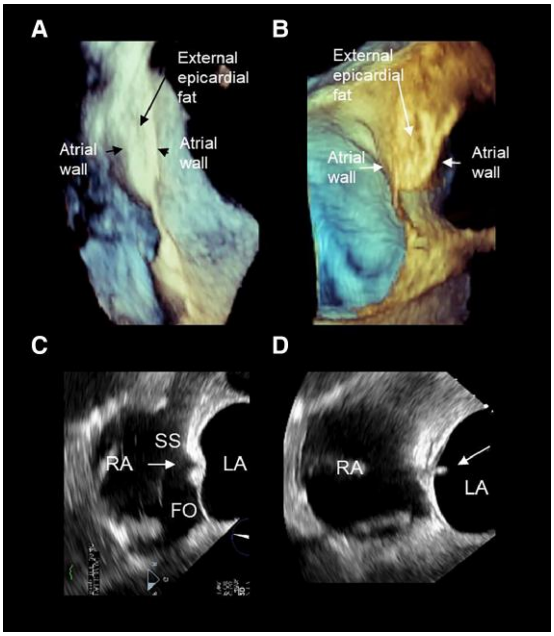
Atrial septal aneurysm[101,102] Atrial septal aneurysm is a redundancy of the FO tissue, forming a saccular protrusion with an excursion of greater than 10 mm into either the LA or the RA or a total excursion of 15 mm. 2D and 3D toe are the most common imaging techniques for evaluating this entity	**Image A** 3D TOE zoom acquisition of an aneurysm of the FO (arrows). Usually, the aneurysm protrudes into the RA cavity.	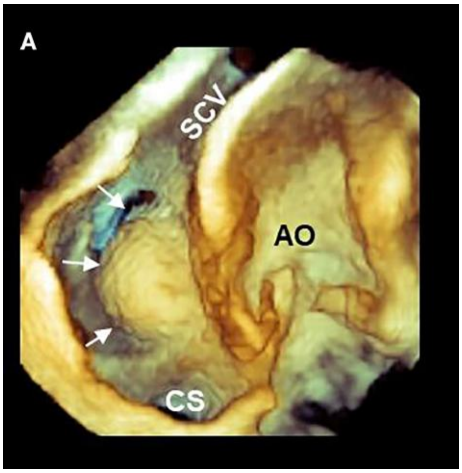

Patent foramen ovalis and atrial septal defect

During foetal life, the SP opens leftward, allowing oxygenated blood to flow from the right to left atrium. The higher pressures in the LA, after birth, push the SP onto the SS, closing the foramen functionally first and anatomically afterward. In adult life, the incidence of TOE-detected patent foramen ovalis (PFO) is approximately present in 25% of the population. Although considered a normal variant, PFOs have been associated with a variety of clinical conditions including cryptogenic stroke, migraine headaches, sleep apnoea, and decompression illness.[103,104]

Excluding BAVs, atrial septal defects (ASD) are the third common congenital cardiac anomaly in adults with an approximate prevalence of 1 out of 1000 individuals. There are five types of atrial communications that allow shunting of blood between the systemic and the pulmonary circulations: the secundum ASD, primum ASD, sinus venosus ASD inferior and superior, and coronary type ASD.[105] 3D TEE allows for accurate visualization of the size and shape of the defect and its rims on unique 'en face' views either from the right or from the left side.

Table 30 shows 3D TOE examples of PFO and describes the five types of ASDs and the corresponding 3D TOE images.

Table 30

Anatomy	3D TOE image description	Image
PFO		
'**PFO**' is an intermittent space/tunnel between SP and SS due to an incomplete sealing of the SP and SS after birth. PFO is located in the anterosuperior portion (between the aortic root and SVC) of the FO. 3D TOE offers a panoramic view of PFO either in en face from the right and left perspectives or in cross-section.	**Image A** 3D TOE zoom acquisition showing the PFO from the LA perspective. **Image B** Same case from the RA perspective. **Image C** 3D TOE cross-section showing a tunnel-like appearance of the PFO (arrow). **Image D** Same case with contrast injection during Valsalva manoeuvre. Commonly, this manoeuvre is performed with 2D TOE. However, 3D TOE is equally effective. The red circle shows the contrast in LA.	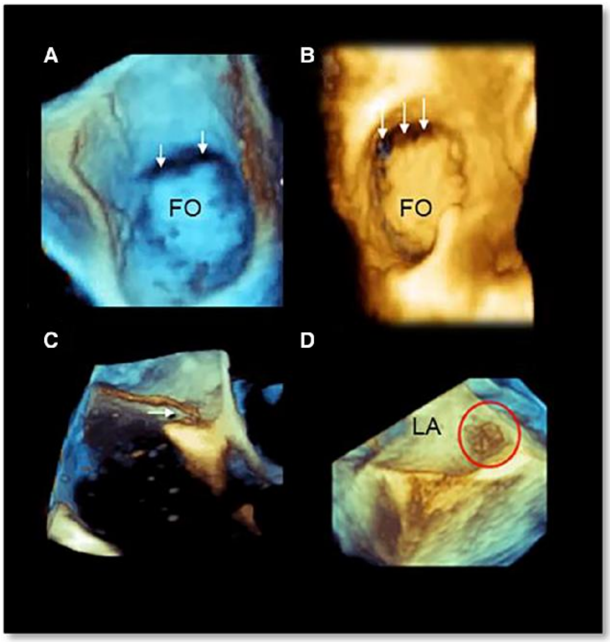
ASDs		
Image A 3D TOE zoom acquisition showing the right side of the IAS and surrounding structures such as FO, AO, CS, superior vena cava (SVC), inferior vena cava (IVC), and TV. **Image B** Same image with the location of the five types of ASDs superimposed.. **Image C** 3D TOE zoom acquisition showing the left side of the IAS and surrounding structures. **Image D** Same image with the location of the five types of ASDs superimposed.		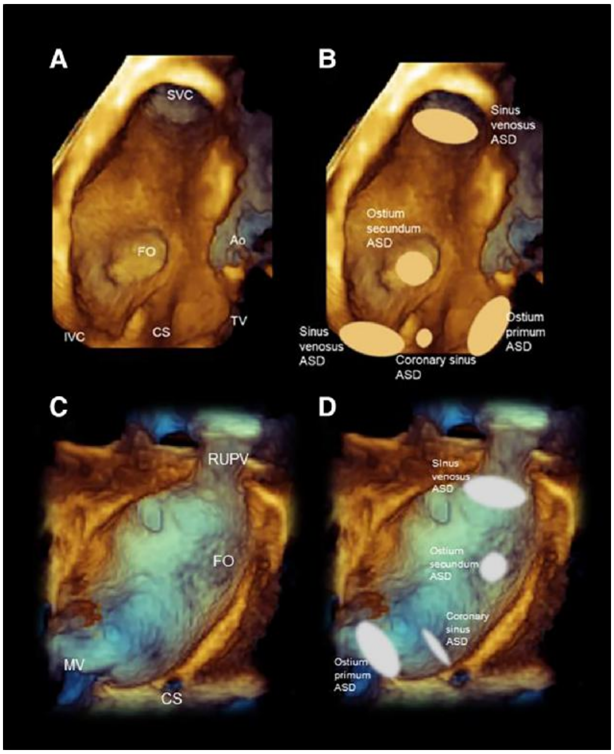

Continued

Table 30 Continued

Anatomy	3D TOE image description	Image
Secundum ASD '**Secundum ASD**' is the most common ASD. In adults, this type of defect comprises about 75% of all ASDs. 3D TOE has shown this defect is located within the borders of the FO and has variable size and variable shape. It can be isolated or fenestrated with multiple holes.	**Images A and B** 3D TOE images of a secundum ASD obtained using a zoom mode from the left (image A) and right side (image B). **Image C** 3D TOE images of secundum ASD with photorealistic modality. **Image D** Fusion image showing the ASD in the right oblique anterior projection. **Images E and F** 3D TOE image of multi-fenestrated ASD and the corresponding surgical findings. The asterisks point at the holes.	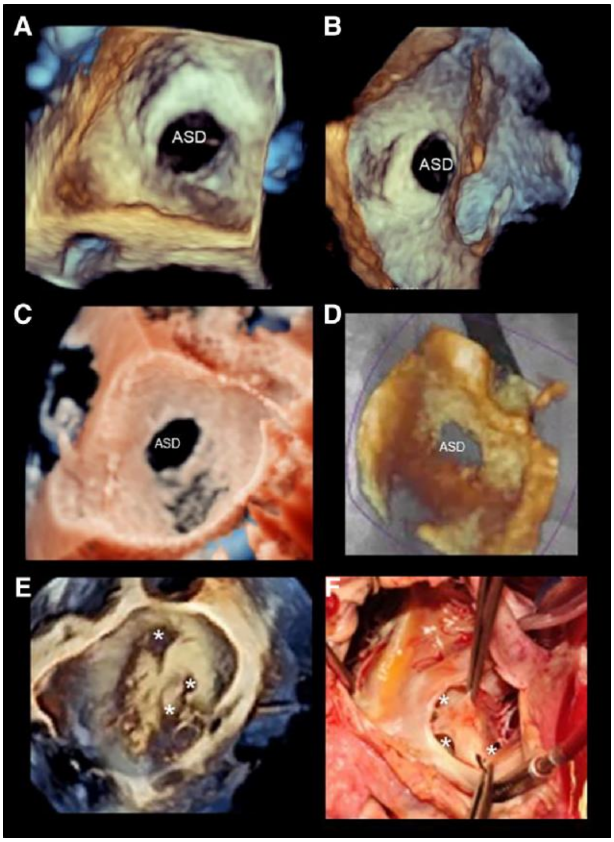
3D TOE colour Doppler of ASD Visualization of the flow crossing the ASD using 3D TOE colour Doppler is an additional extremely useful tool that allows better definition of the margins of the defect and distinguishes true communications from dropout artefacts.	**Image A** 3D TOE colour Doppler of a secundum ASD 'en face' view from the LA perspective. Note the margins of the defect are well defined. **Image B** 3D TOE colour Doppler showing the defect in cross-section. The blood flows from the right upper pulmonary vein (RUPV) directly through the defect (red arrow). **Image C** 3D TOE showing several holes (asterisks). **Image D** The colour Doppler clarifies the position of the true defect (red arrow).	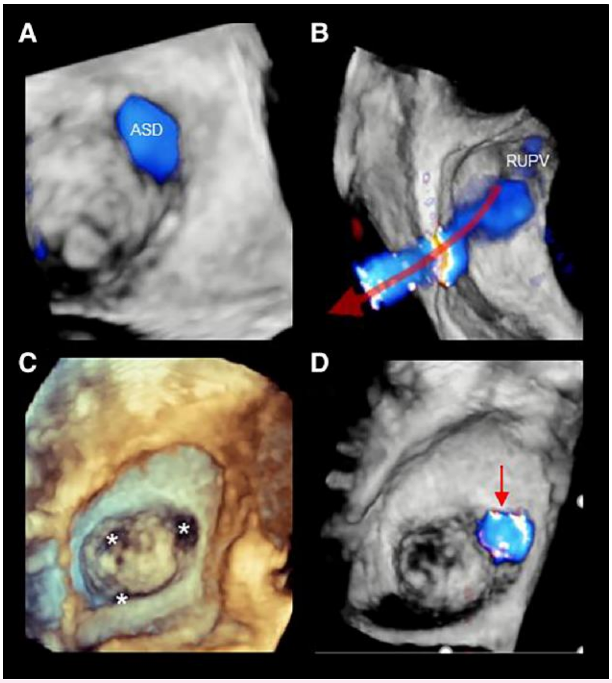

Continued

Table 30 **Continued**

Anatomy	3D TOE image description	Image
Dynamic morphology of secundum ASD 3D TOE has revealed significant changes in the size of an ASD during the cardiac cycle. These changes occur because the SS is actually the atrial wall and follows the contraction of atrial cavities which are smaller during ventricular diastole and larger during the ventricular systole.	**Image A** 3D TOE image from the left perspective showing an ASD during ventricular diastole. **Image B** Same case during ventricular systole. The difference in size is evident. **Image C** 3D TOE colour Doppler image from the left perspective during ventricular diastole. **Image D** Same case during ventricular systole. The difference in size is evident.	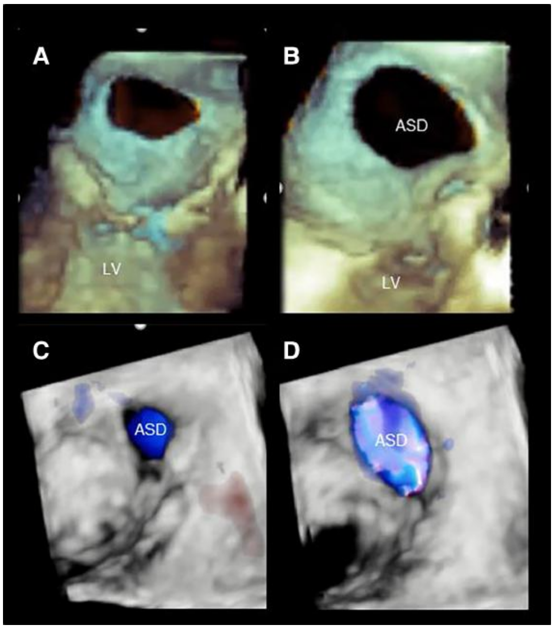
Quantification of secundum ASD size. The size of the defect and the lengths of residual rims) can be assessed using multiplanar reconstruction. Theoretically, sizing of the defect may be measured directly on the 3D image. However, rims on the atrial wall are rather indistinct on 3D volume rendering images.	**Image A** ASD devices require a rim length of at least 5 mm, with the exception of the aortic rim for which a length of 2 mm is considered sufficient for stable anchorage.	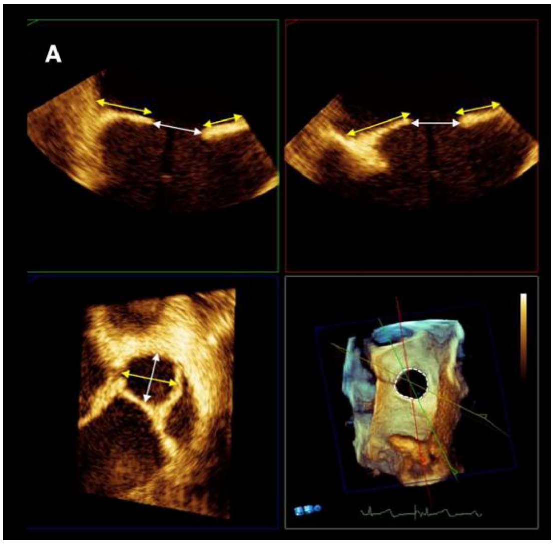
Ostium primum ASD 'Ostium primum ASD' or atrioventricular septal defect results from the failure of partitioning of the atrioventricular canal and accounts for ∼15% of ASD cases.	**Image A** 2D TOE showing the left to right shunt of an isolated ostium primum ASD. **Image B** 3D TOE image showing an ostium primum ASD en face from the LA perspective. (modified image with the permission of Faletra et al. JACC imaging 2020)	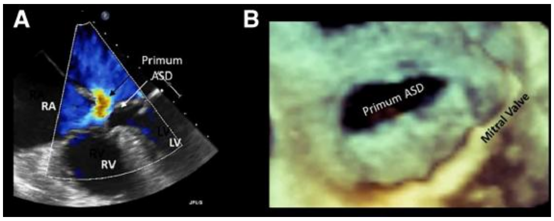

Continued

Table 30 Continued

Anatomy	3D TOE image description	Image
Sinus venous ASD		
'Sinus venosus defects' (superior and inferior) comprise about 5–10% of all ASDs and results from partial or complete absence of the SS. When it is the superior type, this ASD involves the right PV/s, superior vena cava, and the posterior wall of the RA, while the inferior type involves the inferior vena cava.	**Image A** 2D TOE short-axis view of the AO showing the sinus venous ASD (curved arrow). 3D TOE showing the ASD 'en face' view. The defect is clearly in a position that is superior to the FO.	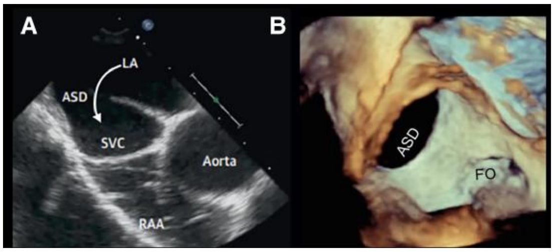
Imaging patients with a previous ASD occluder in place		
Patients with a recent ASD occluder need follow-up for monitoring potential complications such as pericardial effusion, device instability, aortic root erosion, impingement on adjacent structures, and thrombus. 3D TOE provides a panoramic view en face from both sides and useful images in cross-sections.	**Image A** 3D TOE volume rendering showing the left disc (LD) 'en face' from the left perspective. **Image B** 3D TOE volume rendering in cross-section, showing the LD and right disc (RD). **Image C** 3D TOE image using photorealistic modality. **Image D** 3D TOE image using photorealistic modality with the source of light behind the device. This specific image allows visualization of the septal tissue between the two discs (arrows).	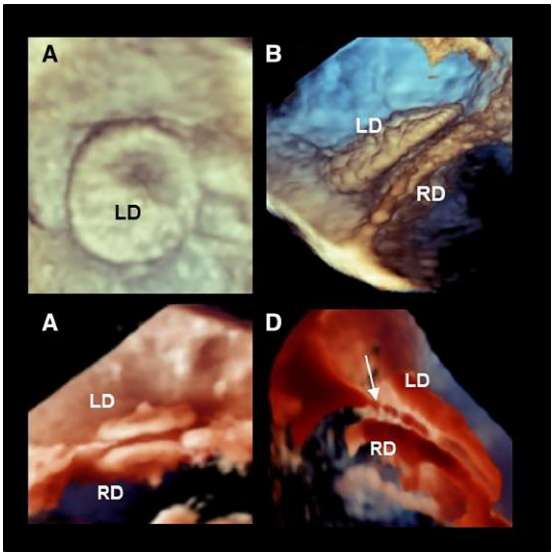

Section II

Left and right atrium

Introduction

2D TOE is routinely used to rule out the presence of thrombi in the atrial chambers before an electrical cardioversion and atrial arrhythmia ablation or in the setting of suspected cardiac origin of a cerebral vascular accident.[106] Furthermore, a detailed echocardiographic analysis of LA and RA anatomy has become crucial for transcatheter treatments of atrial arrhythmias, as well as for congenital or structural heart diseases. The atria are, in fact, part of the access pathways to the atrioventricular valves, enabling transcatheter interventions on TV and, via trans-septal access, on MV.

The RA

There are important anatomical landmarks of RA, such as the RA appendage (RAA), RA vestibule, Eustachian valve (EV), CS ostium, crista terminalis (CT), and cavotricuspid isthmus (CVTI). 3D TOE is probably the best image modality for a detailed assessment of RA structures which can be viewed from a countless number of different perspectives and in relation to neighbouring structures.[107] Anatomical description of RA structures and 3D TOE corresponding images are illustrated in *Table 31*.

Table 31

Anatomy	3D TOE image description	Image
RA appendage (RAA) The RAA appears as a triangular protuberance in the area of the anterior RA with the apex pointing superiorly. The internal surface of the RAA consists of pectinate muscles that form a dense network. The atrial wall in between PMs may be exceedingly thin, comprising only few-millimetre thickness of atrial myocardium sandwiched between the epicardium and endocardium. A sagittal bundle (SB) is usually prominent and crosses the RAA wall transversely. The orifice of RAA is large, allowing a more favourable 'washing out' of blood flow. Indeed, the presence of thrombi in RAA is rare. The RAA vestibule is located between the RAA ostium and the TA. The external aspect of the vestibule is covered by substantial amount of fat along the epicardial side of the tricuspid annulus.	**Image A** 2D TOE from mid-oesophageal level showing the RAA, the CT, and the PeMs (arrows). The red truncated pyramid marks the boundaries of zoom acquisition. **Image B** 3D TOE zoom modality of image A showing the CT, the superior vena cava (SVC), and the RAA. **Image C** 2D TOE from deep trans-gastric level showing the RAA and the CT. The red truncated pyramid marks the boundaries of the zoom acquisition. **Image D** 3D TOE image of RAA from this view. **Image E** 3D TOE image of RAA using a photorealist modality. The PeMs (arrows) are clearly seen. **Image F** 3D TOE image obtained with large zoom modality acquisition showing the RA vestibule. The dotted line marks the hinge of TV.	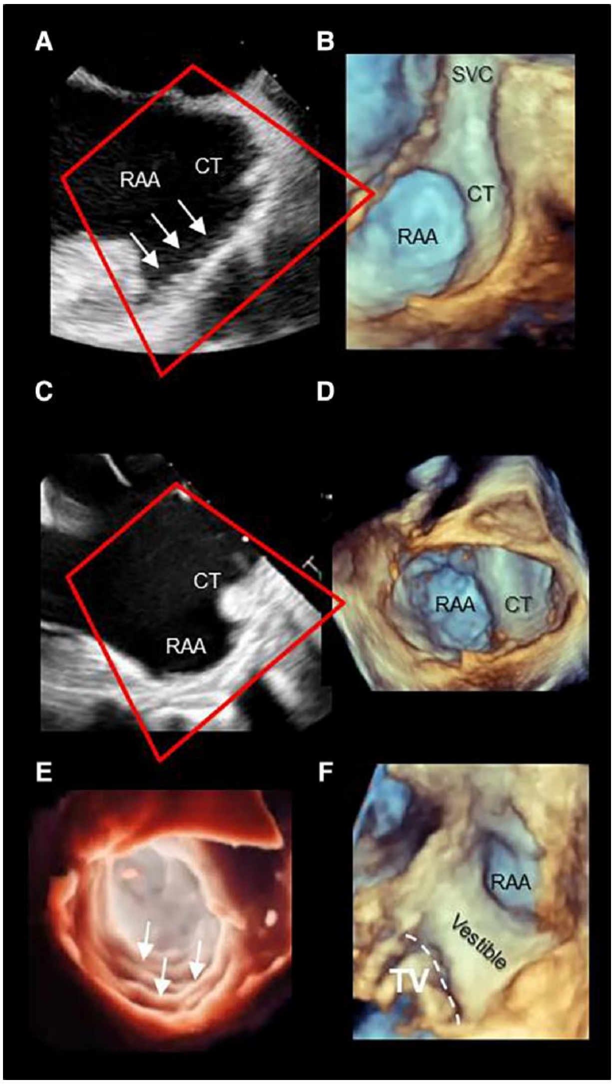

Continued

Table 31 Continued

Anatomy	3D TOE image description	Image
The CT is a muscle bundle that marks the boundary between the smooth surface of the venous system and the rough surface of the RAA.[107] It begins in the area of the antero–medial wall of the RA, merging from the Bachmann bundle, and continues along the anterior border of the SVC orifice; then, it curves laterally and descends slowly towards the IVC, where it branches into smaller bundles. From the CT arises a series of PeMs. The sinus node lies in the musculature of the CT, usually at the anterolateral junction with the SVC. The CT is target for ablation of focal atrial tachycardias.[108]	**Image A** 3D TOE image in zoom modality focused on the superior part of CT. Merging from the superior/medial part RA wall, the CT forms a kind of 'arcade' (arrows) before descending towards the inferior vena cava. **Image B** 3D TOE image in zoom modality showing the PeMs arising in oblique fashion from the CT (dotted lines). The CT ends near the IVC branching into small bundles (arrows).	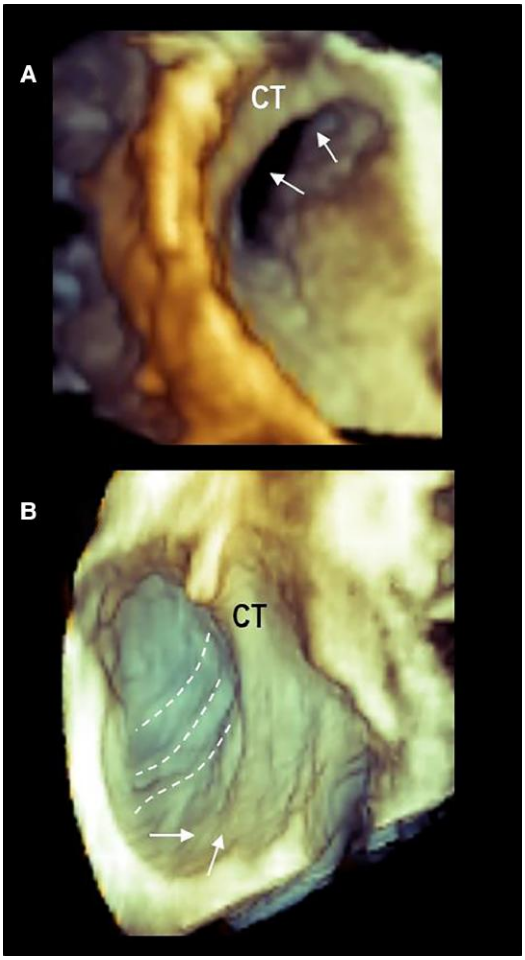
The CVTI **The CVTI** is a quadrangular endocardial region bounded anteriorly by the hinge line of the posterior and septal leaflets of the TV, posteriorly by the EV and IVC, medially by the CS, and laterally by remnants of the CT. The CVTI region is responsible for isthmus-dependent typical atrial flutter, and it is a target for linear ablation. Routine pre-procedural 3D TEE imaging is extremely helpful in qualitative and quantitative evaluation of CTI anatomy in patients undergoing RFA for symptomatic typical atrial flutter. Detection of a deep RA pouch was found to be associated with significantly prolonged CTI ablation time to achieve bidirectional block.[109,110]	**Image A** 3D TOE cross-section four-chamber view. The brown transparent surface marks the boundaries of CVTI. **Image B** 3D TOE cross-section short-axis view through the AO. The blue transparent surface marks the boundaries of the CVTI.	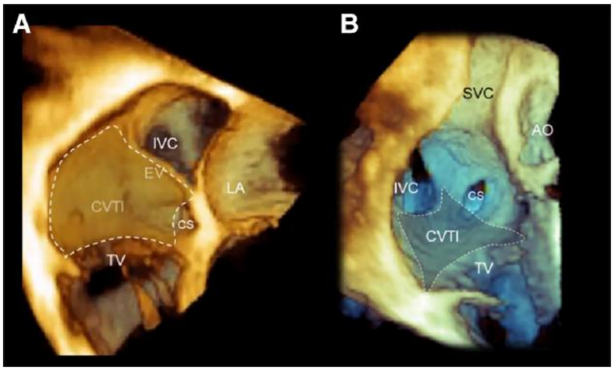

Continued

Table 31 Continued

Anatomy	3D TOE image description	Image
'**The CS ostium**' is located between the opening of the IVC and TV. The Thebesian valve (ThV) guards the CS orifice and typically has a semilunar aspect usually covering up to >75% of the CS ostium. The ostium is the gateway for indirect annuloplasty approaches and for left ventricular pacemaker leads; a prominent ThV may hinder the insertion of wires, catheters, and devices and leads into the CS.[107]	**Image A** 3D TOE cross-section image in slightly oblique four-chamber view, to maximize the CS orifice. **Image B** Magnified image of the structure inside the red box of image A. The image shows the coronary CS ostium guarded by the ThV.	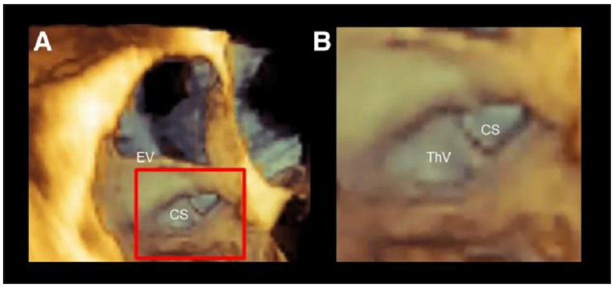
The EV is an embryonic remnant of the inferior portion of the right sinus venosus valve. It may persist in the inferior vena cava (typically as a semilunar flap) and project into the RA.[107] In ∼10%, a sub-Eustachian pouch (or sinus of Keith) is present just lateral of the CS ostium. A large EV and/or a deep sub-Eustachian pouch may interfere with the linear ablation preventing contact with ablation catheter.[107] Depending on its size and extension, a prominent EV may interfere with the manoeuvring of wires, catheters, delivery sheaths, and devices.[107] Thrombus formation and bacterial endocarditis have been described in large EVs,[111] The Chiari network is an embryonic vestigial of the foetal EV. This structure is best visualized with 2D rather than with 3D TOE.	**Image A** 3D TOE zoom modality cropped longitudinally through the superior vena cava (SVC). The image shows the EV and its anatomical relationship with inferior (IVC) and SVC. **Image B** 3D TOE image of EV in four-chamber view. The image shows the anatomical relationship of EV with IVC and CS. **Image C** 3D TOE image of a thin EV. **Image D** 3D TOE image of a thick EV with a sub-eustachian pouch (P). **Images E and F** 3D TOE image of EV seen from the IVC perspective (image E) and from the atrial perspective (image F).	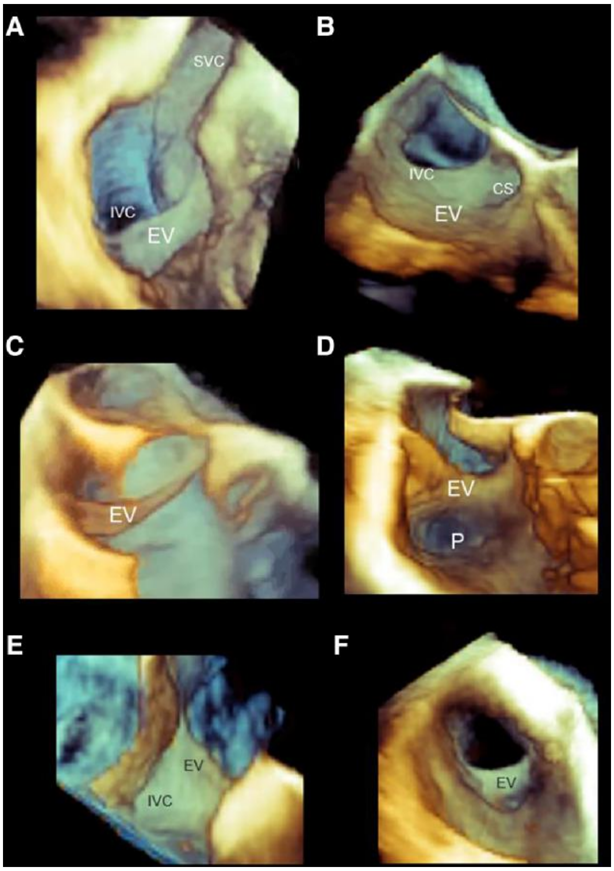

The LA

The LA is adjacent the oesophagus, separated by a thin space filled up by adipose tissue and small oesophageal arteries and veins.[112]

The LA can be divided into four parts: (i) the vestibulum, (ii) four pulmonary veins (PVs), (iii) left atrial appendage (LAA), and (iv) IAS.

Pulmonary veins

Most commonly, there are two PVs for each lung. The ostia of the superior PV tend to be larger. The anatomical variants are frequent. In around 15% of the population, the left upper and lower PVs merge into a common trunk, while on the right side, an accessory vein entering independently is rather common. PVs are target for atrial arrhythmia ablation.

Theoretically, 3D TOE imaging of the roof of the LA should visualize all of the four PV ostia. However, the right and left pairs of veins are widely separated and lie very close to the transducer. At this transducer distance, the pyramidal beam is too narrow to visualize the four PVs and the two pair of PVs must be visualized using two different approaches.[113]

Table 32 illustrates the 3D TOE images of the right and left PVs.

Table 32

Right PV anatomy	3D TOE image description	Image
Right PV ostia open adjacent to the IAS. A zoom modality which includes the superior part of the IAS and adjacent structures, and a slight counter-clockwise rotation of the probe allows the visualization of right PVs in 'en face' view.	**Images A and B** 2D TOE *x*-plane imaging modality. The red truncated pyramidal data show the zoom modality includes both the right PVs. **Images C and D** 3D TOE zoom modality showing 'en face' view of the right upper (RUPV) and lower (RLPV) pulmonary veins in rendering (image C) and in photorealistic modality. **Images E–H** Zoom modality of the entire IAS. Four still frame images show the use of an up-to-down rotation (curved arrow around *x*-axis), which visualizes both the RUPV and RLPV.	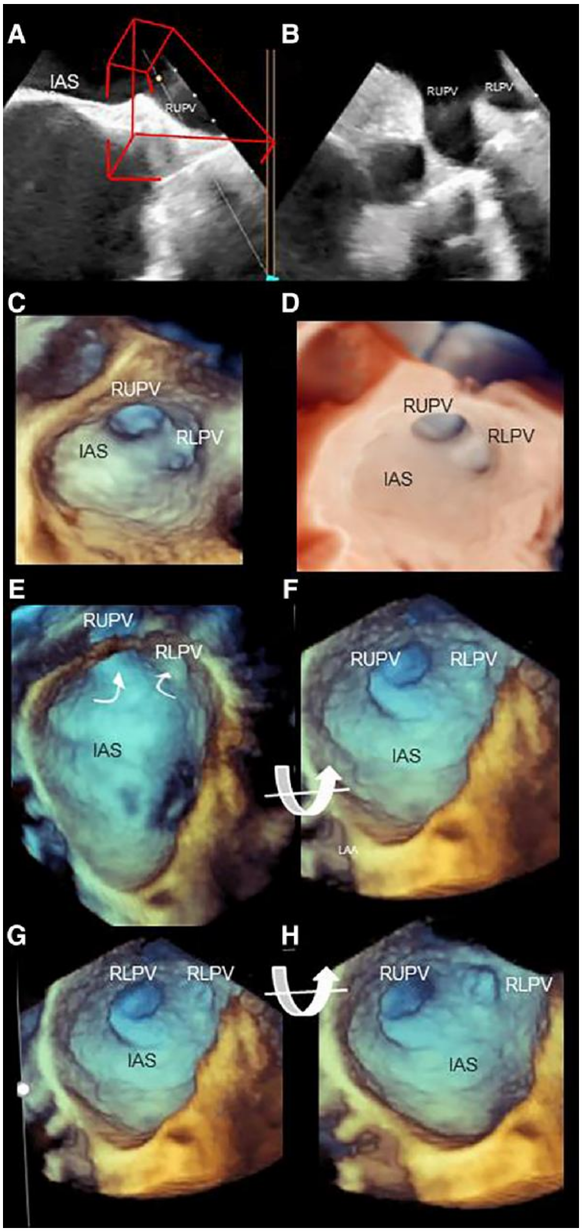

Continued

Table 32 Continued

Left PV anatomy	3D TOE image description	Image
The easiest way to visualize the LUPV is by using the zoom modality of LAA. Once the LAA is visualized, a slight counter-clockwise rotation of the probe allows visualizing the ostium of the LUPV. The LLPV is more difficult to visualize in the same image because it enters into the atrial cavity at a different angle. Thus, a perfect side-by-side 'en face' view of both ostia may be difficult to obtain from a single pyramidal data set, unless the LA is enlarged and the left PV orifices outstretched.	**Image A** 2D TOE cross-section showing the LAA, left lateral ridge (LLR), and LUPV. The trunked pyramid marks the structures included in a zoom modality. **Image B** 3D TOE zoom mode, showing in 'en face' view the LAA, LLR, and LUPV. **Images C and D** 3D TOE zoom modality showing the outstretched LV orifices in volume rendering (image C) and in photorealistic modality (image D). **Image E** Cropped 3D TOE image of left PVs. A right-to-left rotation (curved arrow) allows obtaining the left PVs in long-axis view. **Image F** Left PVs in long-axis view. IVR, intravenous ridge.	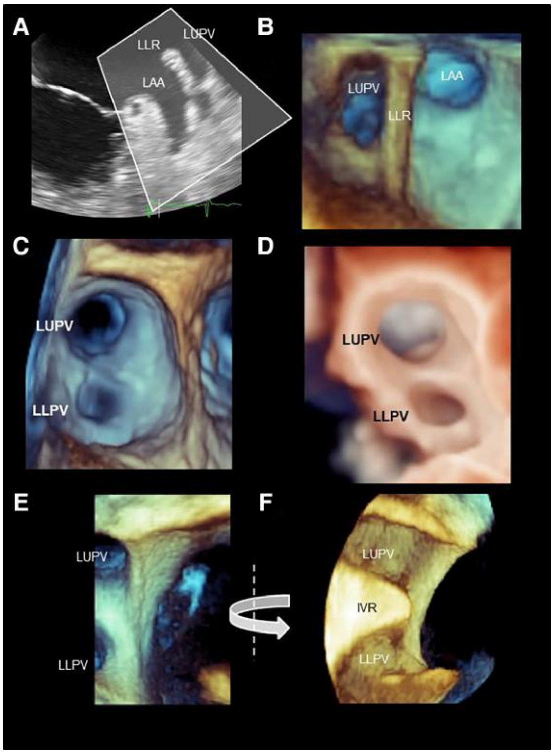
The left lateral ridge (LLR)[114] The LLR (also called coumadin ridge, Marshall ligament, or Q-tip sign) is the most prominent structure protruding into the left atrium. Notably, the LLR is not a muscular ridge but an enfolding of the atrial wall. On the epicardial site of the enfolding, within the adipose tissue, atrial arteries and veins, nerve bundles, and, not infrequently, the oblique vein of Marshall that opens into the CS can be found.	**Image A** 3D TOE showing the orifices of LAA and the LUPV in 'en face' view. The arrow points at the LLR. **Image B** A cross-section of the LLR. The LLR is an enfolding of the atrial wall (curved arrow).	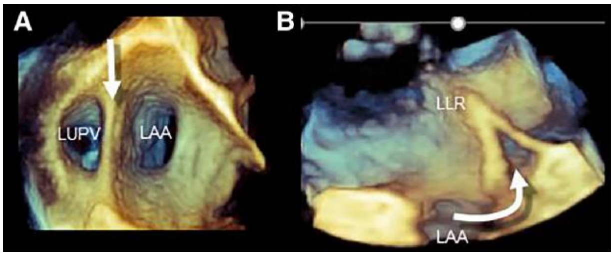

LAA

The LAA is a finger-like extension that derives from the embryological LA. The remaining walls of the LA in adults derive from an outgrowth of the PVs. The LAA covers the atrioventricular groove laterally and anteriorly, in close proximity with the left circumflex artery. Its structure is usually multi-lobar and high trabeculated due to a mesh of pectinate muscles (PeMs). A narrow orifice joins LAA with the smooth venous component of the LA. This anatomic configuration favours blood stasis and thrombi formation. A classification (made by CT) divides the LAA into four sub-types: 'chicken wing', 'cauliflower', 'cactus', and 'windsock'.[115] This classification may be useful in clinical practice since it may be associated with the risk of thrombus formation into the LAA and may influence the choice of the location on device implantation and the type and size of device.

3D TOE provides images of excellent quality of shape and dimensions of LAA. Indeed, LAA is positioned closed to the transducer and the small size of LAA allows using narrow angle with a high line density and high temporal resolution. Currently, there are five 3D TOE modalities for imaging the LAA: (i) B-plane mode; (ii) 3D TOE volume rendering 'en face' view, (iii) 3D TOE cropped views, (iv) photorealistic/transparency mode, and (v) multiplanar reconstruction.

Table 33 shows 3D TOE images of normal anatomical LAA structures as well as of thrombi/sludge.

Table 33

LAA	Images
The position of LAA **Image A** 3D zoom modality with a wide sector (high temporal resolution is not specifically required for atrial structures) shows a large panoramic view, which allows establishing the spatial relationship between LAA and surrounding structures: such as LUPV, LLR, AO, and MV **Images B and C** 2D TOE (image B) and 3D TOE (image C) of fusion images showing the position of LAA in antero–posterior projection.	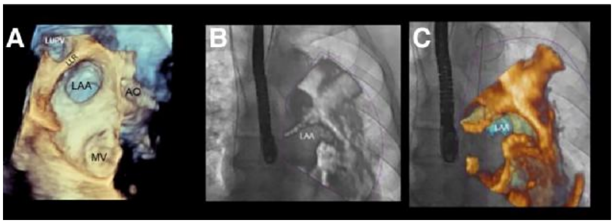
B-plane mode B-plane imaging is currently one of the most useful display modalities. It can be used moving the lateral plane to scan the entire LAA morphology, exploring different lobes and distinguishing PeMs from the thrombus. **Images A and B** show an example of B-plane acquisition. The yellow arrows point at PeMs.	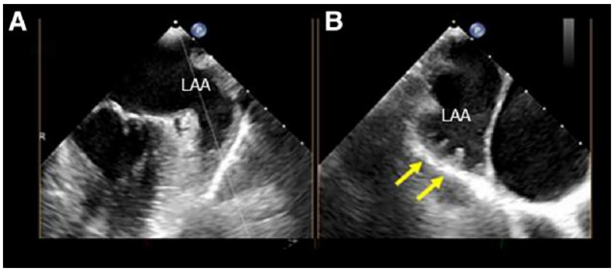
Volume rendering modality This modality allows visualizing the LAA from a countless number of perspectives. The most clinically useful is the view from above cross-section views. **Images A and B** show the same case of LAA seen from above (image A) and after having longitudinally cropped the volumetric data set. Both images show the PeMs (arrows). **Image C** 3D TOE showing four still frame images of LAA from an atrial perspective. A cropping plane (transparent oblique square) advances from left to right (arrow). **Image D** The image shows four still frame images corresponding to the image of line C. These images have been obtained by rotating the volumetric data set from left to right (curved arrow) around the ***y***-axis. As the 'cropping' plane advances, lobes appear and disappear (arrows), protruding in the three spatial directions.	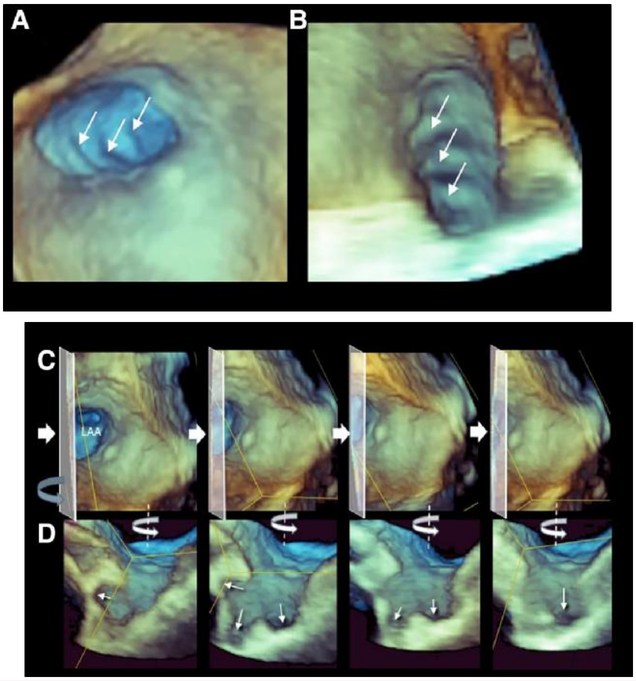

Continued

Table 33 **Continued**

LAA	Images
Glass (transparency) modality This tool allows obtaining a kind of ultrasonic cast which parallels the external shape of LAA. **Image A** has a low degree of transparency. Thus, the atrial wall is partially superimposed to the LAA (asterisk). The LAA appears having just one lobe (curved dotted line). **Image B** Same 3D TOE data set of image A. The volumetric data set has been slightly rotated left-to-right around the *y*-axis, and the transparency has been increased. With these adjustments, the LAA has two lobes (curved dotted line). **Image C** 3D. The image shows the external shape of the LAA. **Image D** Same case of image C. By increasing the transparency, PeMs (asterisk) can be recognized inside. **Image E** 3D TOE glass modality of LAA. **Image F** Same case of image E. A slight rotation of image allows visualizing the ostium (curved arrow).	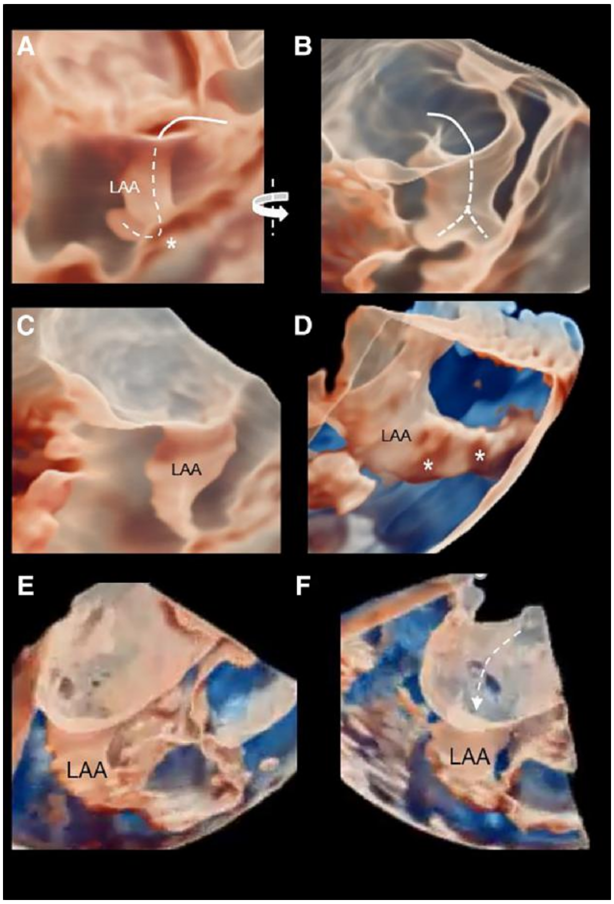
Multiplanar reconstruction This modality uses the 3D TOE data set to reconstruct 2D TOE images in any desired imaging plane. This modality is particularly useful for measuring the diameter, length, and orifice circumference of the LAA to guide device selection and site of device implantation. **Images A and B** 2D TOE perpendicular images. The yellow dotted line measures the diameter of the orifice, while the white dotted line measures the diameter of the landing zone. **Image C** The image shows the measurement of the circumference in cross-section. **Image D** The 3D TOE volume rendering mode.	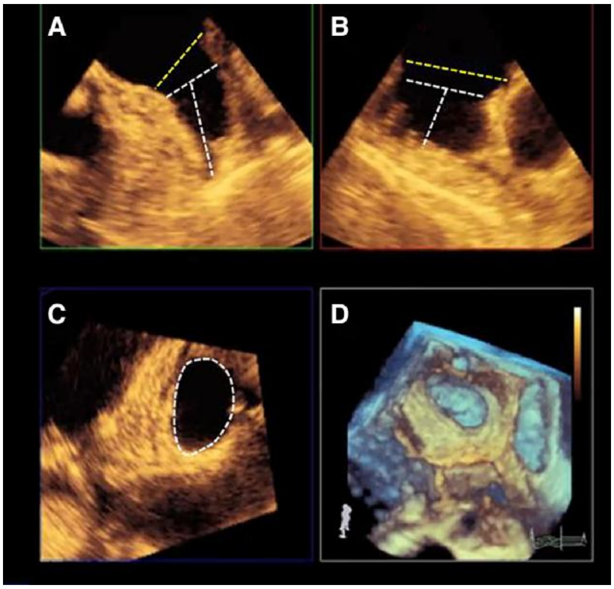

Continued

Table 33 **Continued**

LAA	Images
Thrombi in LAA 3D TOE uses shades of colour for perceiving depth rather than texture. Thus, 3D TOE is less effective than 2D TOE for ruling in/out thrombi. **Image A** 2D TOE image of a thrombus (T) in LAA. The presence of a large thrombus, which appears softer than the surrounding muscular tissue. **Image B** Same case of image A. With 3D TOE, the thrombus appears as a mass in the LAA with the same shades of yellow/brown of surrounding muscular tissue. **Image C** 2D TOE showing a thrombus partially fibrotic/calcific on its surface (arrow), producing two different levels of grey. **Image D** 3D TOE image of the same case of image C. The thrombus appears as a mass protruding from the LAA with the same colour of the surrounding muscular structures. **Image E** 3D TOE appearance of a sludge (S). The brown colour is easily distinguishable from the surrounding tissue. **Image F** 3D TOE image of small thrombus attached in the middle of LAA. In this example, the 3D texture of the thrombus (slightly brown) can be differentiated from surrounding muscular (green/yellow/beige) structures, because the thrombus is located at a different depth.	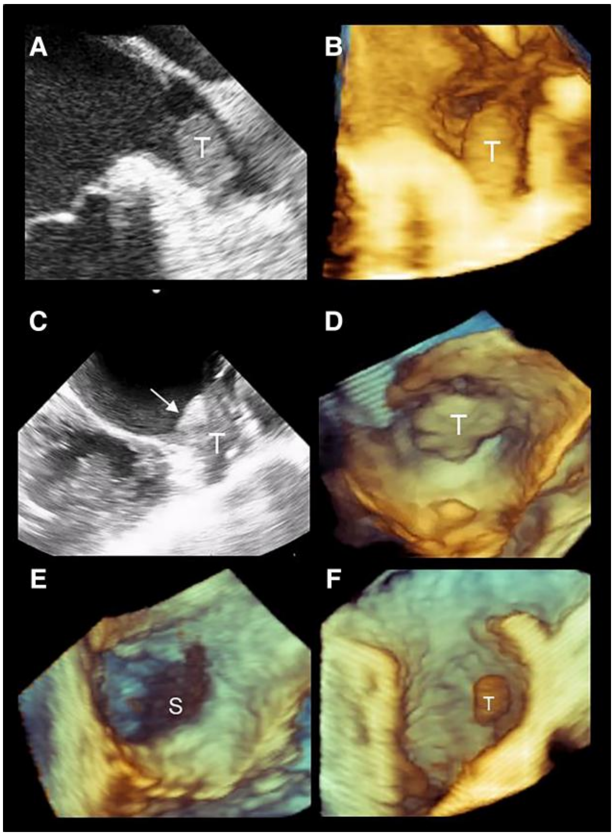

Section II

Ventricular septal defect

Normal 3D TOE aspect of interventricular septum (IVS)

An in-depth knowledge of the normal 3D TOE aspects of the of the IVS (i.e. location, relationships with adjacent muscular and/or fibrous septum, and surrounding atrioventricular or semilunar valves) is mandatory for a full understanding of ventricular septal defects (VSD).[116]

A normal IVS can be divided anatomically into two parts: the muscular and membranous.

Like the IAS, 3D TOE has the ability to show 'en face' either the right or the left side of IVS.

Table 34 briefly describes the anatomy of the IVS and the corresponding 3D TOE images.

Table 34

Anatomy	Image description	Image
The muscular IVS The muscular IVS is an extensive non-planar muscular partition between the two ventricles. In cross-section, the muscular IVS has a curved-shaped arrangement. The convex surface is towards the RV, while the concave surface is towards the LV. As a consequence, the right surface is larger than the left surface, and it is used to describe the location of VSDs. Although real anatomic boundaries do not exist, the muscular septum can be roughly divided into three components: the inlet, the trabecular, and the outlet component. '**The inlet component**' begins at the levels of atrioventricular valves and ends approximately at the level of chordal attachment. '**The trabecular component**' extends from the membranous septum (MS) to the apex. Finally, the infundibular component separates the right from the left ventricular outflow tract.	**Image A** 3D TOE left side of IVS 'en face'. The colours red, yellow, and blue define the inlet, outlet, and trabecular components, respectively. **Image B** 3D TOE right side of IVS 'en face'. The colours red, yellow, and blue define the inlet, outlet, and trabecular components, respectively. The asterisk points at the MS.	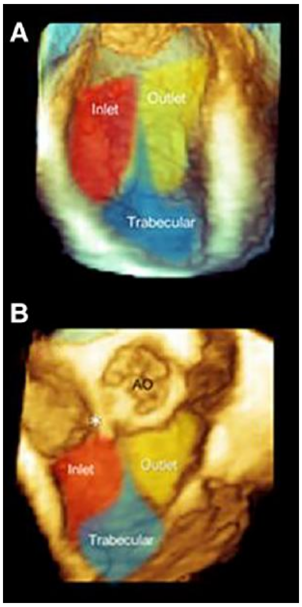
The membranous IVS[117] The membranous IVS is a thin, roughly quadrangular fibrous membrane of 10–15 mm. When viewed from a left ventricular perspective, the MS is positioned immediately below the interleaflet triangle (ILT) between the right and non-coronary sinuses. Thus, the superior margin of the MS is in continuity with the fibrous tissue of the ILT, while the inferior margin inserts on the crest of the muscular IVS. The hinge line of the septal tricuspid leaflet divides the MS into two parts: the atrioventricular MS, a partition between the RA and the LV, and the interventricular MS, a partition between ventricles. The latter is the location of perimembranous VSD.	**Image A** 3D TOE cross-section image in long-axis view. **Image B** Magnified image including the structures inside the red square of image A. The images show the MS below the interleaflet triangle (ILT). The white dotted line marks the boundaries of the ILT, while the red line marks the location of the His bundle.	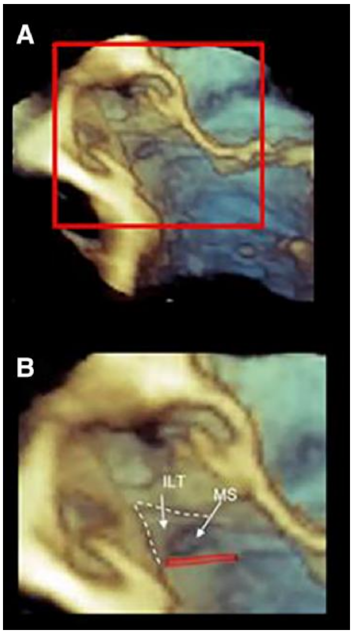

VSD

VSD can be divided into congenital and acquired VSD.

'Congenital VSDs' are the most common congenital defects apart the BAV. They can exist in isolation, but are also found as integral components of complex cardiac anomalies, such as tetralogy of Fallot, double outlet RV, or common arterial trunk.

Isolated congenital VSD vary greatly in location, clinical presentation, associated lesions, and clinical scenarios depending on the size of the defect. Currently, most congenital VSDs are discovered in the neonatal or paediatric population. 2D TTE and TEE, Doppler, and colour Doppler echocardiography provide, in experienced hands, all the morphological and haemodynamic data for a correct assessment of isolated VSD and for therapeutical options. In these patients, the 3D TOE has little relevance.[118]

'Acquired VSDs' can be secondary to trauma or to acute/subacute myocardial infarction (AMI). Large VSD post-AMI defects lead to the development of right ventricular dysfunction, pulmonary hypertension, congestive heart failure, low cardiac output, and a fatal cardiogenic shock.[119]

In both adult congenital VSDs or post-AMI VSD, 3D TOE is able to define the location, shape, and size of VSDs.

Table 35 shows some examples of congenital and acquired VSDs as illustrated by 3D TOE.

Table 35

Congenital VSD	Description of images	Images
Classically, there are two ways for classifying VSDs. One is based on their location within the septum from the right ventricular perspective. Another is based on the type of borders of VSDs and on their relationships with adjacent septum and/or surrounding fibrous structures. Both approaches are useful. The first allows to determine the site of surgical incision (i.e. through the atrium or through the RV or pulmonary artery), whereas the second classification helps to define the structures adjacent to the defect, such as the atrioventricular node and the His bundle or the atrioventricular leaflets. Knowledge of the structures adjacent to VSD may avoid injuries during the surgery or percutaneous closure.	3D TOE images showing the entire IVS from the right perspective. The black dots correspond to the location of congenital VSDs. **1, Perimembranous VSD** Located in the area of the interventricular part of the MS, below the septal leaflet of the TV at the level of anteroseptal commissure **2, Outlet VSD** Located in the muscular part of the infundibular septum, these VSDs are entirely surrounded by muscular tissue. The superior part of the defect is adjacent with the aortic and/or pulmonary annulus or both. These VSDs are termed supracristal, conal sub-pulmonary, or double-committed, respectively. **3, Trabecular VSD** These VSDs are located in the inlet, outlet, or trabecular parts of muscular septum, maintaining the muscular rim all around the defect.	
	Image A Muscular congenital VSD seen from the left ventricular perspective (black arrow). **Image B** Same case with colour Doppler. The image shows the flow crossing the defect (white arrow).	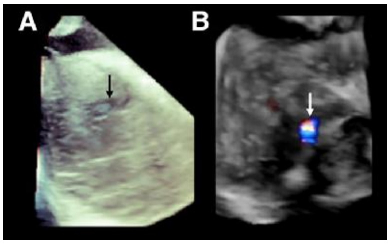
Acquired post-AMI VSD	**Description of images**	**Images**
Post-AMI VSD is a devastating complication occurring 1–8 days after transmural septal infarction, due to a complete occlusion of one major coronary vessel irrorating the IVS. Septal rupture in anterior AMI tends to be apical with a discrete simple hole. Conversely, in inferior–posterior AMI, the VSR is prevalently located in the basal portion of posterior septum and has often a more complex, serpiginous course.	**Image A** 3D TOE image full volume of LV, so cropped that the IVS is seen 'en face' view from the left perspective. A large VSD is present in the apical region (red circle) due to complete occlusion of the left anterior descendent artery. **Image B** Same case from the right perspective. (With the permission of Faletra et al. Interventional transoesophageal echocardiography Springer)	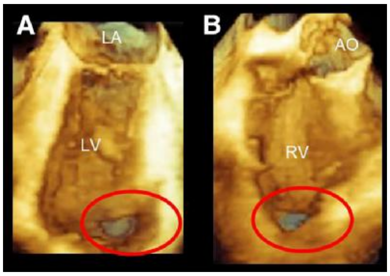

Conclusion

The intent of the present clinical consensus document is to provide a practical approach on the acquisition on 3D TOE images. While 2D will continue to be the main modality of the TOE examination, the authors believe that acquisition of 3D images should be an integral part of the TOE examination. The pathologies described in this document are those in which 3D TOE has shown to be a diagnostic tool particularly valuable.

Data availability

No new data were generated or analysed in support of this consensus document.

References

1. Hahn RT, Abraham T, Adams MS, Bruce CJ, Glas KE, Lang RM *et al.* Guidelines for performing a comprehensive transesophageal echocardiographic examination: recommendations from the American Society of Echocardiography and the Society of Cardiovascular Anesthesiologists. *J Am Soc Echocardiogr* 2013;**26**:921–64.
2. Savord B, Solomon R. Fully sampled matrix transducer for real time 3-D ultrasonic imaging. Hawaii, USA: Proc IEEE Ultrason Symp; 2003:945–53.
3. Lang RM, Mor-Avi V, Sugeng L, Nieman PS, Sahn DJ. Three-dimensional echocardiography: the benefits of the additional dimension. *J Am Coll Cardiol* 2006;**48**:2053–69.
4. Sugeng L, Shernan SK, Salgo IS, Weinert L, Shook D, Raman J *et al.* Live 3-dimensional transesophageal echocardiography initial experience using the fully-sampled matrix array probe. *J Am Coll Cardiol* 2008;**52**:446–9.
5. Kwak J, Andrawes M, Garvin S, D'Ambra MN. 3D Transesophageal echocardiography: a review of recent literature 2007–2009. *Curr Opin Anaesthesiol* 2010;**23**:80–8.

6. Tanabe K. Three-dimensional echocardiography- role in clinical practice and future directions. *Circ J* 2020;**84**:1047–54.
7. Lang RM, Badano LP, Tsang W, Adams DH, Agricola E, Buck T *et al.* EAE/ASE recommendations for image acquisition and display using three-dimensional echocardiography. *Eur Heart J Cardiovasc Imaging* 2012;**13**:1–46.
8. Faletra FF, Pedrazzini G, Pasotti E, Muzzarelli S, Dequarti MC, Murzilli R *et al.* 3D TEE during catheter-based interventions. *JACC Cardiovasc Imaging* 2014;**7**:292–308.
9. Rong LQ. An update on intraoperative three-dimensional transesophageal echocardiography. *J Thorac Dis* 2017;**9**:S271–82.
10. Yang HS, Bansal RC, Mookadam F, Khandheria BK, Tajik AJ. Chandrasekaran K; American Society of Echocardiography. Practical guide for three-dimensional transthoracic echocardiography using a fully sampled matrix array transducer. *J Am Soc Echocardiogr* 2008;**21**:979–89; quiz 1081–2.
11. Genovese D, Addetia K, Kebed K, Kruse E, Yamat M, Narang A *et al.* First clinical experience with 3-dimensional echocardiographic transillumination rendering. *JACC Cardiovasc Imaging* 2019;**12**:1868–71.
12. Karagodin I, Addetia K, Singh A, Dow A, Rivera L, DeCara JM *et al.* Improved delineation of cardiac pathology on echocardiographic images using a novel 3D tissue transparency tool. *J Am Soc Echocardiogr* 2020;**33**:1316–23.
13. Faletra FF, Ramamurthi A, Dequarti MC, Leo LA, Moccetti T, Pandian N. Artifacts in three-dimensional transesophageal echocardiography. *J Am Soc Echocardiogr* 2014;**27**: 453–62.
14. Faletra FF, Leo LA, Paiocchi VL, Caretta A, Viani GM, Schlossbauer SA *et al.* Anatomy of mitral annulus insights from non-invasive imaging techniques. *Eur Heart J Cardiovasc Imaging* 2019;**20**:843–57.
15. Quill JL, Hill AJ, Laske TG, Alfieri O, Iaizzo PA. Mitral leaflet anatomy revisited. *J Thorac Cardiovasc Surg* 2009;**137**:1077–81.
16. Chen S, Sari CR, Gao H, Lei Y, Segers P, De Beule M *et al.* Mechanical and morphometric study of mitral valve chordae tendineae and related papillary muscle. *J Mech Behav Biomed Mater* 2020;**111**:104011.
17. Axel L. Papillary muscles do not attach directly to the solid heart wall. *Circulation* 2004; **109**:3145–8.
18. Biaggi P, Gruner C, Jedrzkiewicz S, Karski J, Meineri M, Vegas A *et al.* Assessment of mitral valve prolapse by 3D TEE angled views are key. *JACC Cardiovasc Imaging* 2011; **4**:94–7.
19. Iung B, Vahanian A. Epidemiology of valvular heart disease in the adult. *Nat Rev Cardiol* 2011;**8**:162–72.
20. Carpentier A. Cardiac valve surgery--the "French correction". *J Thorac Cardiovasc Surg* 1983;**86**:323–37.
21. Adams DH, Rosenhek R, Falk V. Degenerative mitral valve regurgitation: best practice revolution. *Eur Heart J* 2010;**31**:1958–66.
22. Groeneveld SA, Kirkels FP, Cramer MJ, Evertz R, Haugaa KH, Postema PG *et al.* Prevalence of mitral annulus disjunction and mitral valve prolapse in patients with idiopathic ventricular fibrillation. *J Am Heart Assoc* 2022;**11**:e025364.
23. Faletra FF, Leo LA, Paiocchi VL, Schlossbauer SA, Pavon AG, Ho SY *et al.* Morphology of mitral annular disjunction in mitral valve prolapse. *J Am Soc Echocardiogr* 2022;**35**: 176–86.
24. Toh H, Mori S, Izawa Y, Fujita H, Miwa K, Suzuki M *et al.* Prevalence and extent of mitral annular disjunction in structurally normal hearts: comprehensive 3D analysis using cardiac computed tomography. *Eur Heart J Cardiovasc Imaging* 2021;**22**:614–22.
25. Lee AP, Jin CN, Fan Y, Wong RHL, Underwood MJ, Wan S. Functional implication of mitral annular disjunction in mitral valve prolapse: a quantitative dynamic 3D echocardiographic study. *JACC Cardiovasc Imaging* 2017;**10**:1424–33.
26. Agricola E, Oppizzi M, Maisano F, De Bonis M, Schinkel AF, Torracca L *et al.* Echocardiographic classification of chronic ischemic mitral regurgitation caused by restricted motion according to tethering pattern. *Eur J Echocardiogr* 2004;**5**:326–34.
27. Deferm S, Bertrand PB, Verbrugge FH, Verhaert D, Rega F, Thomas JD *et al.* Atrial functional mitral regurgitation: JACC review topic of the week. *J Am Coll Cardiol* 2019;**73**:2465–76.
28. Agricola E, Oppizzi M, Pisani M, Maisano F, Margonato A. Accuracy of real-time 3D echocardiography in the evaluation of functional anatomy of mitral regurgitation. *Int J Cardiol* 2008;**127**:342–9.
29. He S, Fontaine AA, Schwammenthal E, Yoganathan AP, Levine RA. Integrated mechanism for functional mitral regurgitation: leaflet restriction versus coapting force: in vitro studies. *Circulation* 1997;**96**:1826–34.
30. Zoghbi WA, Adams D, Bonow RO, Enriquez-Sarano M, Foster E, Grayburn PA *et al.* Recommendations for noninvasive evaluation of native valvular regurgitation: a report from the American Society of Echocardiography developed in collaboration with the Society for Cardiovascular Magnetic Resonance. *J Am Soc Echocardiogr* 2017;**30**: 303–71.
31. Little SH, Pirat B, Kumar R, Igo SR, McCulloch M, Hartley CJ *et al.* Three-dimensional color Doppler echocardiography for direct measurement of vena contracta area in mitral regurgitation: in vitro validation and clinical experience. *JACC Cardiovasc Imaging* 2008;**1**:695–704.
32. Yosefy C, Hung J, Chua S, Vaturi M, Ton-Nu TT, Handschumacher MD *et al.* Direct measurement of vena contracta area by real-time 3-dimensional echocardiography for assessing severity of mitral regurgitation. *Am J Cardiol* 2009;**104**:978–83.
33. Marsan NA, Westenberg JJ, Ypenburg C, Delgado V, van Bommel RJ, Roes SD *et al.* Quantification of functional mitral regurgitation by real-time 3D echocardiography: comparison with 3D velocity-encoded cardiac magnetic resonance. *JACC Cardiovasc Imaging* 2009;**2**:1245–52.
34. Zeng X, Levine RA, Hua L, Morris EL, Kang Y, Flaherty M *et al.* Diagnostic value of vena contracta area in the quantification of mitral regurgitation severity by color Doppler 3D echocardiography. *Circ Cardiovasc Imaging* 2011;**4**:506–13.
35. Carapetis JR, Beaton A, Cunningham MW, Guilherme L, Karthikeyan G, Mayosi BM *et al.* Acute rheumatic fever and rheumatic heart disease. *Nat Rev Dis Primers* 2016; **2**:15084.
36. Abramowitz Y, Jilaihawi H, Chakravarty T, Mack MJ, Makkar RR. Mitral annulus calcification. *J Am Coll Cardiol* 2015;**66**:1934–41.
37. Zamorano J, de Agustín JA. Three-dimensional echocardiography for assessment of mitral valve stenosis. *Curr Opin Cardiol* 2009;**24**:415–9.
38. Monteagudo Ruiz JM, Zamorano Gómez JL. The role of 2D and 3D echo in mitral stenosis. *J Cardiovasc Dev Dis* 2021;**8**:171.
39. Sadeghian H, Rezvanfard M, Jalali A. Measurement of mitral valve area in patients with mitral stenosis by 3D echocardiography: a comparison between direct planimetry on 3D zoom and 3D quantification. *Echocardiography* 2019;**36**:1509–14.
40. Zhong X, Chen W, Shi Z, Huan Z, Ma L, Liu W *et al.* Three-dimensional transesophageal echocardiography measurement of mitral valve area in patients with rheumatic mitral stenosis: multiplanar reconstruction or 3D direct planimetry? *Int J Cardiovasc Imaging* 2021;**37**:99–107.
41. Toufan Tabrizi M, Faraji Azad H, Khezerlouy-Aghdam N, Sakha H. Measurement of mitral valve area by direct three-dimensional planimetry compared to multiplanar reconstruction in patients with rheumatic mitral stenosis. *Int J Cardiovasc Imaging* 2022;**38**: 1341–9.
42. Loukas M, Bilinsky E, Bilinsky S, Blaak C, Tubbs RS, Anderson RH. The anatomy of the aortic root. *Clin Anat* 2014;**27**:748–56.
43. Paiocchi VL, Faletra FF, Ferrari E, Schlossbauer SA, Leo LA, Maisano F. Multimodality imaging of the anatomy of the aortic root. *J Cardiovasc Dev Dis* 2021;**8**:51.
44. Cheruvu C, Blanke P, Leipsic J. Imaging the aortic annulus with multi-detector computed tomography and 3-dimensional transesophageal echocardiography. *Interv Cardiol Clin* 2015;**4**:23–37.
45. Sutton JP 3rd, Ho SY, Anderson RH. The forgotten interleaflet triangles: a review of the surgical anatomy of the aortic valve. *Ann Thorac Surg* 1995;**59**:419–27.
46. Katayama S, Umetani N, Sugiura S, Hisada T. The sinus of Valsalva relieves abnormal stress on aortic valve leaflets by facilitating smooth closure. *J Thorac Cardiovasc Surg* 2008;**136**:1528–35, 1535.e1.
47. Calleja A, Thavendiranathan P, Ionasec RI, Houle H, Liu S, Voigt I *et al.* Automated quantitative 3-dimensional modeling of the aortic valve and root by 3-dimensional transesophageal echocardiography in normals, aortic regurgitation, and aortic stenosis: comparison to computed tomography in normals and clinical implications. *Circ Cardiovasc Imaging* 2013;**6**:99–108.
48. Shirazi S, Golmohammadi F, Tavoosi A, Salehi M, Larti F, Sardari A *et al.* Quantification of aortic valve area: comparison of different methods of echocardiography with 3-D scan of the excised valve. *Int J Cardiovasc Imaging* 2021;**37**:529–38.
49. Prihadi EA, van Rosendael PJ, Vollema EM, Bax JJ, Delgado V, Ajmone Marsan N. Feasibility, accuracy, and reproducibility of aortic annular and root sizing for transcatheter aortic valve replacement using novel automated three-dimensional echocardiographic software: comparison with multi-detector row computed tomography. *J Am Soc Echocardiogr* 2018;**31**:505–514.e3.
50. Stella S, Italia L, Geremia G, Rosa I, Ancona F, Marini C *et al.* Accuracy and reproducibility of aortic annular measurements obtained from echocardiographic 3D manual and semi-automated software analyses in patients referred for transcatheter aortic valve implantation: implication for prosthesis size selection. *Eur Heart J Cardiovasc Imaging* 2019;**20**:45–55.
51. Iung B, Delgado V, Rosenhek R, Price S, Prendergast B, Wendler O *et al.* Contemporary presentation and management of valvular heart disease: the EURObservational Research Programme Valvular Heart Disease II Survey. *Circulation* 2019;**140**:1156–69.
52. le Polain de Waroux JB, Pouleur AC, Goffinet C, Vancraeynest D, Van Dyck M, Robert A *et al.* Functional anatomy of aortic regurgitation: accuracy, prediction of surgical repairability, and outcome implications of transesophageal echocardiography. *Circulation* 2007;**116**:I264–9.
53. Michelena HI, Della Corte A, Evangelista A, Maleszewski JJ, Edwards WD, Roman MJ *et al.* International consensus statement on nomenclature and classification of the congenital bicuspid aortic valve and its aortopathy, for clinical, surgical, interventional and research purposes. *Eur J Cardiothorac Surg* 2021;**60**:448–76.
54. Muraru D, Hahn RT, Soliman OI, Faletra FF, Basso C, Badano LP. 3-dimensional echocardiography in imaging the tricuspid valve. *JACC Cardiovasc Imaging* 2019;**12**:500–15.

55. Schlossbauer SA, Faletra FF, Paiocchi VL, Leo LA, Franciosi G, Bonanni M *et al.* Multimodality imaging of the anatomy of tricuspid valve. *J Cardiovasc Dev Dis* 2021;**8**: 107.
56. Faletra FF, Leo LA, Paiocchi VL, Schlossbauer SA, Borruso MG, Pedrazzini G *et al.* Imaging-based tricuspid valve anatomy by computed tomography, magnetic resonance imaging, two and three-dimensional echocardiography: correlation with anatomic specimen. *Eur Heart J Cardiovasc Imaging* 2019;**20**:1–13.
57. Abdellaziz Dahou DL, Reisman M, Hahn RT. Anatomy and physiology of the tricuspid valve. *J Am Coll Cardiol Img* 2019;**12**:458–68.
58. Hahn RT, Weckbach LT, Noack T, Hamid N, Kitamura M, Bae R *et al.* Proposal for a standard echocardiographic tricuspid valve nomenclature. *JACC Cardiovasc Imaging* 2021;**14**:1299–305.
59. Waller BF, Howard J, Fess S. Pathology of tricuspid valve stenosis and pure tricuspid regurgitation--part I. *Clin Cardiol* 1995;**18**:97–102.
60. Prihadi EA, Delgado V, Leon MB, Enriquez-Sarano M, Topilsky Y, Bax JJ. Morphologic types of tricuspid regurgitation: characteristics and prognostic implications. *JACC Cardiovasc Imaging* 2019;**12**:491–9.
61. Hahn RT, Badano LP, Bartko PE, Muraru D, Maisano F, Zamorano JL *et al.* Tricuspid regurgitation: recent advances in understanding pathophysiology, severity grading and outcome. *Eur Heart J Cardiovasc Imaging* 2022;**23**:913–29.
62. Otto CM, Nishimura RA, Bonow RO, Carabello BA, Erwin JP 3rd, Gentile F *et al.* 2020 ACC/AHA guideline for the management of patients with valvular heart disease: executive summary: a report of the American College of Cardiology/American Heart Association Joint Committee on Clinical Practice Guidelines. *J Am Coll Cardiol* 2021; **77**:450–500.
63. Praz F, Muraru D, Kreidel F, Lurz P, Hahn RT, Delgado V *et al.* Transcatheter treatment for tricuspid valve disease. *EuroIntervention* 2021;**17**:791–808.
64. Muraru D, Caravita S, Guta AC, Mihalcea D, Branzi G, Parati G *et al.* Functional tricuspid regurgitation and atrial fibrillation: which comes first, the chicken or the egg? *CASE* 2020;**4**:458–63.
65. Ortiz-Leon XA, Posada-Martinez EL, Trejo-Paredes MC, Ivey-Miranda JB, Pereira J, Crandall I *et al.* Understanding tricuspid valve remodelling in atrial fibrillation using three-dimensional echocardiography. *Eur Heart J Cardiovasc Imaging* 2020;**21**:747–55.
66. Utsunomiya H, Harada Y, Susawa H, Ueda Y, Izumi K, Itakura K *et al.* Tricuspid valve geometry and right heart remodelling: insights into the mechanism of atrial functional tricuspid regurgitation. *Eur Heart J Cardiovasc Imaging* 2020;**21**:1068–78.
67. Vieitez JM, Monteagudo JM, Mahia P, Perez L, Lopez T, Marco I *et al.* New insights of tricuspid regurgitation: a large-scale prospective cohort study. *Eur Heart J Cardiovasc Imaging* 2020;**22**:196–202.
68. Hahn RT. State-of-the-art review of echocardiographic imaging in the evaluation and treatment of functional tricuspid regurgitation. *Circ Cardiovasc Imaging* 2016;**9**: e005332.
69. Hahn RT, Thomas JD, Khalique OK, Cavalcante JL, Praz F, Zoghbi WA. Imaging assessment of tricuspid regurgitation severity. *JACC Cardiovasc Imaging* 2019;**12**:469–90.
70. Utsunomiya H, Harada Y, Susawa H, Takahari K, Ueda Y, Izumi K *et al.* Comprehensive evaluation of tricuspid regurgitation location and severity using vena contracta analysis: a color Doppler three-dimensional transesophageal echocardiographic study. *J Am Soc Echocardiogr* 2019;**32**:1526–1537.e2.
71. Liu Y, Chen B, Zhang Y, Zuo W, Li Q, Jin L *et al.* Sources of variability in vena contracta area measurement for tricuspid regurgitation severity grading: comparison of technical settings and vendors. *J Am Soc Echocardiogr* 2021;**34**:270–278.e1.
72. de Agustin JA, Viliani D, Vieira C, Islas F, Marcos-Alberca P, Gomez de Diego JJ *et al.* Proximal isovelocity surface area by single-beat three-dimensional color Doppler echocardiography applied for tricuspid regurgitation quantification. *J Am Soc Echocardiogr* 2013;**26**:1063–72.
73. Lancellotti P, Pibarot P, Chambers J, Edvardsen T, Delgado V, Dulgheru R *et al.* Recommendations for the imaging assessment of prosthetic heart valves: a report from the European Association of Cardiovascular Imaging endorsed by the Chinese Society of Echocardiography, the Inter-American Society of Echocardiography, and the Brazilian Department of Cardiovascular Imaging. *Eur Heart J Cardiovasc Imaging* 2016;**17**:589–90.
74. Zoghbi WA, Chambers JB, Dumesnil JG, Foster E, Gottdiener JS, Grayburn PA *et al.* Recommendations for evaluation of prosthetic valves with echocardiography and Doppler ultrasound. *J Am Soc Echocardiogr* 2009;**22**:975–1014.
75. Sugeng L, Shernan SK, Weinert L, Shook D, Raman J, Jeevanandam V *et al.* Real-time three-dimensional transesophageal echocardiography in valve disease: comparison with surgical findings and evaluation of prosthetic valves. *J Am Soc Echocardiogr* 2008; **21**:1347–54.
76. Hixson CS, Smith MD, Mattson MD, Morris EJ, Lenhoff SJ, Salley RK. Comparison of transesophageal color flow Doppler imaging of normal mitral regurgitant jets in St. Jude Medical and Medtronic Hall cardiac prostheses. *J Am Soc Echocardiogr* 1992; **5**:57–62.
77. Rizzoli G, Guglielmi C, Toscano G, Pistorio V, Vendramin I, Bottio T *et al.* Reoperations for acute prosthetic thrombosis and pannus: an assessment of rates, relationship and risk. *Eur J Cardiothorac Surg* 1999;**16**:74–80.
78. Tanis W, Habets J, van den Brink RB, Symersky P, Budde RP, Chamuleau SA. Differentiation of thrombus from pannus as the cause of acquired mechanical prosthetic heart valve obstruction by non-invasive imaging: a review of the literature. *Eur Heart J Cardiovasc Imaging* 2014;**15**:119–29.
79. Pellikka PA. Prosthetic valve thrombus versus pannus: progress with imaging. *Circ Cardiovasc Imaging* 2015;**8**:e004283.
80. Mahmoud-Elsayed H. Added value of three-dimensional transesophageal echocardiography in management of mitral paravalvular leaks. *Echocardiography* 2020;**37**:954–64.
81. Marin-Cuartas M, Noack T. Mitral and tricuspid annuloplasty ring dehiscence, a story yet to be told. *Eur J Cardiothorac Surg* 2021;**60**:811–2.
82. Daniel WG, Mügge A, Martin RP, Lindert O, Hausmann D, Nonnast-Daniel B *et al.* Improvement in the diagnosis of abscesses associated with endocarditis by transesophageal echocardiography. *N Engl J Med* 1991;**324**:795–800.
83. Erbel R, Rohmann S, Drexler M, Mohr-Kahaly S, Gerharz CD, Iversen S *et al.* Improved diagnostic value of echocardiography in patients with infective endocarditis by transesophageal approach. A prospective study. *Eur Heart J* 1988;**9**:43–53.
84. Berdejo J, Shibayama K, Harada K, Tanaka J, Mihara H, Gurudevan SV *et al.* Evaluation of vegetation size and its relationship with embolism in infective endocarditis: a real-time 3-dimensional transesophageal echocardiography study. *Circ Cardiovasc Imaging* 2014;**7**:149–54.
85. Tolstrup K, Shiota T, Gurudevan S, Luthringer D, Luo H, Siegel RJ. Left atrial myxomas: correlation of two-dimensional and live three-dimensional transesophageal echocardiography with the clinical and pathologic findings. *J Am Soc Echocardiogr* 2011;**24**: 618–24.
86. Müller S, Feuchtner G, Bonatti J, Müller L, Laufer G, Hiemetzberger R *et al.* Value of transesophageal 3D echocardiography as an adjunct to conventional 2D imaging in preoperative evaluation of cardiac masses. *Echocardiography* 2008;**25**:624–31.
87. Lestuzzi C. Primary tumors of the heart. *Curr Opin Cardiol* 2016;**31**:593–8.
88. Parato VM, Nocco S, Alunni G, Becherini F, Conti S, Cucchini U *et al.* Imaging of cardiac masses: an updated overview. *J Cardiovasc Echogr* 2022;**32**:65–75.
89. Sun JP, Asher CR, Yang XS, Cheng GG, Scalia GM, Massed AG *et al.* Clinical and echocardiographic characteristics of papillary fibroelastomas: a retrospective and prospective study in 162 patients. *Circulation* 2001;**103**:2687–93.
90. Pfister R, Betton Y, Freyhaus HT, Jung N, Baldus S, Michels G. Three-dimensional compared to two-dimensional transesophageal echocardiography for diagnosis of infective endocarditis. *Infection* 2016;**44**:725–31.
91. Hansalia S, Biswas M, Dutta R, Hage FG, Hsuing MC, Nanda NC *et al.* The value of live real time three-dimensional transesophageal echocardiography in the assessment of valvular vegetations. *Echocardiography* 2009;**26**:1264–73.
92. Spiliopoulos K, Haschemi A, Fink G, Kemkes BM. Infective endocarditis complicated by paravalvular abscess: a surgical challenge. An 11–year single center experience. *Heart Surg Forum* 2010;**13**:E67–73.
93. Gürsoy MO, Özkan M, Aykan AÇ, Yıldız M, Kahveci G. Multimodality imaging of the mitral paravalvular abscess cavity with left ventriculo-atrial fistula. *Heart Lung Circ* 2012;**21**:284–6.
94. Cui X, Li Y, Liu J, He S, Liu M. Aortic arch atheroma and the risk of stroke: a meta-analysis. *J Evid Based Med* 2014;**7**:185–91.
95. Klimek-Piotrowska W, Hołda MK, Koziej M, Piątek K, Hołda J. Anatomy of the true interatrial septum for transseptal access to the left atrium. *Ann Anat* 2016;**205**:60–4.
96. Faletra FF, Leo LA, Paiocchi VL, Schlossbauer SA, Pedrazzini G, Moccetti T *et al.* Revisiting anatomy of the interatrial septum and its adjoining atrioventricular junction using noninvasive imaging techniques. *J Am Soc Echocardiogr* 2019;**32**:580–92.
97. Faletra FF, Nucifora G, Ho SY. Imaging the atrial septum using real-time three-dimensional transesophageal echocardiography: technical tips, normal anatomy, and its role in transseptal puncture. *J Am Soc Echocardiogr* 2011;**24**:593–9.
98. Zisa D, Faletra FF, Wessler BS, Halin NJ, Reddy P, Patel AR *et al.* Ridges and pouches: a case series of anomalous atrial septal fusion. *CASE (Phila)* 2019;**4**:7–17.
99. de Almeida Gripp E, de Freitas Portela AC, Rabischoffsky R, Rabischoffsky D, de Oliveira Vaz LR, de Carvalho Silva L *et al.* Atrium septal pouch: an anatomic variant of the interatrial septum. *CASE (Phila)* 2020;**4**:328–30.
100. Kapoor R, Wadi L, Becerra B, Eskander M, Razmara A, Lombardo D *et al.* The left atrial septal pouch: A new stroke risk factor? *Transl Stroke Res* 2021;**12**:205–11.
101. Giannopoulos A, Gavras C, Sarioglou S, Agathagelou F, Kassapoglou I, Athanassiadou F. Atrial septal aneurysms in childhood: prevalence, classification, and concurrent abnormalities. *Cardiol Young* 2014;**24**:453–8.
102. Topaz O, Edwards JE, Bojack-Mackey S, Titus JL. Aneurysm of fossa ovalis in adults: a pathologic study. *Cardiovasc Pathol* 2003;**12**:219–25.
103. Arslan A, Yılmaz DÇ, Adıyaman M, Kara C, Örsçelik Ö, Yılmaz IA. Study of transesophageal echocardiography in young patients with cryptogenic stroke: prevalence of patent foramen ovale and interpretation of the RoPE score. *Turk Kardiyol Dern Ars* 2022; **50**:314–9.
104. Fazio G, Ferro G, Barbaro G, Ferrara F, Novo G, Novo S. Patent foramen ovale and thromboembolic complications. *Curr Pharm Des* 2010;**16**:3497–502.

105. Saric M, Perk G, Purgess J, Kronzon I. Imaging atrial septal defects by real-time 3D transesophageal echocardiography: step-by-step approach. *J Am Soc Echocardiogr* 2010;**23**:1128–35.
106. Hindricks G, Potpara T, Dagres N, Arbelo E, Bax JJ, Blomström-Lundqvist C *et al.* 2020 ESC guidelines for the diagnosis and management of atrial fibrillation developed in collaboration with the European Association for Cardio-Thoracic Surgery (EACTS): the task force for the diagnosis and management of atrial fibrillation of the European Society of Cardiology (ESC) developed with the special contribution of the European Heart Rhythm Association (EHRA) of the ESC. *Eur Heart J* 2021;**42**: 373–498.
107. Faletra FF, Ho SY, Auricchio A. Anatomy of right atrial structures by real-time 3D transesophageal echocardiography. *JACC Cardiovascular imaging* 2010;**3**:966–75.
108. Kalman JM, Olgin JE, Karch MR, Hamdan M, Lee RJ, Lesh MD. “Cristal tachycardias”: origin of right atrial tachycardias from the crista terminalis identified by intracardiac echocardiography. *J Am Coll Cardiol* 1998;**31**:451–9.
109. Regoli F, Faletra F, Marcon S, Leo LA, Dequarti MC, Caputo ML *et al.* Anatomic characterization of cavotricuspid isthmus by 3D transesophageal echocardiography in patients undergoing radiofrequency ablation of typical atrial flutter. *Eur Heart J Cardiovasc Imaging* 2018;**19**:84–91.
110. Saremi F, Pourzand L, Krishnan S, Ashikyan O, Gurudevan SV, Narula J *et al.* Right atrial cavotricuspid isthmus: anatomic characterization with multi-detector row CT. *Radiology* 2008;**247**:658–68.
111. Fichadiya H, Shah KK, Noori MAM, Khandait H, Rath P, Latif A *et al.* A rare case of eustachian valve endocarditis in a young male with poorly controlled type 1 diabetes mellitus. *Cureus* 2022;**14**:e25314.
112. Ho SY, McCarthy KP, Faletra FF. Anatomy of the left atrium for interventional echocardiography. *Eur J Echocardiogr* 2011;**12**:i11–5.
113. Faletra FF, Nucifora G, Regoli F, Ho SY, Moccetti T, Auricchio A. Anatomy of pulmonary veins by real-time 3D TEE: implications for catheter-based pulmonary vein ablation. *JACC Cardiovasc Imaging* 2012;**5**:456–62.
114. Cabrera JA, Ho SY, Climent V, Sánchez-Quintana D. The architecture of the left lateral atrial wall: a particular anatomic region with implications for ablation of atrial fibrillation. *Eur Heart J* 2008;**29**:356–62.
115. Di Biase L, Santangeli P, Anselmino M, Mohanty P, Salvetti I, Gili S *et al.* Does the left atrial appendage morphology correlate with the risk of stroke in patients with atrial fibrillation? Results from a multicenter study. *J Am Coll Cardiol* 2012;**60**:531–8.
116. Armour JA, Lippincott DB, Randall WC. Functional anatomy of the interventricular septum. *Cardiology* 1973;**58**:65–79.
117. Teofilovski-Parapid G, Baptista CA, DiDio LJ, Vaughan C. The membranous portion of the interventricular septum and its relationship with the aortic valve in humans. *Surg Radiol Anat* 1991;**13**:23–8.
118. Minette MS, Sahn DJ. Ventricular septal defects. *Circulation* 2006;**114**:2190–7. Erratum in: Circulation. 2007 Feb 20;115(7):e205.
119. Trivedi KR, Aldebert P, Riberi A, Mancini J, Levy G, Macia JC *et al.* Sequential management of post-myocardial infarction ventricular septal defects. *Arch Cardiovasc Dis* 2015; **108**:321–30.